Characterization of Surface Plasmons and Toroidal Moments Using Relativistic Electrons

Surong Guo

TECHNISCHE
UNIVERSITÄT
DARMSTADT

This page intentionally left blank

Characterization of Surface Plasmons and Toroidal Moments Using Relativistic Electrons

Dissertation submitted to the Department of Materials and Earth Sciences at Technische Universität Darmstadt

in Fulfillment of the Requirements for the Degree of
Doctor of Natural Science (Dr. rer. nat.)

by
Surong Guo
at Max Planck Institute for Solid State Research

M.Sc. Advanced Materials 2013
B.Eng. Metallic Material Engineering 2010
Born in China

TECHNISCHE
UNIVERSITÄT
DARMSTADT

Technische Universität Darmstadt, Hochschulkennziffer D17

Date of Submission: 28th June, 2018
Date of Oral Examination: 9th August, 2018

Referee: Prof. Dr. Peter A. van Aken
Co-referee: Prof. Dr. Hans-Joachim Kleebe

Darmstadt 2018

THESIS SUPERVISORS

Prof. Dr. Peter A. van Aken

Professor of Geo-Material Science
Stuttgart Center for Electron Microscopy (StEM)
Max Planck Institute for Solid State Research

Prof. Dr. Hans-Joachim Kleebe

Professor of Geo-Material Science
Geo- and Material Sciences Department
Technical University of Darmstadt

THESIS COMMITTEE

Prof. Dr. Peter A. van Aken

Referee
Professor of Geo-Material Science
Geo- and Material Sciences Department
Technical University of Darmstadt

Prof. Dr. Hans-Joachim Kleebe

Co-referee
Professor of Geo-Material Science
Geo- and Material Sciences Department
Technical University of Darmstadt
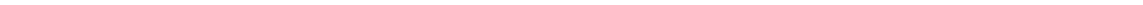
Prof. Dr. Ensinger Wolfgang

Examiner
Professor of Materials Science
Materials Science Department
Technical University of Darmstadt

Prof. Dr. Annette Andrieu-Brunsen

Examiner
Junior professor of Chemistry
Chemistry Department
Technical University of Darmstadt

This page intentionally left blank

Characterization of Surface Plasmons

and Toroidal Moments Using Relativistic Electrons

By

Surong Guo

Submitted to the Department of Materials and Earth Sciences on June 28th, 2018
in Partial Fulfillment of the Requirements for the Degree of
Doctor of Natural Science in Materials Science

ABSTRACT

Plasmonics is one of the research fields in nano-optics with the emphasis on resonant light–matter interactions. Plasmonics has attracted tremendous attention by exhibiting the capability of focusing electromagnetic fields and confining the field beyond the diffraction limit, for enhancing light–matter interactions on the nanoscale. Therefore, plasmons have been applied in the fields of near-field imaging, biosensing, light harvesting, light nanofocusing and emitting, medicine thermotherapy, *etc*.

One of the fundamental investigations is to characterize plasmonic phenomena of a single nano-object in order to systematically quantify the influence of variables in a controlled way. It requires not only the good control of nanofabrication but also an effective and comprehensive characterization tool with a spatial resolution on the nanoscale. Here, electron energy-loss spectroscopy, energy-filtered transmission electron microscopy, and cathodoluminescence spectroscopy are applied as they are the pioneering methods to ´observe´ plasmonic phenomena on the nanoscale, owing to the great instrumentation improvement in the electron energy monochromator and the stability of transmission electron microscopes.

Three-dimensional gold tapers play an important role in nano-optics. They possess the capability of light nanofocusing by transforming surface plasmon polaritons on the shaft to localized surface plasmons at the apex. In this thesis, I employed electron energy-loss spectroscopy and energy-filtered transmission electron microscopy to resolve discrete plasmonic modes in this transformation region beyond the range of optical microscopy. The link and distinction of the underlying physics of the observed modes were disentangled by systematically investigating the plasmonic modes of gold tapers with different opening angles, in combination with numerical finite-difference time-domain simulations. These results suggested that there were two main coexisting mechanisms, namely reflection and phase matching, mutually contributing to the observed plasmonic modes. The dominance from reflection to phase matching was modulated when increasing the interaction length between the fast electrons and the taper near-field. Additionally, the radiation properties of the plasmonic modes in gold tapers are further investigated by using cathodoluminescence spectroscopy. The results are helpful in designing gold tapers as nanofocusing waveguides and as point sources for photon emission.

Another employment of electron energy-loss spectroscopy in this thesis is to explore the fundamental electromagnetic properties of the third family of elementary electromagnetic sources, namely toroidal moments. Despite the infancy of the field, dynamic toroidal moments have recently triggered

increasing research interest initiated by their peculiar symmetry character, i.e., having odd parity under time- and space-inversion symmetry operations. Metamaterial engineering makes the dominant toroidal dipole responses detectable without being masked by electric or magnetic dipoles. A toroidal dipole response can be achieved in the optical regime via plasmon-induced displacement currents. One fundamental question is, whether single dynamic toroidal dipoles radiate to the far-field. Theoretical developments have renewed the understanding of the radiative properties of toroidal dipoles, however there is still lack of experimental evidence. I have experimentally investigated the far-field radiation of toroidal dipole moments in a plasmonic heptamer nanocavity by cathodoluminescence spectroscopy. On the other hand, the present focus of this field is on the novel optical phenomena of a single toroidal dipole resonance and its interactions with electric and magnetic multipoles. Differently, I am interested in the fundamental toroidal dipole–dipole coupling, as the coupling effect tailors the optical response and can be adopted as building and manipulating element for designing potential devices. The transverse coupling of toroidal dipoles was carried out on a plasmonic decamer nanocavity. Here, I experimentally characterized the pronounced coupled toroidal modes by electron energy-loss spectroscopy and visualized them by energy-filtered transmission electron microscopy. The coupling mechanism was further illustrated via theoretical analysis, and a simplified toroidal dipole–dipole interaction model was therefore proposed in a qualitative way. The finding paves the way for further research and exploitation in the fields of nano-optics and meta-devices.

KURZFASSUNG

Die Plasmonik ist eines der Forschungsgebiete der Nanooptik mit Schwerpunkt auf resonanten Licht–Materie-Wechselwirkungen. Die Plasmonik hat große Aufmerksamkeit auf sich gezogen, indem sie die Fokussierung elektromagnetischer Felder über die Beugungsgrenze hinaus ermöglicht und damit verstärkte Licht–Materie-Wechselwirkungen auf der Nanoskala ermöglicht. Daher wurden Plasmonen u.a. zur Abbildung mittels Nahfeld-Optik, der Biosensorik, zur Licht-Nanofokussierung und -emission, in der Medizinthermotherapie eingesetzt.

Eine der grundlegenden Untersuchungen besteht darin, plasmonische Phänomene eines einzelnen Nanoobjekts zu charakterisieren, um den Einfluss von Variablen auf kontrollierte Weise systematisch zu quantifizieren. Dies erfordert nicht nur eine gute Kontrolle der Nanofabrikation, sondern auch ein effektives und umfassendes Charakterisierungswerkzeug mit einer räumlichen Auflösung im Nanobereich. In dieser Arbeit werden Elektronenenergieverlust-Spektroskopie, energiegefilterte Transmissionselektronen-mikroskopie und Kathodolumineszenz verwendet, da mit diesen Methoden plasmonische Phänomene auf der Nanoskala untersucht werden können. Wesentlich sind hierbei der Einsatz neuer Elektronen-Monochromatoren sowie die verbesserte Stabilität moderner Transmissionselektronenmikroskope.

Dreidimensionale Goldspitzen spielen eine wichtige Rolle in der Nanooptik. Sie besitzen die Fähigkeit zur Nanofokussierung von Licht durch Umwandlung von auf der Oberfläche propagierenden Oberflächenplasmonpolaritonen zu lokalisierten Oberflächenplasmonen an der Spitze. In dieser Arbeit verwendete ich Elektronenenergieverlustspektroskopie und energiegefilterte Transmissionselektronen-mikroskopie, um diskrete plasmonische Moden nachzuweisen die der optischen Mikroskopie nicht zugänglich sind. Die Verknüpfung und Unterscheidung der zugrundeliegenden Physik der beobachteten Moden wurde entschlüsselt, indem die plasmonischen Moden von Goldspitzen mit unterschiedlichen Öffnungswinkeln in Kombination mit der numerischen Finite-Differenz-Methode im Zeitbereich systematisch untersucht wurden. Diese Ergebnisse legen nahe, dass zwei koexistierende Mechanismen zu unterscheiden sind, nämlich Reflexion und Phasenanpassung, die beide zu den beobachteten plasmonischen Moden beitragen. Phasenanpassung wird dann dominant wenn die Wechselwirkungslänge zwischen den schnellen Elektronen und dem konischen Nahfeld erhöht wird. Zusätzlich wurden die Strahlungseigenschaften der plasmonischen Moden in Goldspitzen mittels Kathodolumineszenzspektroskopie untersucht. Die Ergebnisse tragen dazu bei, Goldspitzen als nanofokussierende Wellenleiter und als Punktquellen für die Photonenemission zu entwerfen.

Eine weitere Anwendung der Elektronenenergieverlustspektroskopie in dieser Arbeit besteht darin, die elektromagnetischen Grundeigenschaften der dritten Familie elementarer elektromagnetischer Quellen zu untersuchen, nämlich der Toroidmomente. Obwohl dieses Forschungsgebiet noch jung ist, haben dynamische Toroidmomente in jüngster Zeit ein zunehmendes Forschungsinteresse ausgelöst, das durch ihren besonderen Symmetriecharakter ausgelöst wird, nämlich der ungeraden Parität unter Zeit- und Rauminversionssymmetrie-operationen. Die Herstellung von Metamaterialien macht Strukturen möglich bei denen toroidale Dipole dominant sind und damit detektierbar werden, ohne durch elektrische oder magnetische Dipole überdeckt zu werden. Ein toroidaler Dipol kann im optischen Bereich mittels plasmoninduzierter Verschiebungsströme erreicht werden. Eine grundlegende Frage ist, ob einzelne dynamische toroidale Dipole zum Fernfeld beitragen. Theoretische Entwicklungen haben das Verständnis der strahlenden Eigenschaften von toroidalen Dipolen vertieft, jedoch fehlen immer noch experimentellen Beweise. Ich habe die Fernfeldstrahlung toroidaler Dipolmomente in einer plasmonischen Heptamer-Nanokavität experimentell durch Kathodolumineszenz-spektroskopie untersucht. Die gegenwärtige Forschung konzentriert sich auf die neuartigen optischen Phänomene

singulärer toroidaler Dipolresonanzen und derer Wechselwirkung mit elektrischen und magnetischen Multipolen. Im Gegensatz dazu untersuche ich die fundamentale Dipol–Dipol-Kopplung zweier toroidaler Momente, da diese Kopplung das optische Verhalten bestimmt und dieses Wissen für den Bau- und Entwurf potentieller Bauelemente verwendet werden kann. Die transversale Kopplung von toroidalen Dipolen wurde auf einer plasmonischen Dekamer-Nanokavität durchgeführt. Hier habe ich die ausgeprägten gekoppelten Toroidmoden experimentell durch Elektronenenergieverlustspektroskopie charakterisiert und durch energiegefilterte Transmissionselektronenmikroskopie visualisiert. Der Kopplungsmechanismus wurde durch theoretische Analyse veranschaulicht, und es wird ein vereinfachtes qualitatives toroidales Dipol–Dipol-Wechselwirkungsmodell vorgeschlagen. Das Ergebnis ebnet den Weg für weitere Forschung und Nutzung in den Bereichen der Nano-Optik und von Geräten die auf Meta-Materialien basieren.

ACKNOWLEDGMENTS

BIOGRAPHICAL NOTE

EDUCATION

Ph.D.	Max Planck Institute for Solid State Research Technical University of Darmstadt (TUD)	2014–2018
	Materials Science	*Supervised by,* Prof. Dr. Peter A. van Aken Prof. Dr. Hans-Joachim Kleebe
M.Sc.	University of Ulm	2010–2013
	Advanced Materials –Nanomaterials	*Supervised by,* Prof. Dr. Ulrich Herr Prof. Dr. Peter Unger
B.Eng.	Shandong University	2006–2010
	Metallic Materials Engineering	*Supervised by,* Prof. Dr. Chuanzhong Chen

PUBLICATIONS

Peer-reviewed journal publications

A. <u>Surong Guo</u>, Nahid Talebi, Wilfried Sigle, Ralf Vogelgesang, Gunther Richter, Martin Esmann, Simon F. Becker, Christoph Lienau, Peter A. van Aken, "Reflection and phase matching in plasmonic gold tapers", *Nano Letters*, **16**, 6137–6144 (2016).

B. Nahid Talebi, <u>Surong Guo</u>, Peter A. van Aken, "Theory and applications of toroidal moments in electrodynamics: their emergence, characteristics, and technological relevance", *Nanophotonics*, **7**, 93–110 (2017).

C. <u>Surong Guo</u>, Nahid Talebi, Peter A. van Aken, "Long-range coupling of toroidal moments for the visible", *ACS Photonics*, **5**, 1326–1333 (2018).

D. Xu Wang, Varun Sridhar, <u>Surong Guo</u>, Nahid Talebi, Alber Miguel-López, Kersten Hahn, Peter A. van Aken, Samuel Sánchez, "Fuel-free nanocap-like motors actuated under visible light", *Advanced Functional Materials*, 1705862 (2018).

Conference contributions

a. Surong Guo, Nahid Talebi, Wilfried Sigle, Christoph Lienau, Alfredo Campos, Mathieu Kociak, Martin Esmann, Simon F Becker, Ralf Vogelgesang, Peter A van Aken, "Interaction between relativistic electrons and mesoscopic plasmonic tapers" (<u>invited lecture</u>), Microscopy and Microanalysis, August 2017, St. Louis, MO, USA.

b. Surong Guo, Nahid Talebi, Peter van Aken, "Unveiling long-range coupling of toroidal moments by EELS and EFTEM" (abstract), 19th International Microscopy Conference, September 2018, Sydney, Australia.

c. Surong Guo, Nahid Talebi, Wilfried Sigle, Christoph Lienau, Alfredo Campos, Mathieu Kociak, Martin Esmann, Simon F Becker, Ralf Vogelgesang, Peter A van Aken, "Reflection and phase matching in mesoscopic plasmonic tapers investigated by relativistic electrons" (abstract), Microscopy Conference, August 2017, Lausanne, Switzerland.

d. Surong Guo, Nahid Talebi, Wilfried Sigle, Ralf Vogelgesang, Martin Esmann, Simon F Becker, Christoph Lienau, Peter van Aken, "Transverse and longitudinal resonances in plasmonic gold tapers" (1st place poster prize), NanoMeta 2017, January 2017, Seefeld, Austria.

e. Surong Guo, Nahid Talebi, Wilfried Sigle, Peter A. van Aken, "Investigation of toroidal moments by relativistic electrons" (oral lecture), International Workshop at Ringberg Castle, January 2017, Germany.

f. Surong Guo, Nahid Talebi, Wilfried Sigle, Ralf Vogelgesang, Martin Esmann, Simon F Becker, Christoph Lienau, Peter van Aken, "Investigation of plasmonic modes of gold tapers by EELS" (poster), European Microscopy Congress, August 2016, Lyon, France.

g. Surong Guo, Nahid Talebi, Wilfried Sigle, Ralf Vogelgesang, Martin Esmann, Simon F Becker, Christoph Lienau, Peter van Aken, "Reflection and phase matching in plasmonic gold tapers" (oral lecture), International Workshop at Ringberg Castle, June 2016, Germany.

h. Surong Guo, Nahid Talebi, Wilfried Sigle, Ralf Vogelgesang, Martin Esmann, Simon F Becker, Christoph Lienau, Peter van Aken, "Higher-order plasmonic modes of gold tapers" (oral lecture), Deutsche Physikalische Gesellschaft Conference 2016, March 2016, Regensburg, Germany.

i. Surong Guo, Nahid Talebi, Wilfried Sigle, Martin Esmann, Simon F. Becker, Ralf Vogelgesang, Christoph T. Lienau, Peter A. van Aken, "Investigation of plasmonic modes of gold tapers by EFTEM and EELS" (best poster prize), Microscopy Conference 2015, September 2015, Goettingen, Germany.

j. Surong Guo, Nahid Talebi, Wilfried Sigle, Martin Esmann, Simon F Becker, Ralf Vogelgesang, Christoph T Lienau, Peter A van Aken, "Real-space imaging of plasmonic modes of gold tapers by EFTEM and EELS" (oral lecture), The European Conference on Lasers and Electro-Optics, June 2015, Munich, Germany.

Papers A, B and C are included and discussed in this dissertation.

Contents

List of figures

List of abbreviations

BF	Bright field
CL	Cathodoluminescence (spectroscopy)
DF	Dark field
EEL	Electron-energy-loss
EELS	Electron-energy-loss spectroscopy
EFTEM	Energy-filtered transmission electron microscopy
FIB	Focused ion beam
FWHM	Full width at half maximum
FDTD	Finite-difference time-domain
HAADF	High-angle annular dark field
LSPRs	Localized surface plasmon resonances
SEM	Scanning electron microscopy
SESAM	Sub-electron-volt sub-angstrom microscope
SPs	Surface plasmons
SPPs	Surface plasmon polaritons
SPRs	Surface plasmon resonances
STEM	Scanning transmission electron microscopy
TEM	Transmission electron microscopy
ZLP	Zero-loss peak

Chapter 1   Introduction

In Chapter 1, I will explain the motivation of employing electron-microscopy-related techniques in the field of plasmonics. Then I will introduce two objects, surface plasmons and toroidal moments, to which the characterization techniques were applied in this thesis. The interaction between fast electrons and surface plasmons (SP) will be the core of this chapter to be introduced, as it is the cornerstone for plasmon characterization and sequential data interpretation. Next, I will outline the characterization principles of energy-filtered transmission electron microscopy (EFTEM), low-loss electron energy-loss spectroscopy (EELS), and cathodoluminescence spectroscopy (CL). The fundamentals for numeric simulations will be briefly explained for its necessity in interpreting experimental results. The outline of this thesis will be sketched at the end.

1.1   Motivation

Far-field photon-based spectroscopies have been the dominating characterization techniques to explore the optical and electronic properties of materials. Due to the rapid development of optically active nanomaterials and nanostructured materials, the understanding of light–matter interaction on the nanometer scale has become the fundamental issue in optoelectronics and nanophotonics.[1] Moreover, phenomena on the nanoscale, such as surface plasmons and local inhomogeneities of the band gap or structure, can significantly affect the optical response of nano-objects. Effective characterization techniques at the equivalent scales are of significant necessity, especially for directly correlating local variations to the displayed optical properties.[2] However, the diffraction limit of light hinders conventional optical microscopy to directly observe the phenomena at nanometer resolution.[3, 4] Only an averaged response over many nano-objects can be measured with conventional absorption/scattering/reflection optical microscopy.[5] One approach to overcome this limitation is to use near-field optical microscopy, which is mainly based on collecting evanescent near-field signals for resolution improvement. Another approach is to replace the optical probe with an electron probe by taking the advantage of ultra-small de Broglie wavelengths. The latter holds the best spatial resolution even down to the atomic level under certain circumstances.[6]

Modern electron microscopes are capable of forming highly focused electron probes with sub-nanometer size and < 0.1 eV energy resolution, as benefited from a series of technical developments such as electron sources, lenses, and monochromators, but also from the improvement of mechanical and electrical stability.[7] This extremely small probe size provides the possibility for achieving high spatial resolution. Thus the related techniques, such as low-loss electron energy-loss spectroscopy (low-loss EELS) and cathodoluminescence spectroscopy (CL) in scanning transmission electron microscopy (STEM), have been employed to investigate the electromagnetic properties of individual plasmonic nano-objects. Furthermore, electron-based measurements provide related, but more comprehensive information compared to photon-based measurements.[4, 8]

Electron energy-loss spectroscopy has a history in discovering and characterizing collective excitations of conduction electrons in metals (plasmon) since the 1940s. In 1941 Ruthemann showed a *transmission* electron energy-loss spectrum of an Al thin film with a series of peaks at multiples of 16 eV;[9] this characteristic energy loss is now known as the bulk plasmon energy of Al.[10] In 1959 the first experimental evidence of surface plasmons was achieved on an Al thin film by *reflection* electron energy-loss spectroscopy;[11] it verified Ritchie´s proposal on surface plasmons (originally termed depolarization effect of surface charge) two years earlier.[12] However, the early works were only able

to identify plasmons in the frequency domain (i.e. resonant peaks in spectra), but not to ´see´ them in real space. It was not until 2007 that a breakthrough in mapping localized surface plasmons of single nanoparticles at nanometer resolution was reported by two independent groups with modern low-loss EELS techniques in a STEM.[1, 2] Another equivalent technique for visualizing localized surface plasmons on the nanoscale is energy-filtered transmission electron microscopy (EFTEM), where images are formed using electrons with a specific amount of energy losses corresponding to specific plasmon excitations.[13, 14]

CL constitutes another characterization technique and it is based on the phenomenon of light emission from a material by the impingement of an electron. It was applied conventionally in geological sciences and for semiconductors. Nowadays after being incorporated into modern electron microscopes, this technique receives great attention in characterizing nanoscale optical phenomena.[15-19] As CL only characterizes the radiative part of plasmonic excitations, it is thus considered as to be complementary to EELS measurements, in which both radiative and non-radiative excitations are detected.[20]

On the other hand, numerical finite-difference time-domain (FDTD) simulations are significantly helpful to understand the underlying physics of experimental observations. In this thesis, I will dedicate these advanced experimental techniques in combination with the numerical finite-difference time-domain (FDTD) simulations, which were performed by Dr. Nahid Talebi, to investigate surface-plasmon phenomena: (i) plasmonic properties of tapered gold tips for their extraordinary capability in nanofocusing and field localization; (ii) radiative properties and the coupling effect of the unique dynamic toroidal moments in plasmonic nanocavities.

1.2 Plasmons

Plasmons refer to the coherent collective oscillation of conduction electrons in metals. A plasmon represents a discrete quantity (quantum) of the collective oscillation energy, conceptually analogous to the phonon for atom vibrations or photons for electromagnetic waves. To explain the ´plasmon´ intuitively, a neutral metal is considered, which is represented by a background of fixed positive charges and an ocean of negatively charged electrons (Figure 1–1). When a group of electrons is displaced under excitation, an area with excess positive charge is left behind and then creates a local electric dipole moment. The induced electric field tends to restore the group of electrons to a uniform density. The process results in a plasma oscillation at a characteristic frequency.[21]

In contrast to plasmons in bulk (so-called bulk or volume plasmons), interface plasmons are referred to plasmons existing at the interface between two materials. If one of the materials is the vacuum, the plasmon is called surface plasmon. SPs are classified as **localized** surface plasmon resonances (LSPRs) and **propagating** surface plasmon polaritons (SPPs). LSPRs are confined to a limited space, whereas the propagating SPPs travel along the sustained surfaces. The size and shape of plasmonic structures determine whether LSPRs or SPPs can be built up. In general, LSPRs are observed, when the size of a structure is similar to the wavelength of the SP, whereas a semi-infinite or infinite structure supports SPPs (i.e. the size of a structure is much larger than the wavelength of the SP). In this thesis, I discuss mainly SPPs.

Obviously, surface plasmons transfer electromagnetic energy to electromechanical energy.[22] They can either concentrate or deliver energy. Therefore, surface plasmons have fascinating capabilities in energy guidance and local field confinement on the nanoscale, which fits the contemporary needs for electronic miniaturization. Plasmons have been applied in a great variety of fields[23, 24], such as light

harvesting in photovoltaics[25] and chemical synthesis,[26] cancer therapy,[27] near-field imaging,[28] nanofocusing,[29] sensing,[22] nanoantenna,[30] *etc*.
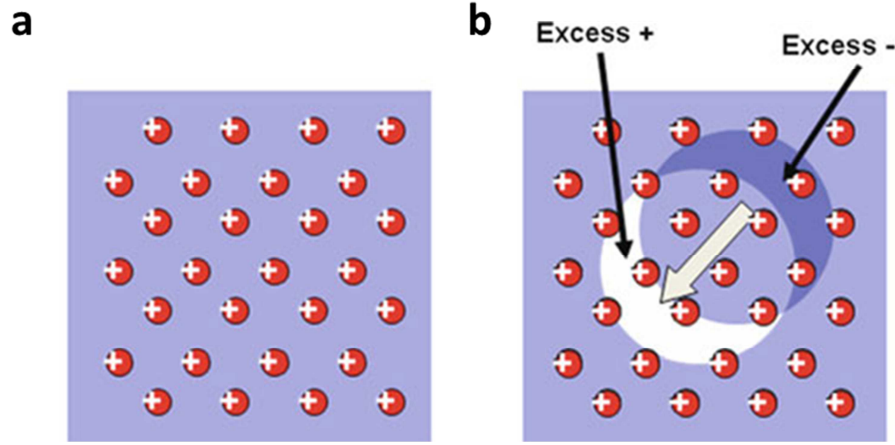
Figure 1–1. Concept of a plasma oscillation or plasmon in a metal. (a) A metal consisting of fixed positive charges (red) and an ocean of mobile electrons (lilac) at equilibrium. (b) When some of the electrons are collectively displaced, regions of excess positive and negative charge produce a local dipole moment and an associated electric field. It results in a restoring force on the electrons (grey arrow) that tends to eliminate the imbalance and restore the equilibrium state. This yields simple harmonic motion at a well-defined frequency (the plasma frequency). Reproduced from ref. [21] with permission from Springer Science+Business Media, LLC.

Maxwell´s equations

Besides describing plasmons as collective oscillations of free electrons from the view of solid-state physics, they can also be described in the framework of electromagnetism. Plasmons are in fact the response of a material against an external field for which the permittivity of the metal is responsible. The classical Maxwell theory can essentially describe the electrodynamics of plasmons in noble metals, if the energies of the investigated system are a continuum.[31] The validation counts, when the plasmon size exceeds a few nanometers.[32]

The set of macroscopic Maxwell´s equations incorporates the material intrinsic properties, i.e. permittivity ε, conductivity σ, and permeability μ:[33]

$$\varepsilon \vec{\nabla} \cdot \vec{E}(\vec{r}, t) = \rho(\vec{r}, t) \tag{1.1}$$

$$\mu \vec{\nabla} \cdot \vec{H}(\vec{r}, t) = 0 \tag{1.2}$$

$$\vec{\nabla} \times \vec{H}(\vec{r}, t) = \sigma \vec{E}(\vec{r}, t) + \varepsilon \frac{\partial \vec{E}(\vec{r}, t)}{\partial t} \tag{1.3}$$

$$\vec{\nabla} \times \vec{E}(\vec{r}, t) = -\mu \frac{\partial \vec{H}(\vec{r}, t)}{\partial t} \tag{1.4}$$

where $\rho(\vec{r}, t)$ represents free charge coming from external sources. $\vec{E}$ and $\vec{H}$ denote electric and magnetic fields, respectively.

For oscillating fields (e.g. time-harmonic electric or magnetic fields), the material permittivity ε and conductivity σ can be integrated into a single, complex quantity:

$$\varepsilon(\omega) = \varepsilon'(\omega) + j\varepsilon''(\omega) = \varepsilon'(\omega) + j\frac{\sigma(\omega)}{\omega}.$$

This frequency-dependent dielectric function $\varepsilon(\omega)$ embodies all the details of electrodynamics in metals.[33] The real part of the dielectric function $\varepsilon'(\omega)$ denotes the polarizability, whereas the imaginary part $\varepsilon''(\omega)$ represents absorption or dissipation. Note that the dielectric function may vary when the size of the material shrinks to the nanoscale. For example, the dielectric function of thin films strongly depends on the film thickness.[34]

For nonmagnetic materials, the permeability μ can be ignored; moreover, since only the electric field $\vec{E}(\vec{r}, t)$ counts for plasmon excitation (e.g. EELS measurements), merely equations (1.1) and (1.3) are important, in which the response of materials is determined by their dielectric functions.

Obviously, when the size of plasmonic structures shrinks down to below a few nanometers, quantum phenomena play an essential role. In this case, to describe surface plasmons properly, either the classical Maxwell theory with relevant corrections or the quantum mechanical treatment [35] is exerted. Several semi-classical or quantum models are thus developed, such as the nonlocal hydrodynamic model[36] or time-dependent density functional theory (TDDFT)-based calculations.[32]

Field distribution and dispersion relation of a surface plasmon polariton

In Chapter 3, surface plasmon polaritons along semi-infinite mesoscopic gold tapers are intensively discussed. This section will present the basic characteristics of surface plasmon polaritons. Considering a surface plasmon wave propagating along the x-direction at a planar interface between a metal and a dielectric, the corresponding surface charge density is polarized longitudinally as `+´ and ´−´ as shown in Figure 1–2. It thus leads to an electric field with two components, i.e. a parallel field component along the x-direction and a perpendicular component in z-direction.

The electric field along the z-direction has an evanescent character, which decays exponentially either in metal or air, i.e., it does not radiate to the far-field. The corresponding decay length is determined by the dielectric function of each medium, which is usually of the order of tens of nanometers in the optical regime.[37] On the other hand, the longitudinal x-component of the electric field demonstrates that the surface plasmon polariton is a transverse magnetic (TM) mode. The field along the x-direction will be eventually attenuated. The attenuation length (or propagation distance) is dictated by the imaginary part of the SPP propagation constant, which is on the order of a few micrometers in the visible range, and even several hundred microns in the near-infrared range.[37, 38] The lifetime of surface plasmons for silver and gold are ultrashort in the range of a few tens femtosecond.[23]
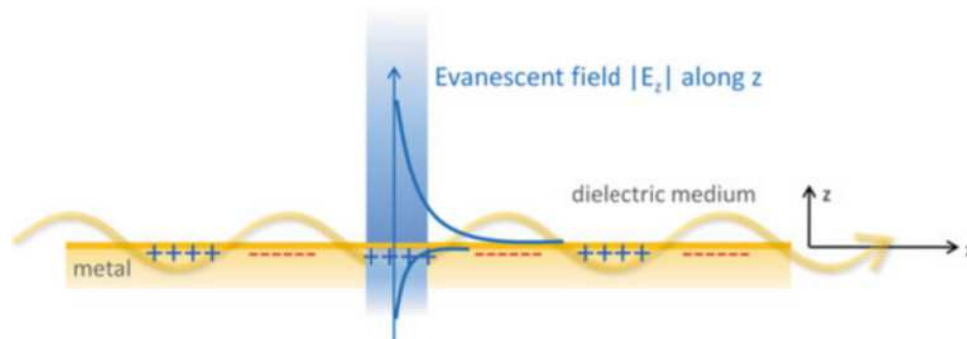
Figure 1–2. Schematic representation of an evanescent wave corresponding to a surface plasmon polariton propagating along the interface of a metal and a dielectric. Adopted from ref. [33].

Based on the description in Figure 1–2, the wave vector of the surface plasmon has two components, i.e. k_x and k_z. Because of propagation along the x-direction and decay in the z-direction, the surface plasmon polariton should possess a real k_x and an imaginary k_z. This condition leads to the dispersion

relation illustrated by the red curve in Figure 1–3 below the light line (yellow line). Taking the Drude form of the dielectric function for a metal, the asymptote of this dispersion relation reaches a frequency of $\omega_p/\sqrt{2}$, where ω_p is the plasma frequency. For details of the derivation of the plasmon dispersion relation and the relation to the corresponding dielectric function, I refer to ref. [37].

There exists another type of plasmon polaritons above the plasma frequency ω_p. In contrary to the surface plasmon polariton, this plasmon has both real k_x and k_z, which indicates the propagation in the z-direction as well (blue curve in Figure 1–3); thus such plasmons are radiative. With respect to the light line $k = \omega/c$, the evanescent surface plasmon modes lie below, whereas the radiative modes are above. If taking the absorption of materials into account, the dispersion relations of both plasmon polaritons are slightly changed due to damping (dashed red curve in Figure 1–3).

In fact, the geometry of plasmonic structures plays a key role in the dispersion of surface plasmon polaritons. For example, the curvature of cylinders changes the dispersion of surface plasmons significantly from that on a planar interface.[39] Nevertheless, the concepts of ´polarization of surface charge density wave´, ´evanescent field´, ´radiative modes´ and ´non-radiative modes´ are still applicable.
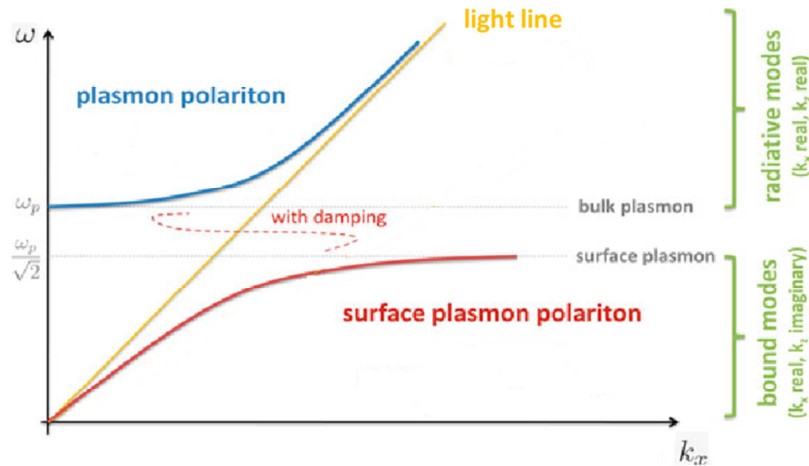
Figure 1–3. Dispersion relation of a surface plasmon propagating along a metal/air interface versus the real part of the wave vector component k_x and angular frequency ω. Dispersion line of bound plasmon modes (red curve) and radiative plasmon modes (blue curve) are apart with respect to the light cone in the vacuum (yellow line). Adopted and modified from ref. [33].

Plasmonic modes in cylinders

As a base to understand the surface plasmon modes in three-dimensional gold tapers, the surface plasmon modes in a cylindrical system are first introduced here. Figure 1–4 (a) shows the SPP modes in an infinite metal cylinder surrounded by a dielectric. They are the fundamental transverse magnetic TM modes with angular momentum order $M = 0$ and two hybrid modes with $M = 1$ and 2, respectively.[40] The propagation direction of these modes is along the cylinder axis (z–direction). However, their propagation behavior is different (Figure 1–4 (b)). The $M = 0$-mode can be excited at both small and large radius, whereas modes with higher M orders can only be excited above critical radii and evanescent propagation is not possible below the critical radii, the so-called ´cut-off radius` as marked by the black arrow in Figure 1–4 (b).
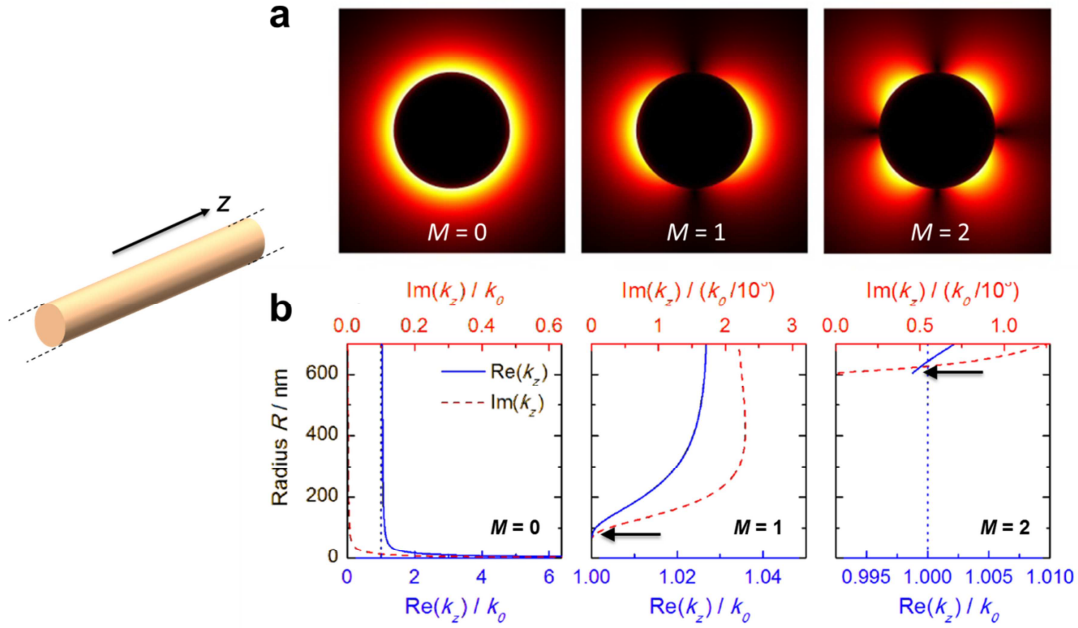
Figure 1–4. (a) Normalized electric field distributions of the three fundamental plasmonic modes in an infinite plasmonic cylinder with different M orders. M denotes the order of angular symmetry. (b) Propagation constant k_z of the three eigenmodes $M = 0, 1, 2$ of an infinitely long gold cylinder as a function of cylinder radius. The SPP frequency corresponds to a vacuum wavelength of 800 nm. Solid blue and dotted red lines represent the real and imaginary parts of k_z, respectively. Vertical dotted blue lines mark the limit of the real part of k_z, where it approaches the light line, $k_0 = \omega / c_0$. Adopted and modified from ref. [40] and [41].

Plasmonic materials

Gold and silver are the most investigated plasmonic materials due to their excellent plasmonic properties in the infrared-visible-UV frequency.[42] The surface plasmon resonances of gold and silver usually possess lower energies than the corresponding bulk plasmon energies of 2.2 eV and 3.75 eV, respectively. Gold is chemically inert; silver is prone to surface oxidization and corrosion in ambient condition. However, silver is less optically damped[23] and has no interband transitions in the visible, which is suitable for studying coupling over relatively long distances, as adopted in Chapter 4.

1.3   Toroidal moments in plasmonic nanocavities

During the last decades, toroidal moments have been drawing increasing attention in either theory and/or experiment because of their unique charge–current configurations and peculiar parity characteristics in contrast to electric and magnetic moments. However, the exploitation on toroidal multipoles is lagging behind compared to the well-known electric and magnetic multipoles, not only because of the relatively recent discovery, but also because of the challenges in experimental realization. Metamaterials have tackled the experimental problems and particularly facilitated the research on toroidal moments in the framework of electrodynamics. For more details see the brief review on toroidal moments in Section 4.2. In this thesis, I addressed the radiation properties and the coupling of magnetic toroidal moments, where the elementary toroidal dipole moment is mediated by surface plasmons and sustained in plasmonic nanocavities.

The simplest model of a dynamic toroidal dipole moment is the poloidal current model, which refers to a conventional solenoid folded into a torus, in which the currents flow poloidally around the

meridians of the torus (also see Figure 4–1 (a)).[48] To realize the excitation of toroidal moments on the nanoscale, the core idea is to mimic a surface current distribution like the poloidal currents flowing on the surface of a free-standing torus; the dual configuration is a vortex of head-to-tail connected magnetic dipoles along the meridian of the torus. A bottom-up approach is to arrange single constitutive magnetic dipoles in a circular symmetry (Figure 1–5 (a–b)).

A subwavelength hole punctured in a metal film is a good choice to sustain a magnetic dipole. As Bethe calculated early in 1944, the diffracted field (transmission) through a small hole can be considered as caused by an effective magnetic dipole in the tangential direction (in the plane of the hole) and an electric dipole in the normal direction (out of the plane of the hole).[43] It was the surface currents induced by the incident magnetic field (Eddy currents) that mainly determine the scattering properties of such a subwavelength hole.[44] Originally, the statement only accounted for the ideal case, in which the hole existed on infinitely planar, perfectly conducting, and infinitesimally thin metal film. Additionally, the diameter of the hole should be small compared to the wavelength (in the pure quasi-static regime).[43, 45] In this ideal case, the diffraction of the subwavelength hole is identical to the diffraction of its complementary structure, i.e., a nano-disc. This is called Babinet´s principle.[46] As a nano-disc supports an electric dipole (red arrow), a subwavelength hole sustains a magnetic dipole (blue arrow) as its Babinet analogue (Figure 1–5 (a)).

Under more realistic conditions, i.e. less-than-ideal metal conductivities and larger hole size (partially subwavelength), other factors begin to play a role in the transmission, such as surface plasmon and waveguiding modes.[45] Nevertheless, it was demonstrated that even under such realistic conditions a single subwavelength hole still functions as a Babinet analogue of a nanoparticle due to the small skin depths in the order of few ten nm.[44] Therefore, metals, like gold, silver and aluminum, are still considered as a reasonably good conductor at near-infrared and visible frequencies.

By virtue of the above-mentioned magnetic dipole element, a vortex of magnetic dipoles (blue arrows) can be constructed by a circle of subwavelength holes (bright contrast) in Figure 1–5 (b). A toroidal moment (green) is thus possible to be excited at the center of the topology at a certain energy. The additional hole at the center provides a loss-free region, which allows a mode with high intensity.[47] Such heptamer structures on silver thin films are also named plasmonic nanocavities. It has been demonstrated that such a heptamer nanocavity structure indeed supports toroidal moments with the fast electron excitation via the induced displacement current $j = \partial D / \partial t$.[8] Figure 1–5 (c) shows the typical electric (red) and magnetic (blue) field distributions under a toroidal moment excitation, which implements the ´poloidal current model´ on the nanoscale.

Note that in plasmonic cavity structures other modes can also be simultaneously excited by fast electrons even under a selective excitation strategy. The primary way to differentiate toroidal moment excitations from other electric or magnetic excitations is the specific resonant frequencies, which can be designed and tuned by modifying the topology of the structures from the resonances of other modes, as commonly used in metamaterial engineering.
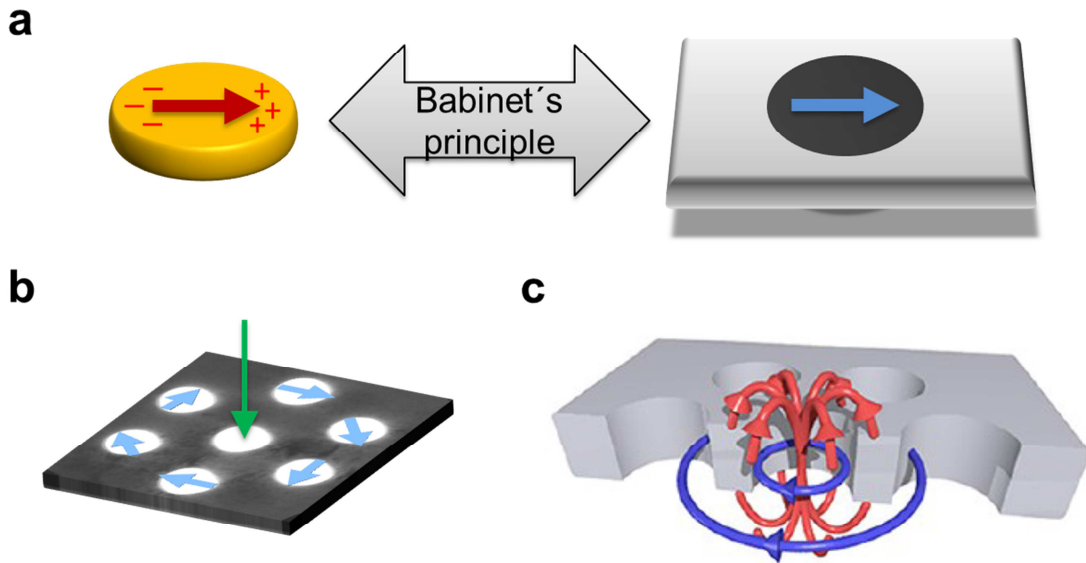
Figure 1–5. (a) A subwavelength hole as a Babinet analogue of a nano-disc. Red and blue arrows indicate an electric dipole and a magnetic dipole, respectively. (b) Construction of a vortex of magnetic dipoles (blue arrows) with a plasmonic heptamer nanocavity on a free-standing silver thin film. The green arrow denotes a toroidal moment. (c) Illustration of electric (red) and magnetic (blue) field lines strength of a toroidal mode sustained by the plasmonic heptamer nanocavity.[8] Reprinted with permission from ref. [8]. Copyright (2012) American Chemical Society.

1.4   Excitation of surface plasmons by relativistic electrons

Surface plasmons can be excited either by photons or electrons when the energy- and momentum-conservation is fulfilled. Light in the vacuum is not able to excite a SP because of deficient momentum. Solutions for increasing the momentum of light is obtained by using a denser medium (e.g. glass) or by interacting with a periodic grating. In contrary, relativistic electrons can directly excite plasmons, because they have by nature larger momentum than photons due to a non-zero rest mass (Figure 1–6 (a)).

To be more specific, fast electrons interact with plasmonic objects through the long-range Coulomb field, where the electromagnetic field linked to a fast electron indeed matters (Figure 1–6 (b)). A fast electron moving with a constant velocity through the vacuum can be regarded as an evanescent source of radiation, which decays exponentially away from the electron and cannot directly radiate to the far field. Inside the electron, the electric field is a sigularity. Outside of the electron, the intensity of the electric field decays exponentially away from the trajectory.[49] Compared to the field of an electrostatic charge, the near-field of a fast electron is relatively ´compressed´ along the moving direction (Figure 1–6 (b)). Moreover, the spectral content of a fast electron features a broadband character (from 0 eV up to several keV).[49] Fast electrons are supreme to excite both ´bright´ and ´dark´ plasmon modes, which cannot be excited by normal incident linearly polarized light due to vanishing dipole moments. On the timescale, the excitation of a SPP wave happens within several hundred femtoseconds.[23]

A swift electron acts not only as a near-field excitation source but also shares certain overlapping excitation features with various optical excitation field geometries in an ultra-broadband frequency range, such as a radial and circular far-field, and a dipolar near-field.[8] Such combined electronic and

optical characters of fast electrons allow for all manners of excitations and a comprehensive study of plasmons.[21]
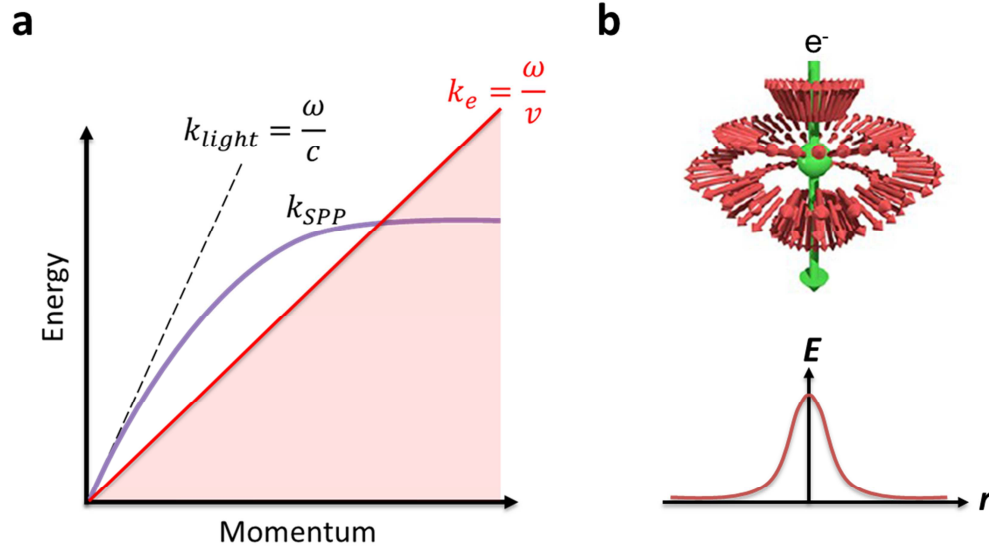
Figure 1–6. (a) Energy- and momentum-conservation for plasmon excitation: an illustration in wave-vector–frequency diagram when an electron moves parallel to a metal surface. Curve k_{SPP} presents a typical dispersion of a planar SPP; curve k_{light} denotes the dispersion of light in vacuum; and k_e is the upper dispersion limit of the wide distribution of the related electromagnetic field of a fast electron with velocity v. (b) The electromagnetic-field components surrounding a relativistic electron with the illustration of the evanescent field distribution underneath. Reprinted with permission from ref. [8]. Copyright (2012) American Chemical Society.

1.5   Energy loss of fast electrons

During the process of surface plasmon excitation, the near-field of the fast electron polarizes the surface-near region of a plasmonic object. The polarization causes a scattered electromagnetic field around the plasmonic object which can act back on the fast electrons. The work of the scattered field done on the fast electron leads to an energy loss, which can be calculated by integrating the corresponding Lorentz force over the electron travelling path:

$$\int_{path} dt \, e(\vec{E}(r,t) + \vec{v} \times \vec{B}) \cdot \vec{v} \tag{1.5}$$

$\vec{E}(r,t)$ is the electric field of the scattered field and $\vec{B}$ is the magnetic field. They both depend on distance r and time τ. Note that the scattered field includes all the excited plasmonic modes.

However, only the electric field contributes to the energy loss of the fast electron, since the term $(\vec{v} \times \vec{B}) \cdot \vec{v}$ is zero.[4] As a result, one can say in turn that the energy losses of fast electrons indicate the electric field of the excited plasmons projected along the electron trajectory.

1.6   Characterizing surface plasmons using relativistic electrons

Owing to the particle–wave duality character, relativistic electrons possess wave character with very small wavelengths. For example, a 200 keV electron has a de Broglie wavelength of 2.51 pm. This offers tremendous advantages in interacting with nano-size plasmonic objects. Combined with the unique broadband excitation features of fast electrons, electron microscopy and spectroscopies have

therefore become an unprecedentedly powerful tool to excite,[50] manipulate[51] and characterize plasmons[52] in nanoscale objects (see Chapter 2).

EFTEM and low-loss EELS using relativistic electrons are among the pioneering experimental methods to characterize plasmonic modes of metallic structures on the nanoscale in a broad energy spectral range.[8, 53-55] In both techniques, the energy losses of the exciting fast electrons quantify the characteristic energies of the excited plasmonic modes because of energy conservation. The counts of the electrons at each energy loss are recorded as ´intensity´ in the energy-loss spectra and in the EFTEM images. This parameter symbolizes the energy-loss probability, which is related to the induced electric field along the electron trajectory. It is expressed as follows[56]

$$\Gamma_{EELS}(\omega) = \frac{e}{\pi\hbar\omega} \int dt \, Re\{e^{-i\omega t}\vec{v} \cdot \vec{E}^{ind}[\vec{r}_e(t),\omega]\} \quad (1.6)$$

where Γ_{EELS} is the loss probability per electron per unit of transferred frequency ω. E is the induced field of all the excited plasmonic modes projected along the electron trajectory. v is the velocity of the primary fast electron. From this equation, one can see that a higher intensity in energy-loss spectra or EFTEM images indicates a stronger plasmonic field.[56, 57] Furthermore, it is usually stated that EELS has a direct relation to the photonic local density of states (LDOS) projected along the trajectory of the electron beam.[56] More precisely, it is the local electromagnetic density of states of the material that is measured.[20] A broad overview on the applications of electron energy-loss related techniques on plasmonic systems can be found in ref. [58] and [59].

Instead of measuring the energy losses of incident electrons, the detection of the radiation from plasmon decay is another way to characterize surface plasmons.[5, 16] This probing technique is called cathodoluminescense spectroscopy (CL). CL has been applied to study the far-field radiative behavior of an object under local electron excitation. The comparison between CL and EELS in the aspect of data interpretation has been extensively investigated in ref. [17], [20], and [60], but it is still ongoing. In simple words, CL shows only the radiative loss of the excited plasmons, whereas EELS gives a summation of both the radiative and the dissipated losses. Due to the plasmon damping as inherent in metals, CL and EELS spectra of identical plasmonic structures generally show slight discrepancies.[60, 61]

For a brief technical comparison between EELS, EFTEM and CL I refer to Section 2.2. Keep in mind that in these techniques the excitation of plasmonic modes in objects depends on the impact positions of the incident fast electrons.[61] It may excite different types of plasmonic modes or change the relative weight between the excited modes.

Not limited to the fundamental measurements as mentioned above, characterization techniques have been developed to resolve more useful information in parallel. For instance, the momentum-resolved EELS collects signals in both frequency and momentum domain in which the propagation or radiation behavior of plasmonic modes can be read out easily. In CL this is accomplished by the so-called angle-resolved CL,[19] which measures the direction of the emitted light and gives an access to the momentum of the radiation-coupled plasmons.[62] Not only that, more advanced developments, like EELS tomography[63] and both angle- and polarization-resolved CL,[64] have been employed to understand plasmonic excitations in three dimensions and to differentiate multiple plasmonic modes that are spectrally or spatially overlapped. Also time-resolved EELS and CL techniques have been developed to study the dynamics of the interaction process and of light emission.[65-67]

1.7   Simulating electron energy-loss spectra

In this thesis, the electron energy-losses are simulated by solving the full Maxwell´s equations in two steps within the non-recoil approximation.[57, 68, 69] The electromagnetic field attached to a fast electron is first employed to excite the investigated structure, while assuming that the fast electron moves with constant velocity along a straight-line trajectory. Secondly, the scattered field reemitted from the excited structure exerts a force on the fast electron, causing energy losses. The energy-loss possibilities of the fast electron in the frequency domain, which is relevant to EELS experiments, are then derived according to this work, as shown in equation (1.6).

As seen, this approach reduces the problem of calculating the loss probability to solving the scattered electric field induced by the fast electron. The induced magnetic field does not contribute to the loss probability as explained in Section 1.5. To solve the induced electric field of the structure, the dielectric functions of the materials at specific frequencies are necessary parameters to obtain the electromagnetic response. In this thesis, the experimental dielectric function of gold or silver is adopted from ref. [70].

1.8   Outline of this thesis

In Chapter 2, the fabrication methods, characterization techniques, and data processing will be introduced in detail. Figure 1–7 shows the topics which are covered in Chapter 3 and 4. In Chapter 3, the plasmonic modes in tapered gold tips will be comprehensively studied. I will show the mode mapping by EELS and EFTEM in the proximity to taper apices, where the transformation between localized and propagating surface plasmons occurs. Then I will discuss the corresponding dynamic resonance mechanisms with fast electrons, reflection and phase-matching, and how to differentiate them. Later, the far-field radiation properties of the surface plasmons in gold tapers investigated with CL will be shown to understand more about the photon emission of tapers. In Chapter 4, a brief review of toroidal moments will be provided. Then I will show the far-field radiation measurement of a single toroidal dipole moment sustained on a plasmonic heptamer nanocavity. Later, the fundamental dipole– dipole coupling in the family of dynamic toroidal moments will be discussed based on both experimental and theoretical results. In Chapter 5, the conclusion of this thesis will be presented.

Low-loss EELS & EFTEM

CL
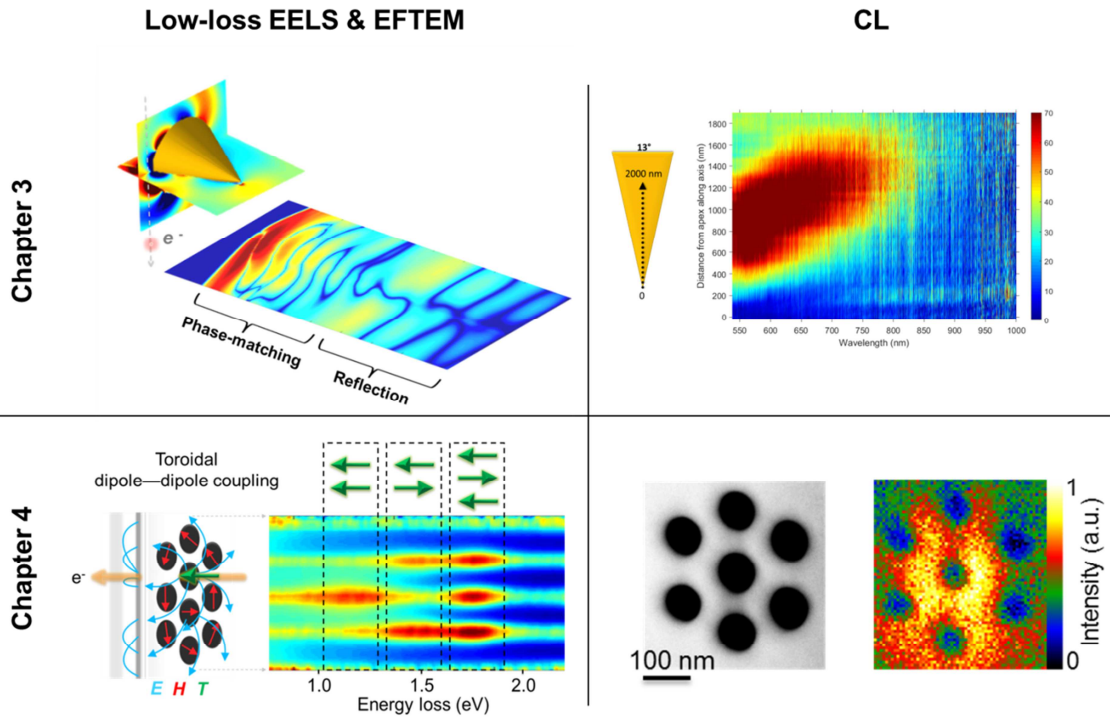
Chapter 3

Chapter 4

Figure 1–7. Sketch of the outline of the investigations presented in Chapter 3 and 4.

This page intentionally left blank

Chapter 2   Experimental methodology

In this thesis, the plasmon properties of single-crystalline gold tapers and the toroidal moments sustained by the plasmonic nanocavities on silver thin films were primarily investigated. To characterize the spatial, spectral and radiative properties of plasmons on the nanoscale, several electron-microscopy-pertinent technologies are used, namely, energy-filtered transmission electron microscopy (EFTEM), electron energy-loss spectroscopy (EELS) and cathodoluminescence spectroscopy (CL). The following two electron microscopes were used to perform those spectroscopic techniques.

The Zeiss Sub-Electron-Volt-Sub-Angstrom-Microscope (SESAM), a 200-kV Schottky field-emission gun (FEG) TEM microscope equipped with a symmetric electrostatic Ω-type monochromator (CEOS Heidelberg) and the in-column MANDOLINE energy filter. This microscope was used to perform EFTEM and EELS measurements.

A Vacuum Generator HB-501 scanning transmission electron microscope (VG Cold) equipped with a cold-field emission electron gun. CL measurements were carried out at an operation voltage of 100 kV. The electron probe has a current of around 1 nA and a size of a few nanometers. The solid detection angle is 1.2 π sterad.

2.1   Sample preparation

Free-standing specimens are favorable for surface plasmon studies because it avoids damping or modification of plasmon resonances at the interface.[71] Moreover, smooth surfaces minimize SPP scattering during propagation. Therefore, free-standing gold tapers and silver thin films with smooth surfaces were prepared for the study of this thesis.

2.1.1   Single crystalline gold tapers and gold nanowhiskers

Single crystalline gold tapers are fabricated by the method of electrochemical etching and were provided by our collaborators.[72] Gold tapers were glued on the edge of a ϕ = 3.05 mm TEM copper ring, with the tips located at the center of the ring. The glue was mixed with carbon powder to be conductive.

On the other hand, free-standing, high-aspect ratio, single crystalline gold nanowhiskers were fabricated from polycrystalline tungsten wires using a high-temperature molecular beam epitaxy method by another collaborator.[73] Au was deposited on the tungsten substrate at 680°C using an effusion cell.[74] A tungsten wire with epitaxially grown gold nanowhiskers was immersed in an ethanol solution and received ultrasonic vibration for a few minutes. In this way, gold nanowhiskers were dropped off from the tungsten substrate and suspended in the ethanol solution. The gold nanowhiskers were then transferred to lacey-carbon-coated TEM grids by dropping ethanol solution droplets on the TEM grids.

2.1.2   Plasmonic nanocavities in silver thin films

Plasmonic cavities were nanostructured by a FIB in smooth and free-standing poly-crystalline silver thin films. The grain size is of the order of hundred μm. As shown in Figure 2–1 (a–c), the preparation for free-standing poly-crystalline silver thin films is as follows: i) Silver discs with 3 mm diameter were punched out from annealed silver sheets. ii) The discs were electropolished by using a cyanide-free solution[75] until a hole was generated in the center of the disk (Struers Tenupol 5 electrolytic

polisher). The voltage and flow rate were set to 20 V and 23 (arbitrary units as indicated on the electrolytic polisher), respectively. iii) Each specimen was ion-milled at a low energy for final cleaning (at 0.5 kV for 30 min, Gatan Precision Ion Polishing System II Model 695). A double beam was used at a milling angle of 6°. After electropolishing the rim of the holes in the silver discs became thinner than 100 nm, as the area with brighter contrast shown in Figure 2–1(c).

Plasmonic cavities were patterned by a focused Ga+ beam (ZEISS 1540EsB Crossbeam) on the thin rim area (Figure 2–1(d)). A low ion dose was used to minimize the possible ion implantation damage (less than 20 pA at 30 kV for the ion beam and the exposure time for each cavity structure was at maximum a few seconds).
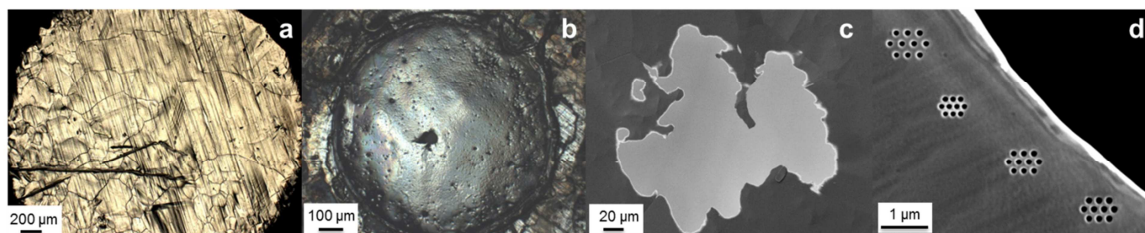
Figure 2–1. (a) Optical image of a flat 3 mm silver disc after punching out. (b) Optical image of a silver disc after electropolishing. (c) Secondary electron image of a hole after ion milling. (d) Plasmonic nanocavities patterned by FIB at the thin rim area of (c). The edge of the hole is bent due to strain induced by ion bombardment.

2.2   Characterization methodology

As mentioned in Chapter 1, fast electrons have several unique features in investigating plasmons:

i. Nanometer-scale spatial resolution, as the wavelength of electrons is just a few picometer at high voltages (usually 60-300 kV);

ii. An ultra-broadband excitation from meV to thousands of eV because of the short impact time;

iii. Adequately large momenta of the electric near-field to couple to surface plasmon polaritons.

The interaction between fast electrons and a thin specimen is selectively illustrated in Figure 2–2. First, the impact of electrons on the specimen could cause transient photon emission in the visible spectrum. This radiation is called cathodoluminescence, which might be due to bremsstrahlung, transition radiation or plasmon-mediated photon emission, *etc*. These emitted photons are collected in CL measurements. The incident fast electrons interact with the electrostatic potential of the atomic nuclei and electrons of the specimen through the Coulomb field while transmitting the specimen. Some incident electrons pass through the specimen without scattering (so-called ´direct beam´); some undergo inelastic scattering by losing certain amounts of energies, which usually has a small scattering angle on the scale of 10 mrad off the optical axis and holds rich information about the specimen including plasmon excitations. These electrons are utilized for EFTEM and EELS characterization. Some electrons are scattered by the atoms to higher angles (> 50 mrad off axis), which can be used to distinguish atoms of different atomic number from the image contrast.[76] These electrons form so-called high-angle annular dark field (HAADF) images.
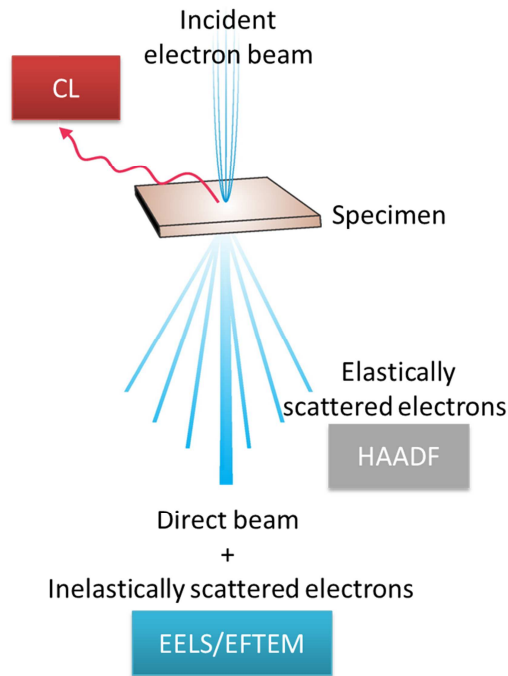
Figure 2–2. Sketch of the interaction between the electron beam and the specimen. Only the techniques related to this dissertation are labeled, together with their electron or photon sources.
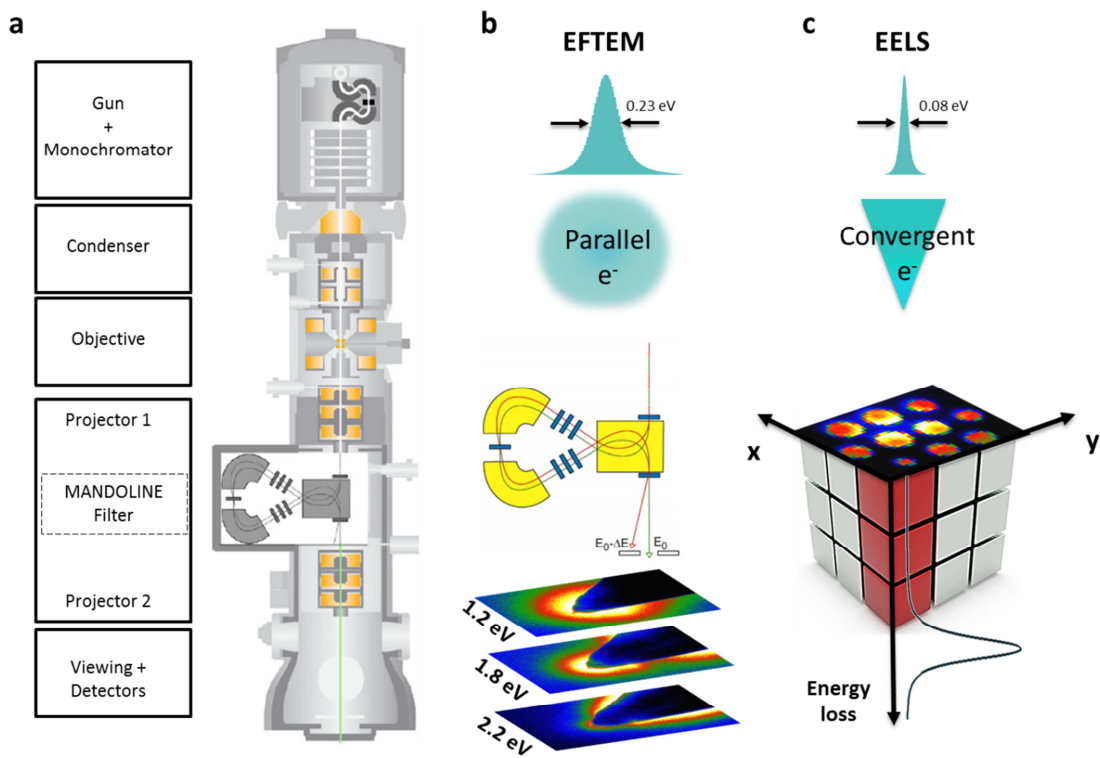
Figure 2–3. Schematic illustrations for (a) the SESAM optical column, (b) EFTEM and (c) EELS techniques. The sketch for the SESAM column is adapted from ref. [77]. In (c) the pixel size is exaggerated compared to the displayed image.

EFTEM, EELS and CL are used for different investigation purposes. EFTEM allows to image the spatial distribution of a selected energy range with high spatial resolution in a reasonably short time; EELS is utilized to map both radiative and dark plasmonic eigenmodes with high spectroscopic resolution. The far-field radiation properties of plasmonic objects can instead be accessed by CL. Usually in STEM mode, elastically scattered electrons with high-angle deflection are detected to form HAADF images to give a morphologic image in parallel to the spectroscopic measurement.

Some fundamentals of the transmission electron microscope are explained based on the optical column of the Zeiss SESAM, as shown in Figure 2–3 (a). It consists of 5 system blocks and the in-column energy filter ´MANDOLINE`. Starting from the top, electrons are generated by a Schottky field-emission gun and narrowed in energy width through a monochromator. The condenser system is used to form the shape of the electron beam when illuminating the specimen. It differentiates the TEM mode with a field-of-view illumination from the STEM mode with a convergent beam. After passing through the specimen, sitting between the objective upper and the lower pole pieces, the incident electrons can be either transmitted without interaction with the specimen, or scattered either elastically and/or inelastically by the nuclei and electrons in the specimen. The unscattered electrons are used for ´bright-field´ imaging, the deflected electrons for ´dark-field´ imaging. Inelastically scattered electrons experience energy losses within the specimen, whereas elastically scattered electrons preserve the energy. The objective lens focuses parallel direct or diffracted beams transmitted through the specimen and forms a diffraction pattern and a first magnified image which is further magnified by the projector lenses. An energy filter (spectrometer) is the key element for electron-energy resolved methods, such as EFTEM and EELS. The MANDOLINE filter is located within the projector system as shown in Figure 2–3 (a). It consists of multipole magnets and the magnetic field inside deflects the electrons differently depending on their speeds. For EFTEM a slit with a certain width is used at the exit plane to select electrons which have suffered a specific energy loss and an image is formed from these electrons. The image is recorded by a CCD camera located at the end of the microscope column.

2.2.1 Energy-filtered transmission electron microscopy series acquisition

Figure 2–3 (b) illustrates the EFTEM technique in the SESAM as used for our experiments. A parallel monochromated electron beam with a 0.23 eV full-width at half-maximum (FWHM) of the zero-loss peak (ZLP) illuminates the specimen. Both elastically and inelastically scattered electrons enter the MANDOLINE energy filter and are sorted according to their energy losses at the filter exit plane. At the same plane, an exit slit with 0.2 eV energy width is inserted to select the electrons with the desired energy loss for forming an energy-filtered TEM image. By sequentially shifting the accelerating voltage with a step of $\Delta E = 0.2$ eV, a series of energy-filtered TEM images are thus acquired. Such an EFTEM image series constitutes a 3D data cube, with 2D highly sampled images and 1D roughly sampled energy-loss spectra.

2.2.2 Electron energy-loss spectroscopy

In contrast to EFTEM, EELS offers a very high sampling in energy space. In STEM–EELS, a convergent electron beam with energy resolution below 0.1 eV is focused onto the specimen. This electron probe is then scanned across a region of interest covering $N \times M$ pixels. At each pixel an EELS spectrum is recorded with a typical dwell time of 0.2–0.8 s. In this case, the spatial resolution is determined by the size of the electron probe and the beam broadening in the specimen (here a few nm). The energy dispersion can be as small as 0.003 eV per CCD pixel. The scan is performed either along a line (line scan) or across an area (mapping). Figure 2–3 (c) shows a 2D STEM–EELS mapping, with a pixelated image in *xy* plane and an EEL spectrum in *z* direction at each single voxel.

For STEM-EELS measurements, a semi-convergent angle of 7 mrad and a semi-collection angle of 6.5 mrad have been used.

2.2.3   Cathodoluminescence spectroscopy

The CL measurements were performed using a VG HB-501 scanning transmission electron microscope at the Laboratoire de Physique des Solides, Université Paris Sud, Orsay, France (Figure 2–4 (a)).[5] The acceleration voltage was 100 kV and the electron probe current was around 1 nA. Data were acquired in the so-called spectral image mode (SI), in which the electron beam scans a certain area of the sample. At each pixel, the emitted photons are collected by the parabolic CL mirror and deflected to an external spectrometer. Simultaneously, the HAADF image is recorded. At the end of the scan, both the spectral image and the HAADF image can be compared pixel per pixel (Figure 2–4 (b)). Dwell times per pixel were 50 or 1000 ms and the pixel size was 18 × 18 nm. A monochromatic photon map at a certain wavelength (or energy) can be visualized as a 2D image extracted from the acquired 3D spectral image data set (Figure 2–4 (b), middle).[18]

Although the acceleration voltages in CL and EELS measurements are different (100 and 200 kV), it does not affect the plasmon peak position.[15] However, the relative intensities of the multipole modes are affected by the acceleration voltage. With increasing electron velocity, the ratio of the radiative loss probability between the dipole mode and quadrupole mode increases.[15]
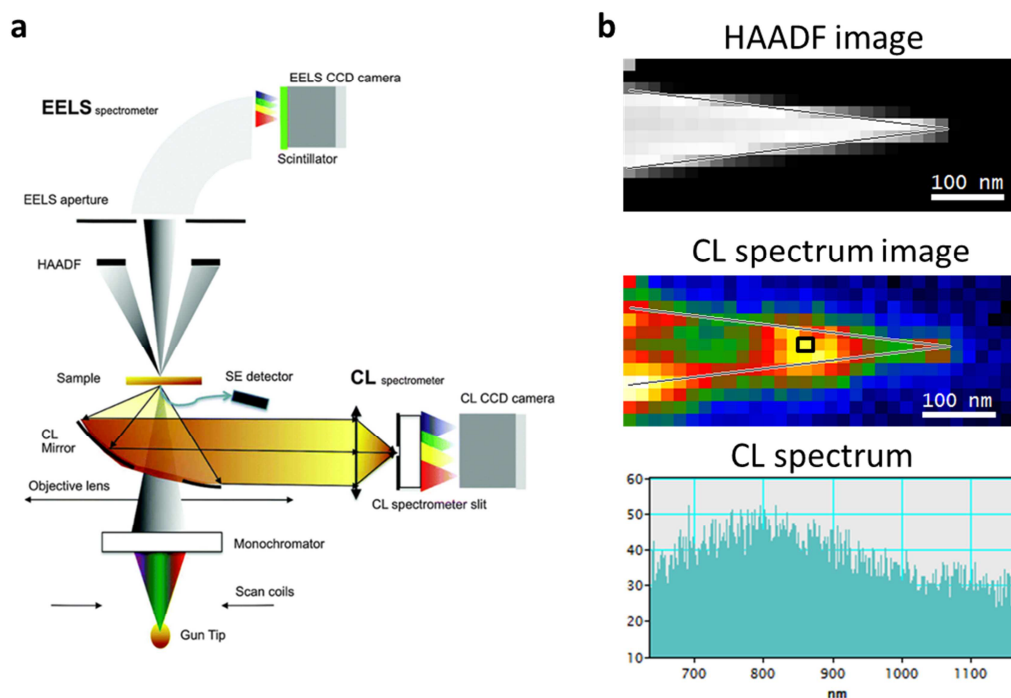
Figure 2–4. (a) Sketch of the set-up for STEM–CL measurements in a VG microscope.[3] (b) An exemplary data set of a CL measurement, including the simultaneously acquired HAADF image and the CL 2D spectrum image. A CL spectrum extracted from a single pixel (highlighted by the black box in the middle) is displayed at the bottom.

2.3   Data processing

In this thesis, three types of spectrum data, EFTEM series, EEL and CL spectra, need processing. Overviews of the processing flows for each data type are presented in Figure 2–5. A fundamental step

is spectrum calibration, including assigning the correct zero-energy (or zero-wavelength) position and the correct spectrum dispersion. For processing EEL spectra or EFTEM images, the ZLP-related correction is the major part; for processing CL data, more steps are taken, for example, reducing noise via principal component analysis (PCA), correcting the spectral collection coefficient of the CL spectrometer at different wavelengths, subtracting the background noise extracted from vacuum and smoothing the processed data. Each processing step is described in the following sections.
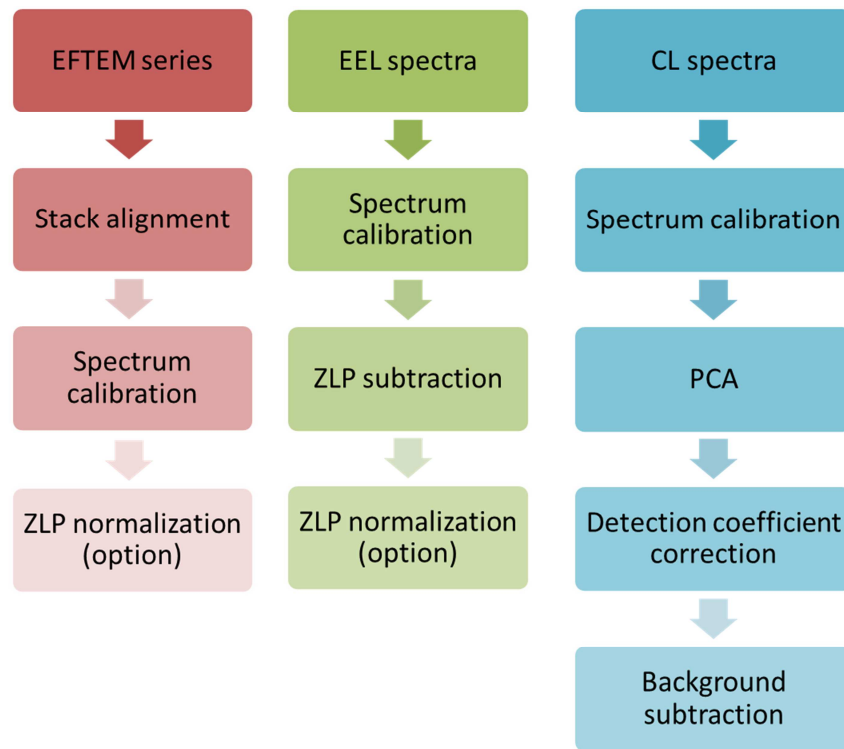
Figure 2–5. Overview for EFTEM, EELS and CL data processing, respectively.

2.3.1 Zero-loss peak subtraction and normalization

The low-loss EEL spectrum includes the ZLP and plasmon peaks (grey area in Figure 2–6 (a)). However, the intensity of the ZLP is overwhelmingly higher than the intensity of the plasmon peaks. To make plasmon peaks clearly visible, the ZLP needs to be subtracted from the EEL spectra for further analysis. For this purpose, the tail of the ZLP is fitted by a power-law function, as indicated by the red line in Figure 2–6 (a). The green line shows the signal of the plasmon peaks after ZLP subtraction.

Additionally, ZLP-normalization is applied to eliminate the EELS intensity fluctuation caused by different specimen thickness in the scanned area. In this process, the contribution of the elastic zero-loss peak is firstly subtracted from a spectrum by a power-law fit and the remaining spectrum is normalized by dividing by the maximum intensity of the ZLP. Taking a plasmonic nanocavity as an example (Figure 2–6 (b)), the EELS linescan was conducted along its central axis. Both the zero-loss intensity and the plasmon intensity differ strongly between the measurements in the hole (black contrast) and in the silver film (white contrast) due to elastic scattering in the silver film. This makes the spectrum almost invisible in the thick areas between the holes in the ZLP-subtracted spectrum. Only after ZLP-normalization the EELS intensity becomes visible in all areas.
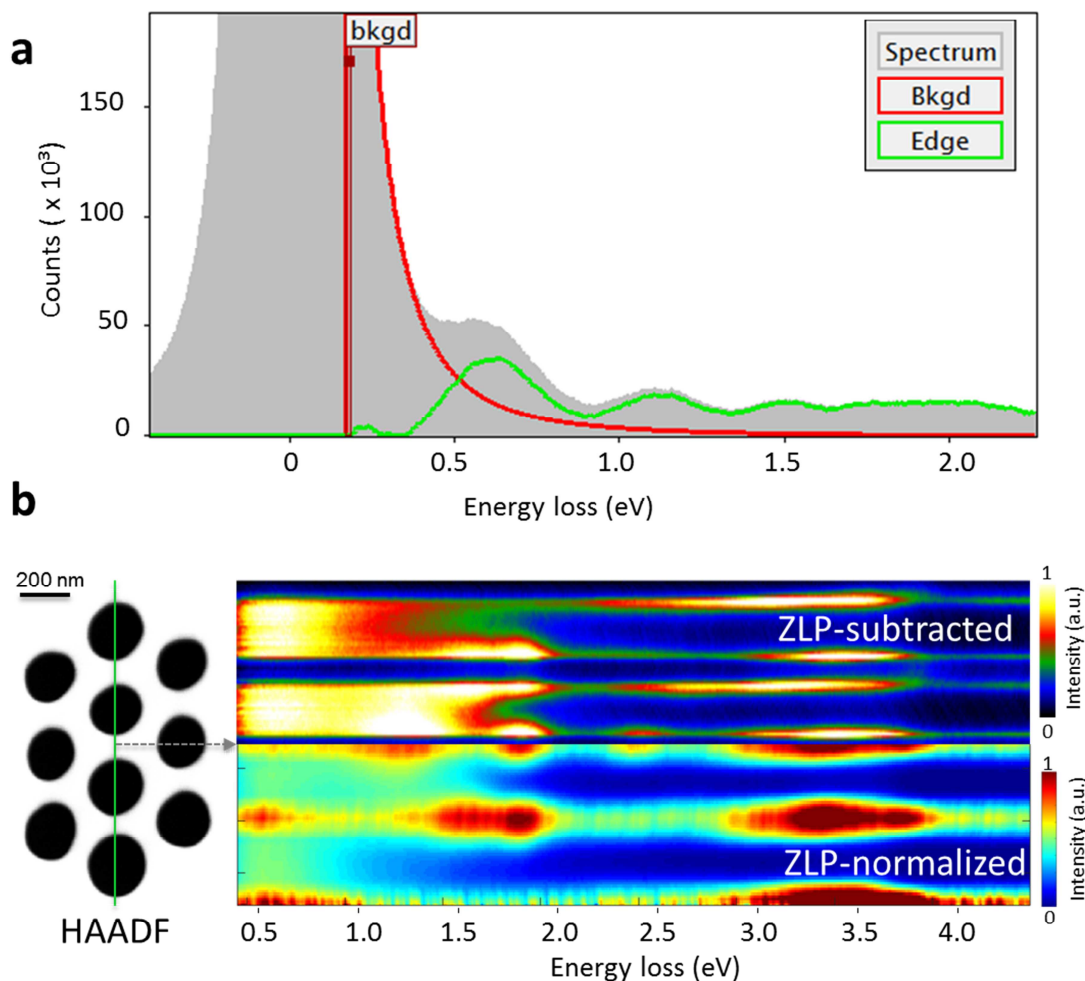
Figure 2–6. (a) Illustration for ZLP-subtraction in a low-loss EEL spectrum. The grey area denotes an EEL spectrum including the ZLP and the plasmon peak. The red line indicates the power-law fitted for the tail of the ZLP. The red curve shows the spectrum after ZLP-subtraction. (b) Comparison between the ZLP-subtracted and the ZLP-normalized EEL spectra. Left panel shows the HAADF image of a plasmonic nanocavity, where the EELS linescan was conducted along the central axis as the green line indicates.

2.3.2 Principal component analysis

Principal component analysis (PCA) is a decomposition algorithm applied as a means of noise reduction. This analysis is performed based on the open source Python library HyperSpy V0.8.1.[78] PCA sorts the components in the data in order of decreasing variance and generates a logarithmic plot of the variance against the component index. The plot can provide a good estimation of how many components contain meaningful signal and the rest is considered as noise which can be discarded. The components containing signals are then selected for reconstructing the original signal.

As demonstrated in Figure 2–7, the noise in the CL spectrum is much reduced after PCA processing. The spectrum can be further smoothened by the Savitzky–Golay smoothing algorithm, which is based on fitting local polynomials to segments of the data. This method seeks to preserve shapes of peaks.[79]
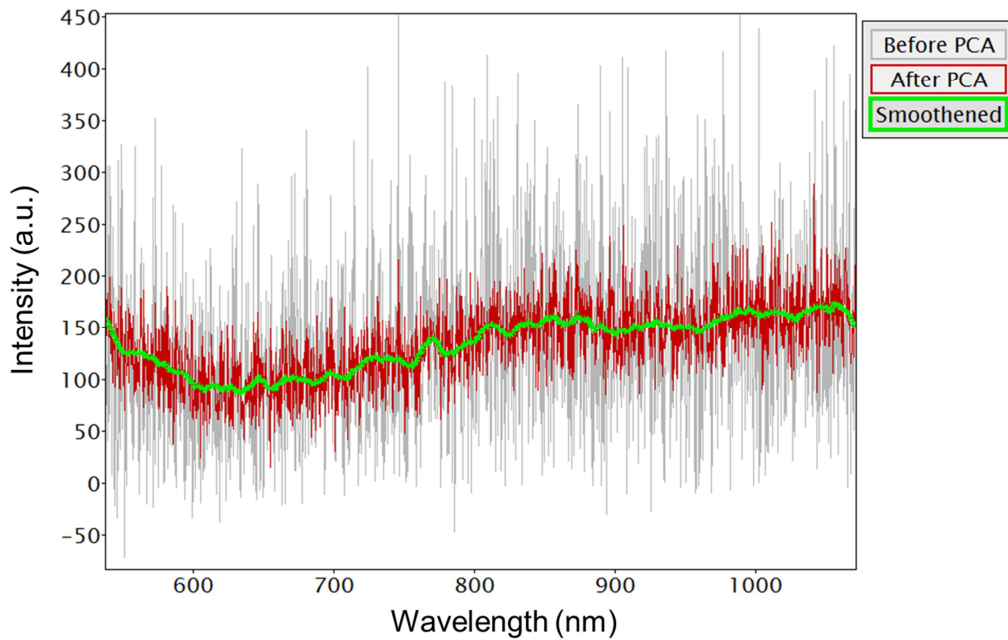
Figure 2–7. A raw CL spectrum (grey) after PCA process (red), and then further smoothened (green).

2.3.3 Detection coefficient correction for cathodoluminescence spectrometer

The CL spectrometer is sensitive to light with wavelengths smaller than 800 nm only. This leads to diminishing detection intensity at wavelengths larger than 800 nm (Figure 2–8 left). Therefore, the wavelength-dependent detection coefficient of the spectrometer needs to be considered and calibrated before interpreting CL data.

A light source with a known emission spectrum is used as a reference. The detection coefficient of the spectrometer is calculated as the ratio between the measured and the known emission spectrum. The acquired CL spectra are then corrected by dividing by the detection coefficient.
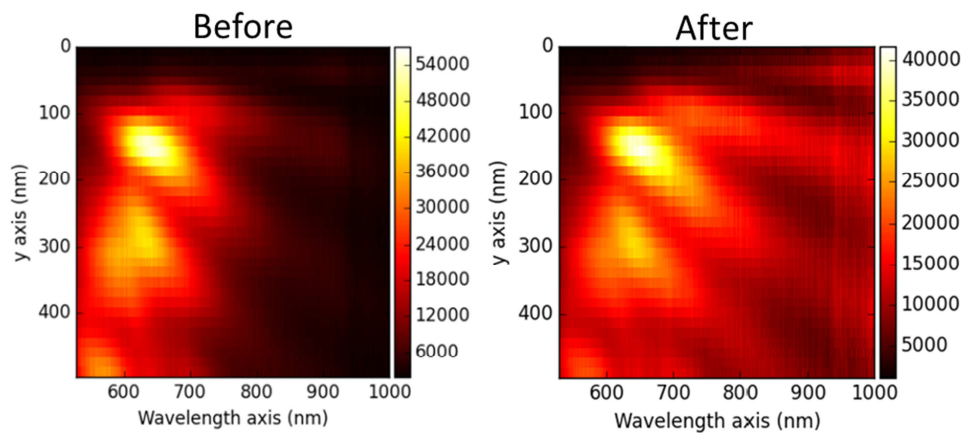
Figure 2–8. A distance–wavelength CL map before (left) and after (right) detection coefficient correction for the CL spectrometer (courtesy of Alfredo Campos at University Paris Sud).

Chapter 3   Plasmonic properties of gold tapers

3.1   Introduction

Abbe´s diffraction limit points out that the wavelength of any light source restricts the focused size whose radius is roughly half of the wavelength.[80, 81] It poses a limit on the achievable light–matter interaction. As nowadays the need for miniaturization of electronic devices (e.g. integrated circuits) steeply grows, guiding and focusing light on the nanometer scale is necessary. Plasmonics is very promising to tackle this question on the nanometer scale, because it provides electron mechanical oscillations as an alternative approach to focus optical energy, out of the box of the diffraction restriction.[22]

Plasmons in metallic structures provide a way to transfer and to concentrate electromagnetic energy effectively in nano-scale regions through collective oscillations of free electrons in metals.[29, 82-84] One of the most common and simple structures, with concomitant capabilities of nanofocusing and field enhancement, are conically-shaped metallic tapers (Figure 3–2 (a)).[82, 83] It was inspired by the lightning-rod effect and proposed to apply in the near-field optical microscopy.[85, 86] Such tapers support SPPs along the shaft and the transformation to LSPs at the apex (Figure 3–1 (a)). They can serve either as waveguides or nanoantennas[87, 88] in apertureless scanning near-field optical microscopy[89-92] and ultrafast photoelectron emission.[30, 93-96] Due to their importance in diverse nanophotonic applications, several different characterization techniques and numerical methodologies have been employed to further understand the excitation, propagation, and nanofocusing of electromagnetic energy by such metallic tapers.[41, 65, 72, 89, 92, 97, 98]

A comprehensive understanding of SPPs sustained by conical gold tapers, especially the nonlocal behavior of excited modes, like their corresponding phase constant and attenuation, is requested for better manipulation and application purposes. As already known, a radially symmetric SPP mode (the fundamental TM mode with vanishing angular momentum, $M = 0$) is supported by tapers to achieve adiabatic nanofocusing.[90] On the other hand, higher-order modes with larger angular momenta are strongly coupled to the radiation continuum at critical radii, and thus cannot be preserved at the apex.[41, 97] The behavior of all these modes can be significantly tailored by the geometry of gold tapers, such as the opening angle and the radius of curvature at the apex.[99] In Section 3.2, the surface plasmonic modes of gold tapers near the apex were revealed by EELS and EFTEM with high spatial resolution. These different resonant modes were not distinguishingly observed by conventional optical microscopy due to the resolution limit.

The main object of this chapter is to clarify the physics for the observed EELS signals as discussed in Section 3.3. In 2015 two papers[93, 97] reported on the investigation of surface plasmons on three-dimensional, single-crystalline gold tapers with different opening angles using EELS. Signatures of multiple plasmonic modes were observed as resonances in the EEL spectra in both studies. Although the experimental results in both studies showed important similarities, the suggested mechanisms behind the observed resonances were fundamentally different. One interpretation, based on studies of tapers with small opening angles, suggested that the EELS signatures of the investigated tapers were due to the interference between the forwardly propagating fundamental azimuthal surface plasmon polariton mode ($M = 0$ with radial symmetry) and its reflection from the apex (Figure 3–1).[93] Another interpretation, based on studies of tapers with larger opening angles, suggested that EELS resonances were consequences of the phase matching between the exciting electron wavepacket and the electric field re-emitted by higher M-order modes of the taper (Figure 3–1).[97] In other words, the swift electron

dynamically interacts with plasmonic modes of the taper and experiences a force induced by the electromagnetic field re-emitted by those modes. Hence, a maximum, or scattering resonance, appears in the EELS signal whenever the electron self-interferes constructively with the electromagnetic field re-emitted by the excited plasmon modes. Both interpretations matched well with the corresponding numerical simulations of Maxwell's equations for the corresponding taper geometries in the time domain. Very recently, an analytical model for the EELS spectra of conical metal tapers has been introduced[98] that confirmed the occurrence of these two different mechanisms in cylindrical nanostructures. In Section 3.3, plasmonic tapers of varying opening angles were systematically investigated by using both EELS and numerical FDTD simulations. It shows that for all tapers both phase matching and reflection contribute to the EELS signals. For small taper angles, the apex reflection of the SPP wavepacket launched by the swift electrons dominates. The resulting interferogram is highly sensitive to the temporal chirp of the time-delayed SPP wavepacket. For large taper angles, however, apex reflections contribute less and the excitation of higher-order angular momentum modes of the taper gives rise to resonances in the EEL spectra.
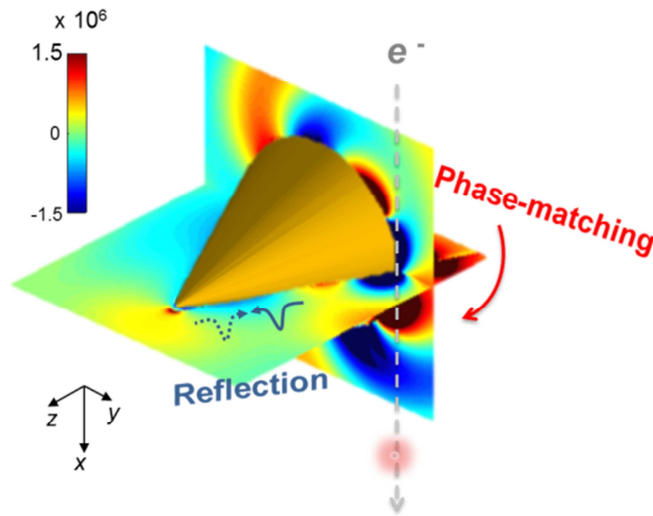
Figure 3–1. Schematic drawing of the dominant optical modes of a gold taper excited by a relativistic electron. The passing electron excites both evanescent SPP modes and radiative, higher-order angular momentum modes. Only the lowest order, $M = 0$, SPP mode of the taper is guided towards and reflected at the apex. It gives rise to a time-delayed evanescent field, acting back on the electron and inducing reflection resonances in the EEL spectra. In contrast, the excitation of radiative, higher-order angular momentum modes of the taper induces the emission of electromagnetic fields. Their back-action on the passing electron leads to phase matching resonances in the EEL spectra. The corresponding electric field distributions in both *xy*- and *yz*-planes are presented, as well as the *x* component of the Fourier-transformed oscillating electric field associated with the exciting electron at the corresponding energy.

To further study the influence of SPPs modes with different *M*-orders on the light emission of gold tapers, the radiation properties of gold tapers were investigated experimentally by CL and numerically by FDTD simulations of Maxwell´s equations. In Section 3.4, CL measurements on gold tapers with 13° and 47° opening angles are present in the wavelength range of 540 to 900 nm. The related emission mechanisms in this plasmonic taper structure are first introduced. Then the experimental observations of the 13° taper are present and further discussed parallel with the numerical results. At the end, a comparison of the CL spectra of the 13° and the 47° tapers is presented and discussed.

3.2 Plasmonic modes of gold tapers

EELS and EFTEM measurements reveal multiple plasmonic modes of a taper structure near the apex in a very broad spectral range (Figure 3–2 (b-f)). The multiple plasmonic modes can be catalogued into two groups presenting different characteristics. First, the discrete resonances along the shaft become asymptotic toward the apex in the distance–energy EELS map (Figure 3–2 (c), corresponding to the linescan 1 in (b)). Specifically, these resonances are blue-shifted towards the bulk plasmon energy of 2.2 eV when the distance from the apex decreases (Figure 3–2 (e)). Interestingly, the tendency of these resonances can be represented by an empirical hyperbolic function in a form of $E = \kappa/(L + L_0)$, where κ and L_0 are fitting parameters (details see Section 3.3). In contrast, a localized single broadband resonance is observed at the apex. An EELS linescan perpendicular to the taper axis in front of the apex can exclusively resolve the localized mode at the apex (Figure 3–2 (d), corresponding to the linescan 2 in (b)). The result shows that the localized plasmonic mode at the apex is symmetric with respect to the taper axis. As the energy increases, the field of the mode penetrates less into the vacuum because of the smaller decay depth at smaller wavelengths. The broadband feature up to 2.0 eV indicates the capturing of the broad local density of optical states. Above 2.0 eV, the local signal at the apex is drastically reduced due to the large imaginary part of the dielectric function which is induced by the interband excitation of d-band electrons.[92]

EFTEM images help to visualize the spatial distribution of the near-field of the taper surface plasmonic modes projected along the electron trajectory (Figure 3–2 (f)). With decreasing energy loss, the extent of the mapped near-field tends to increase in the vicinity of the taper apex. However, it is attributed to (i) the increasing decay length of the plasmon near-field, and (ii) the convolution of the delocalization of inelastic electron scattering due to the long-range Coulombic interaction.[7, 92, 100] EFTEM imaging is in principle showing the similar results as EELS measurements, however, with the emphasis on direct optical imaging.

The above observed characters of the plasmonic modes hold true in the gold taper system generally. However, the formation mechanism for these discrete resonances is ambiguous. In Section 3.3, this question will be further addressed and disentangled.

In addition, such tapered metallic tips are commonly applied in apertureless scanning near-field optical microscopy. However, the characteristics of such tips vary on their shapes. To improve the reproducibility of taper characteristics, attaching a single well-defined nanoscopic scatterer at the apex is proposed because of the correspondingly well-controlled field enhancement effects.[101-103] Therefore, the surface plasmonic modes of a taper with a particle-like apex were also probed by EELS and EFTEM (Figure 3–3). Compared to the smoothly tapered geometry in Figure 3–2, the particle-like apex shape narrows the spectral range of the localized mode down below ~ 1.5 eV (Figure 3–3 (c–d)). Moreover, the strong intensity of this mode indicates a strong coupling to the external field of the fast electrons. The gradual blue-shifts of the discrete modes along the shaft reach plateaus at higher energies when approaching the apex (Figure 3–3 (b)).
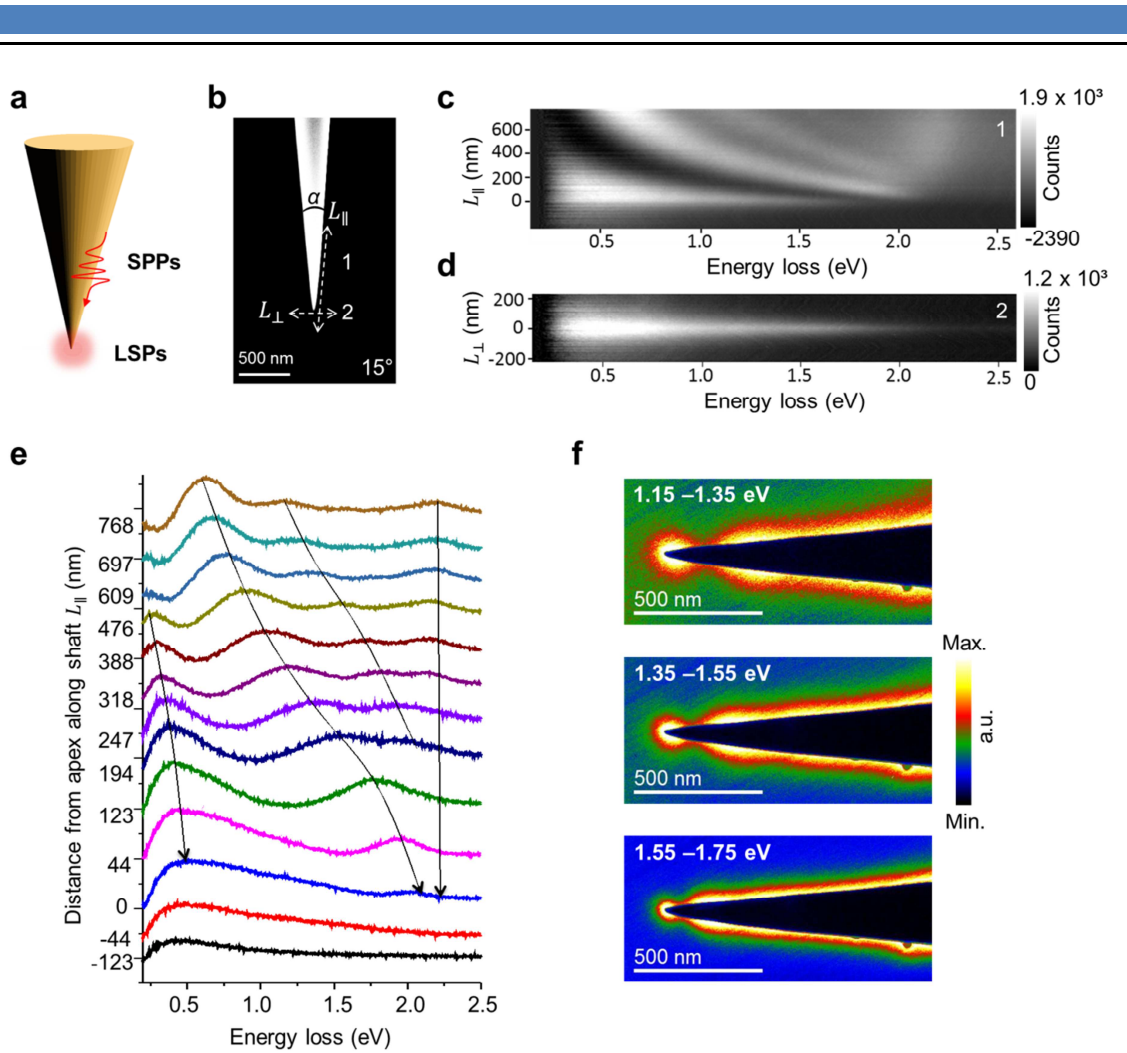
Figure 3–2. Plasmonic modes in three-dimensional gold tapers with smooth apices. (a) Sketch of SPPs on the taper shaft and LSPs at the taper apex. (b) HAADF image of a gold taper with an opening angle α of 15°. EELS linescans were performed along the shaft (dashed line 1) and perpendicular to the taper axis in front of the apex (dashed line 2). (c) and (d) are the corresponding distance–EEL maps of linescans 1 and 2 in (b) as a function of distance from the apex. $L_{\parallel}$ and $L_{\perp}$ respectively denote the distances from the taper apex along the shaft or vertical to the taper axis. (e) EEL spectra extracted at different distances from the apex along the shaft $L_{\parallel}$. The intensity has arbitrary units. The tendencies of the observed resonant peaks are highlighted by black lines. (f) Corresponding EFTEM images at the energy losses of 1.25, 1.45 and 1.65 eV with an energy window of 0.2 eV. The colour bar on the right symbolizes the energy-loss probability which is a measure of the overlap between the monochromatic electron wavefunction and the local electric near field in the vicinity of the taper apex.[92]
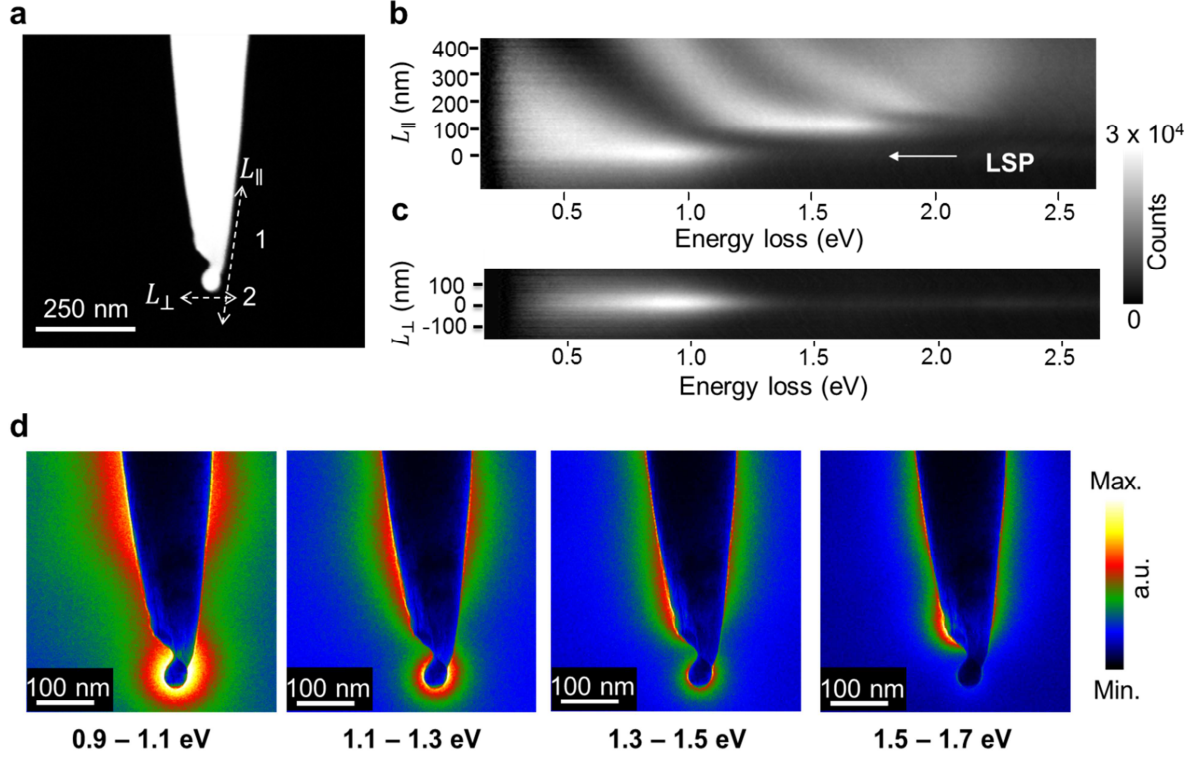
Figure 3–3. Plasmonic modes in a gold taper with a particle-like apex. (a) STEM-HAADF imaging. EELS linescans were performed along the shaft (dashed line 1) and perpendicular to the taper axis in front of the apex (dashed line 2). (b) and (c) are the corresponding distance–EEL maps of linescans 1 and 2 in (a) as a function of distance from the apex. $L_\parallel$ and $L_\perp$ respectively denote the distances from the taper apex along the shaft and vertical to the taper axis. The white arrow points to the localized surface plasmon at the apex. (d) Corresponding EFTEM images at the energy losses from 0.9 to 1.7 eV with an energy window of 0.2 eV. The colour bar on the right symbolizes the energy-loss probability which is a measure of the overlap between the monochromatic electron wavefunction and the local electric near field in the vicinity of the taper apex.

3.3 Coexisting resonance mechanisms: reflection and phase matching

The experimental and theoretical results indicate that the opening angle of three-dimensional gold tapers plays a key role in tailoring the properties of excited surface plasmons sustained by this structure.[41, 93, 97, 98] To analyze the effect of the opening angle on EEL spectra and to unravel the interplay between reflection and phase matching resonances, we performed numerical FDTD calculations on two tapers with extremely small and large full opening angles (5° and 30°). In the following, I use the notations *"N"* and *"M"* for ordering the multiple resonances dominated by reflection and phase matching, respectively.

For this, we first simulate the electric fields generated by a swift, relativistic electron, moving perpendicular to the taper axis. The electron, with a kinetic energy of 200 keV and moving at $V = 0.67c$ (c: speed of light in vacuum), is modelled as a Gaussian wavepacket with a transverse width of 8 nm and a time duration of less than 100 as.[104] For each taper, the component of the scattered electric field projected along the electron trajectory, $|E_x|$, at a distance $L = 1460$ nm from the apex is plotted on a logarithmic scale as a function of the electron trajectory and time. This field component is chosen because it is the only component that contributes to the EELS signal. The large travelling distance of

1460 nm is intentionally set to separate signals of the reflected wave and the phase-matched wave along the time axis.

I first analyze the results for a 5° taper (Figure 3–4 (a)). Three different contributions to the re-emitted fields can be distinguished. First, the excitation of plasmon oscillations gives rise to the emission of propagating electromagnetic fields. These propagate away from the taper axis at the speed of light c to the free space and retardation results in field maxima that are inclined with respect to the time axis at an angle indicated by the dashed yellow line. In the time domain, the excitation of different radiative, higher-order angular momentum SPP modes of the taper gives rise to a complex interference pattern dying out within a few fs after the arrival of the electron beam. In addition, also bound, evanescent SPP modes of the taper are excited by the electron beam. For a 5° taper, only the lowest-order mode, $M = 0$, is a bound mode and can propagate away from the excitation spot towards the apex. Due to this propagation, the contribution of the bound mode to the re-emitted field lasts only a few fs. Importantly, the $M = 0$ mode remains a bound mode even for vanishingly small local taper radii and hence will generate a spatially highly confined electromagnetic field near the apex.[82, 83, 89] For finite taper radii, the incident mode is partially reflected.[93, 105] This reflection is clearly seen as a pronounced, time-delayed evanescent field burst arriving at Δt ~11 fs. Since only the radial (E_r) and on-axis (E_z) electric field components of the $M = 0$ mode are nonzero,[90] the projection along the electron trajectory (x-axis) imposes a null intensity at the nearest distance of the electron to the taper. The time delay of the reflected SPP field provides a measure of the path-integrated local effective refractive index n_{eff} of the $M = 0$ mode, $\Delta t = 2 \int_{z_e}^{z_a} \frac{n_{eff}(z)}{c} dz$, between the impact point of the electron at z_e and the apex at z_a. From this, we estimate an average effective refractive index of $n_{eff} \approx 1.15$, reasonably close to what is expected based on the tabulated values of bulk gold.[70] Possible time delays[106] due to the local increase in n_{eff} near the apex[83] seem too small to be reliably extracted. Instead, a pronounced chirp of the reflected SPP wavepacket is visible in the FDTD simulation as a clear decrease in time delay between successive oscillations of the reflected evanescent plasmon field. In the spectral domain (Figure 3–4 (c)), the time-delay of SPP oscillations gives rise to pronounced oscillations in the EEL spectra,[93, 98] with a fringe spacing that is decreasing with increasing energy loss. The energy loss dependence of the EELS fringes hence provides a quantitative measure of the chirp of the bound $M = 0$ SPP wavepacket upon its propagation from the injection point to the apex and back.

A fundamentally different time structure of the re-emitted field is observed for the excitation of the taper with a large opening angle of 30° (Figure 3–4 (b)). Here, again, radiative higher-order angular momentum modes of the taper are impulsively excited. Their re-emitted fields give rise to a strong burst of light that propagates away from the taper surface at the speed of light in vacuum (dashed yellow line). For this taper not only the $M = 0$ mode but also the $M = 1$ and $M = 2$ modes are bound, evanescent SPP modes. Their excitation launches a coherent SPP wavepacket that propagates towards the apex. The characteristic of this wavepacket is the different inclination angle (dashed black line), defined by the velocity V of the electron. The large radius of this taper leads to a longer interaction length along the electron trajectory and, hence, a finite propagation distance of the SPP wavepacket during the interaction. The SPP propagation along the taper surface then results in the observed decrease of this component within the first few femtoseconds. Both, the $M = 1$ and $M = 2$ modes are coupled into the far field at finite distances from the apex. The $M = 0$ mode again propagates to the very apex of the taper, where it is partially converted into far-field radiation and partially back-reflected. For an opening angle of 30°, the amplitude of the back-reflected field, however, is fairly weak. Hence, the modulation contrast in the EEL spectra (Figure 3–4 (d)), which is much smaller than for a 5° taper (Figure 3–4 (c)), arises from the action of the higher-order angular momentum modes, $M > 0$, which are all coupled into far-field radiation before reaching the apex region. Therefore, phase

matching is clearly the dominant contribution to the modulation contrast for such tapers with large opening angles.
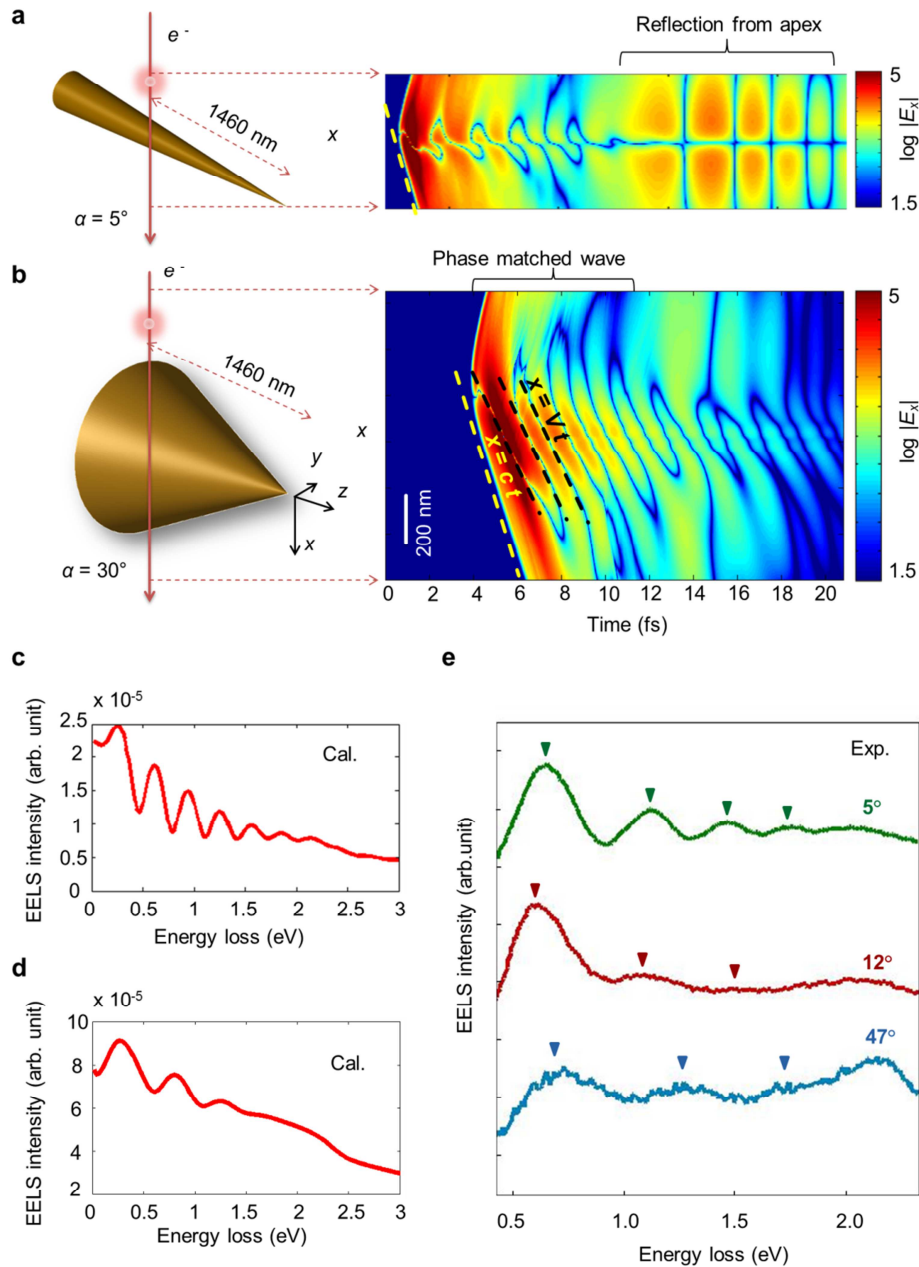
Figure 3–4. Different mechanisms contributing to the EEL resonances: phase-matching versus reflection. FDTD simulations of the total scattered electric field along the electron trajectory $|E_x|$, plotted on a logarithmic scale versus electron trajectory (nm) and time (fs) when a relativistic electron is passing at a constant distance of $L = 1460$ nm for gold tapers with full opening angles α of (a) 5° and (b) 30°, respectively. L, the distance between the taper apex and the electron impact location along the taper surface, is sufficiently large to separate phase-matched and reflected waves along the time axis. The slope of the dashed black line denotes the velocity of the exciting electron, which is roughly 2/3 of the speed of light in vacuum (shown as a dashed yellow line in (a) and (b)). (c) Calculated EEL spectrum from (a) which is dictated by the reflection mechanism. (d) Calculated EEL spectrum from (b) which is dominated by the phase-matching mechanism. (e) Experimental zero-loss-corrected EEL spectra at an equivalent distance from the apex of $L = 800$ nm for gold tapers with an opening angle of 47°, 12° and 5° in the energy-loss range from 0.5 to 2 eV. The zero-loss peak contribution was subtracted from the individual spectra by using a power-law fit. The maxima of the spectra are normalized and vertically shifted for comparison.

To verify these theoretical findings, I now compare experimental EEL spectra of gold tapers with various full opening angles from 5° to 47° at equivalent distances of $L = 800$ nm from their apex (Figure 3–4 (e)). The full opening angles for the investigated gold tapers are $5° \pm 1°$, $12° \pm 2°$, $19° \pm 1°$ and $47° \pm 4°$. Obviously, there are a larger number of resonances for the gold taper with 5° opening angle with a fringe spacing and modulation depth that approximately matches that in the simulations (green curve). Evidently, these fringes are reflection-dominated, as concluded in ref. [98]. The modulation depth is much more pronounced than that of the resonances observed for the gold taper with 47° opening angle (blue curve), which is evidently dominated by phase matching. Interestingly, the EELS resonances of the gold taper with 12° opening angle (red curve) show a much reduced fringe contrast compared to those of the two gold tapers with 5° and 47° opening angles. This is a surprising and unexpected result which cannot easily be understood by considering only either the phase matching or the reflection-type contribution to the EELS fringes. Instead, we conclude that for the 12° taper both phase matching and reflection are active. Their overlap leads to a smearing of the EELS signal, because both resonances appear within the same energy range.

In addition to showing an individual EEL spectrum at a fixed location L, we also compute and measure EEL spectra as a function of distance (distance–energy EELS maps) to analyze the spectral features in more detail. This allows us to directly compare the simulated and experimental distance–energy EELS maps. As shown in Figure 3–5, there is good agreement between the experimental and the computed EELS maps of gold tapers with different opening angles. Slight differences are attributed to a non-perfect apex shape, surface roughness or a non-constant opening angle. For all the tapers, an extremely broadband resonance near the apex, extending from 0.5 eV, a lower limit set by the finite energetic width of the zero-loss peak, to 2.0 eV, and an upper limit set by the onset of interband absorption of gold was found. This broad resonance shows that the taper can act as a broadband waveguide which can localize surface plasmon polariton fields, i.e., the $M = 0$ mode, at its very apex. In fact, the broadband signal at the apex reflects the capturing of the full local density of states by the taper, and also the perfect quality of our tapers. It also shows that such tapers, when excited at the apex, can capture the electron-induced radiation with high collection efficiency, as investigated elsewhere.[92] Discrete resonances along the shaft are observed in both experimental and the computed EELS maps. When decreasing the opening angle, more resonances in each sequence are observed within a certain distance from the apex. Furthermore, the reflection-dominated EELS map displays a more distinct contrast among the multiple resonances (Figure 3–5 (c)) than the phase-matching-dominated one in Figure 3–5 (a). Indeed, by further decreasing the opening angle the taper asymptotically evolves into a fiber with a small radius, for which only the reflection from the ends will be responsible for the observed resonances in the EELS signal. For example, a semi-infinite whisker with a small radius can be ideally the reference for a pure reflection mechanism. For comparison, the EEL spectra of a gold whisker[73] with 50 nm diameter are measured along its long axis (Figure 3–6 (a)). For this whisker, only the fundamental $M = 0$ mode is supposed to be sustained by this structure according to previous theoretical calculations.[97] Note that phase matching can also become relevant for whiskers at sufficiently large radius. The EEL spectra of the whisker show at least 4 distinct resonances that are observed inside the 1μm scanning distance from the whisker end, which is highly similar to the distance–energy EELS map of the gold taper with a full opening angle of 5° (Figure 3–5 (c)).

In essence, the experimental distance–energy EELS maps (Figure 3–5) show a gradual transition from reflection to phase-matching with increasing opening angle. To further support this observation, Figure 3–6 (b) compares the total scattered electric field $\log |E_x|$ (superposition of all the excited plasmons) of a half-infinite gold whisker with 50 nm diameter (as reference for reflection) with the gold tapers with opening angles of 10°, 20° and 50° at a constant distance of $L = 1460$ nm. As the opening angle of gold tapers increases to 10° and 20°, the contribution of the phase-matched waves

becomes apparent. When reaching 50° almost only the phase-matched waves are visible in the corresponding $\log |E_x|$ plot.
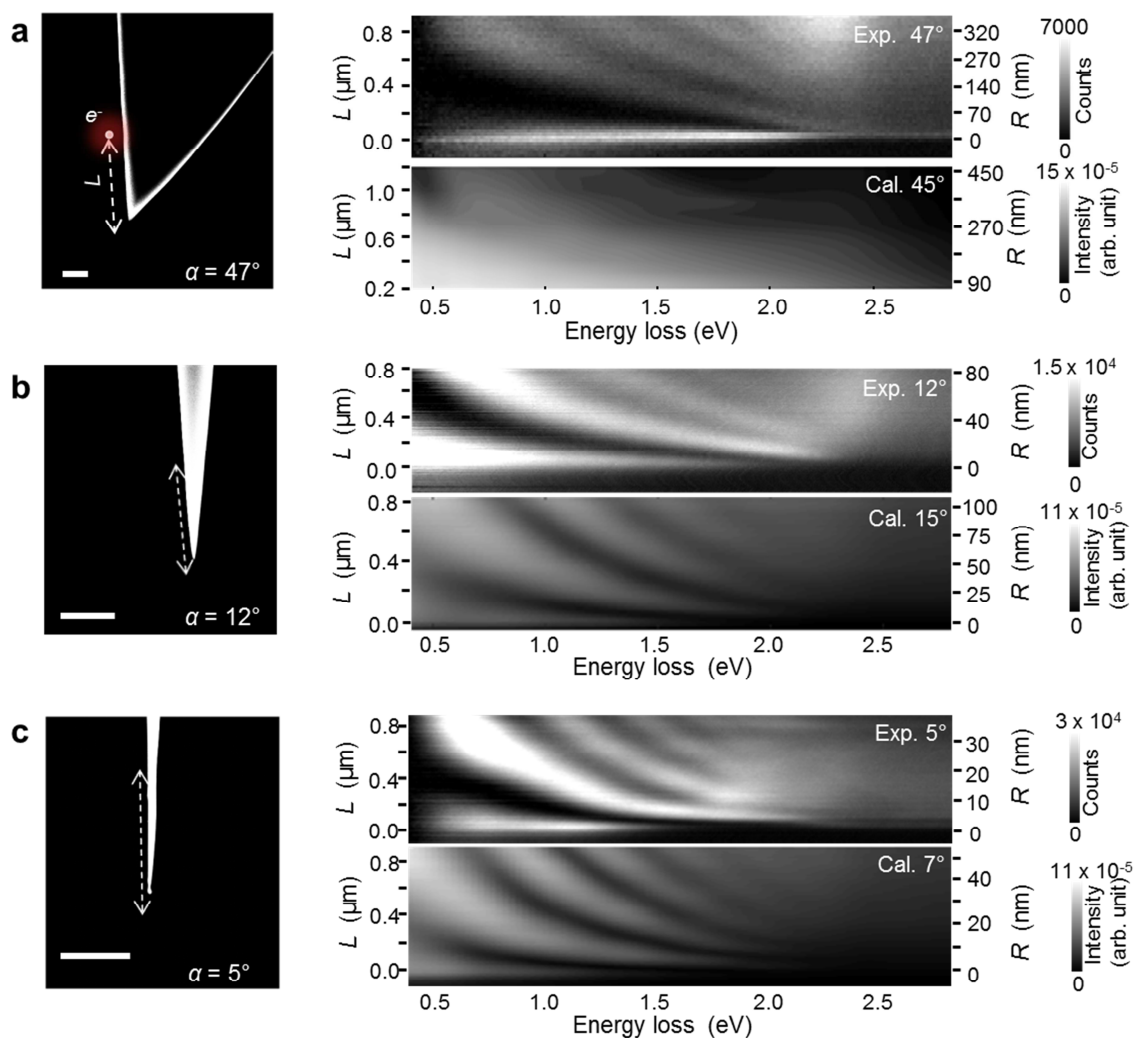
Figure 3–5. Dark-field imaging and spectroscopy of gold tapers with full opening angles of (a) 47°, (b) 12° and (c) 5°, respectively. The position $L = 0$ μm corresponds to the taper apex and the scanning direction is upward. Both experimental and computed electron energy-loss spectra are plotted as a function of impact location along the taper shaft (L, left) and the corresponding local radius (R, right). In the experimental EEL spectra the contribution of the elastic zero-loss peak was subtracted by a power-law fit. Scale bar lengths are 500 nm.
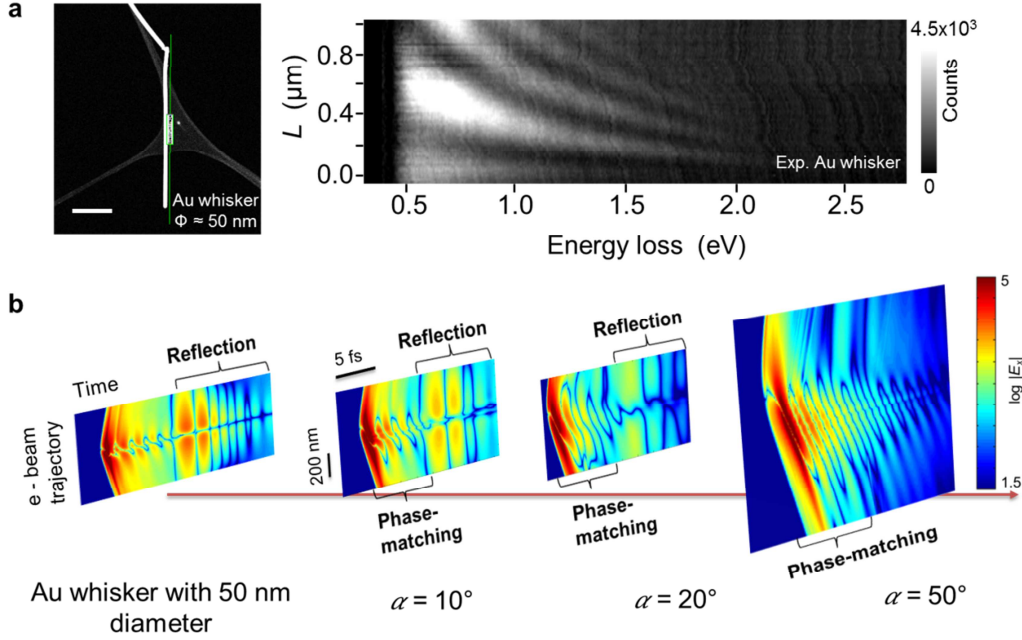
Figure 3–6. (a) STEM annular dark-field image and zero-loss-corrected distance–energy EELS map of a gold whisker with a diameter of ~50 nm. The location $L = 0$ μm corresponds to the lower end of the whisker and the scanning direction is towards the top. The scale bar length is 200 nm. (b) Transition from reflection to phase matching: numerically calculated total scattered electric field along the electron trajectory, $\log |E_x|$, versus electron trajectory (nm) and time (fs) for a gold whisker and tapers with different opening angles of 10°, 20° and 50° when a relativistic electron is traversing the taper surface at a constant distance of $L = 1460$ nm from the apex. The scheme resembles Figure 3–4 (a–b).

Although the energy dispersion of the reflection-dominated and the phase-matching-dominated EELS resonances appear to look very similar, the physics for forming this energy dispersion is intrinsically different. I therefore apply curve fitting using hyperbolic functions to the experimental EELS resonances of the half-infinite gold whisker with 50 nm diameter as a reference of pure reflection (Figure 3–6 (a)) and for the gold taper with 47° opening angle as a representative of phase matching (Figure 3–5 (a)).

First, in the case of the 50-nm gold whisker, at an arbitrary energy, the forward propagating $M = 0$ mode travels along the gold whisker length with a spatially independent propagation constant β and experiences a phase shift $\Delta\varphi$ upon reflection at the end. For the Nth order resonance the phase accumulation equals N times of 2π

$$2\beta L + \Delta\varphi = 2N\pi,$$

$$2\beta\left(L + \frac{\Delta\varphi}{2\beta}\right) = 2N\pi. \tag{3.1}$$

In equation (1), the part $\frac{\Delta\varphi}{2\beta}$ can be substituted by L_0. With $\beta = \frac{\omega}{c} \cdot n_{\text{eff}}$, where c is the speed of light in vacuum and n_{eff} is the effective refractive index, equation (3.1) can be rearranged to

$$\frac{\omega}{c} \cdot n_{\text{eff}}(L + L_0) = N\pi. \tag{3.2}$$

Multiplying by $\hbar$ on both sides of equation (3.2) and replacing $\hbar\omega$ with E, we obtain

$$E = \frac{N\hbar\pi c}{n_{\text{eff}}(L + L_0)} \qquad (3.3)$$

, where $L_0 = \frac{\Delta\varphi}{2\beta}$.

Comparing equation (3.3) with the hyperbolic fitting function $E = \kappa_L/(L + L_0)$, we find

$$\kappa_L = \frac{N\hbar\pi c}{n_{eff}}. \qquad (3.4)$$

Note that the derived components $L_0 = \frac{\Delta\varphi}{2\beta}$ and $\kappa_L = \frac{N\hbar\pi c}{n_{eff}}$ represent the average values over the energy range, where the hyperbolic fitting function $E = \kappa_L/(L + L_0)$ is applied. Therefore, the reflection-induced resonances have energy dispersions proportional to the inverse distance between the impact location and the end of the whisker with a virtual length increase $E = \kappa_L/(L + L_0)$ as shown in Figure 3–7 (a), where L_0 is almost a constant of (0.202 ± 0.024) μm for all the resonances $N = 1, 2, 3$ and 4. The other fitting parameter κ_L depends on the sequence number N in a linear fashion as $\kappa_L = (0.379 \cdot N + 0.1553)$ $\mu m \cdot eV$. Figure 3–7 (c) illustrates that the observed EELS resonances of the gold whisker can be understood as a reflection-type resonance.[107] Therefore, the fitting parameter L_0 is interpreted in terms of a length increase as shown in Figure 3–7 (c), which is linked to a phase shift $\Delta\varphi$ at the whisker end in the energy range between 0.5 and 2.0 eV, where the hyperbolic fitting function is applied.
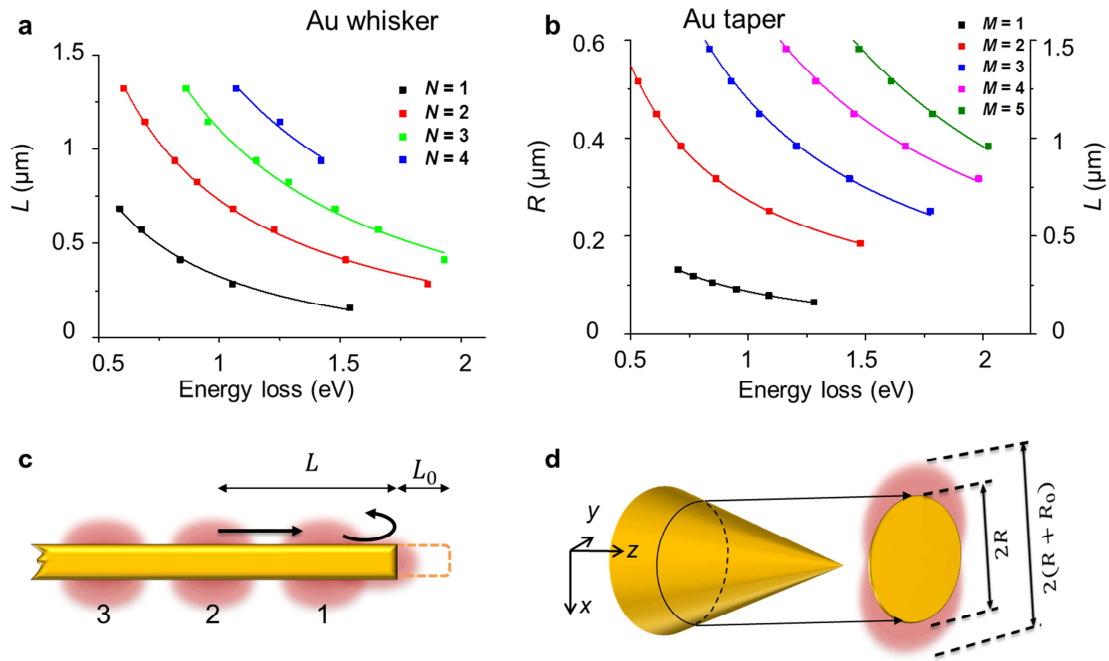
Figure 3–7. (a) Relations of maxima in EEL spectra versus the distance from the end of the gold whisker with 50 nm diameter (dots). Curves are fits to a hyperbolic function $E = \kappa_L/(L + L_0)$, where κ_L and L_0 are constants. (b) Dispersions of maxima in EEL spectra versus the distance from the apex of the gold taper with 47° opening angle (dots). Curves are fits to a hyperbolic function $E = \kappa_R/(R + R_0)$, where κ_R and R_0 are constants. (c) Reflection-type (standing wave anti-node) mechanism for the SPP resonances on the gold whisker. The physical meaning of the fitting parameter L_0 is related to the phase shift at the end of the gold whisker. (d) Phase-matching principle for large-opening-angle tapers along the electron trajectory. The physical meaning of the fitting parameter R_0 is relevant to the effective interaction length along the electron trajectory.

Additionally, the effective refractive index n_{eff} can be extracted from the fitting parameter κ_L based on the experimental EELS data according to equation (3.4). I plot the extracted n_{eff} *versus* the standing wave SPP antinode order N in Figure 3–8. Note that in this case, the extracted n_{eff} is an average value over the energy range from 0.5 to 2.0 eV. The experimentally extracted n_{eff} of each resonance order N (black dots with error bars) fall in the similar range of the theoretically calculated values (marked as red area). This good agreement demonstrates the reasonable accuracy of the method of the hyperbolic function fitting. The small deviation may come from the slight morphological difference between the fiber and the whisker, where the gold whisker may have facets.
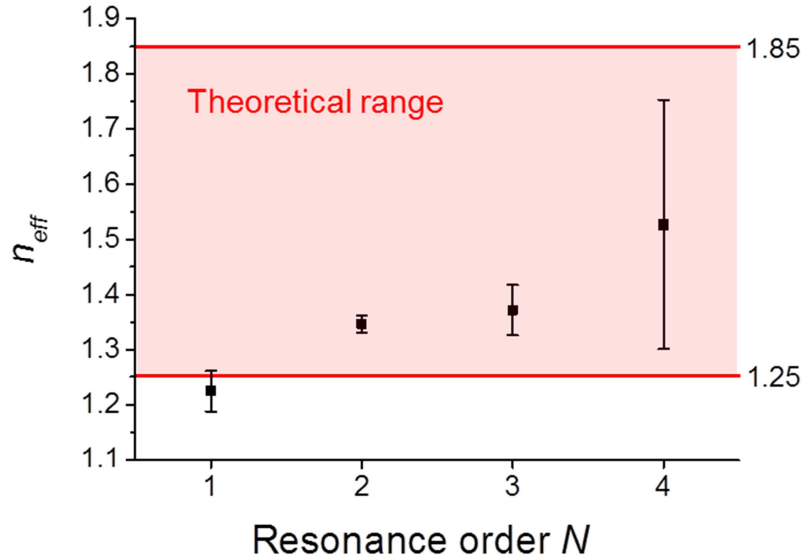
Figure 3–8. Comparison between the experimentally extracted effective refractive index n_{eff} of the gold whisker and the theoretically calculated range of a gold fiber in the energy range from 0.5 to 2.0 eV. Both the gold whisker and the gold fiber have the same diameter of 50 nm. The extracted n_{eff} of the gold whisker is an average value over 0.5 to 2.0 eV (dots with error bars), whereas the theoretically calculated n_{eff} of the gold fiber gives a value range between 1.25 and 1.85 (red area).

On the other hand, the dispersion of the EELS resonances of the gold taper with 47° opening angle can be well captured by a hyperbolic function of the form $E = \kappa/(L + L_0)$ (Figure 3–7 (b)). With $L = R/\sin(\alpha/2)$ being the distance from the apex and R and α being the local radius and the full opening angle, respectively, the fitting function can be transformed into $E = \kappa_R/(R + R_0)$. Contrary to the gold whisker, the fitting parameters κ_R and R_0 for the taper with 47° opening angle have different meaning, since the phase-matching principle is dominant in this system. Figure 3–7 (d) illustrates that the fitting parameter R_0 can be viewed as an extension of the geometric interaction length between the SPP field and the fast electron along the trajectory beyond $2R$. The interaction length extension R_0 can be due to the fact that the interaction already starts once the fast electron enters the near-field of the taper structure.[97] In addition, R_0 also includes the phase lag between the SPP and the fast electron. κ_R is therefore associated with the phase matching, linearly depending on the azimuthal mode order $\kappa_R = (A \cdot M + B)\ \mu\text{m·eV}$, with the linear fitting parameters $A = 0.254$ and $B = 0.201$. Considering this, the swift electron picks up a phase of $\omega \cdot (2R + 2R_0)/V$ by moving through the near-field region of the taper, whereas the excited plasmons with an azimuthal order M pick up a phase of $M\Delta\varphi$. In the phase-matching picture, a resonance is observed in the distance–energy map whenever these two phases are equivalent at the energy of $E = M\Delta\varphi\hbar V/(2R + 2R_0)$, where $E = \hbar\omega$ is the energy loss due to the excited plasmon, and $\Delta\varphi$ is the angular rotation of the plasmon along the circumference. This simple model matches perfectly with the hyperbolic relation stated above. The value of $\Delta\varphi$ can

be thus deduced as a function of the angular momentum order $\Delta\varphi = (0.363 \cdot M + 1.308)$ radian. Moreover, the significance of this model is its ability to unravel the parameters $\Delta\varphi$ and R_0, by comparison to the experimental result. Especially the parameter R_0 demonstrates the actual increase in the EELS cross section compared to the real size of the structure. Therefore, it seems to be worthy to define an electron-induced cross section, in analogy to the so-called scattering, extinction, and absorption cross sections in far-field optical experiments.
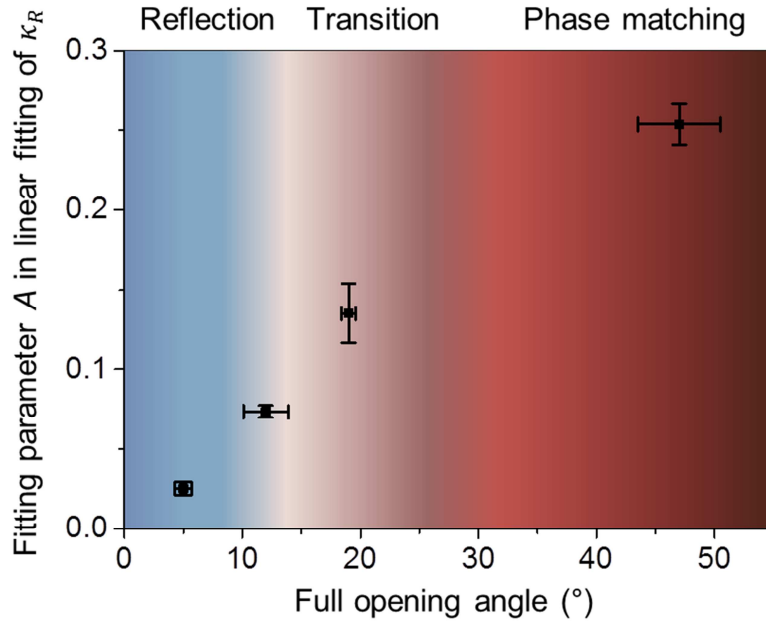
Figure 3–9. Differentiation of experimental EEL resonances of gold tapers with full opening angles of 5°, 12°, 19° and 47° by empirical hyperbolic fitting $E = \kappa_{R,L}/(R(L) + R_0(L_0))$. The fit parameter $\kappa_{R,L}$ for each taper linearly depends on its resonance order as $\kappa_R = (A \cdot M + B)$ or $\kappa_L = (A \cdot N + B)$. The linear fitting parameter A (slope of $\kappa_{R,L}$) exhibits a monotonic increase as a function of the full opening angle. The uncertainties of the measured opening angles and of the fit parameters are attached horizontally and vertically to each data point.

In addition to quantitatively describing the EELS resonances, the hyperbolic fitting function $E = \kappa_{R,L}/(R(L) + R_0(L_0))$ introduced here can help us to distinguish between the phase matching and reflection mechanisms. To better demonstrate it, I plot the values of the slope of $\kappa_{R,L}$ (as it is linearly dependent on the EELS resonance order) for the gold tapers with full opening angles of 5°, 12°, 19° and 47°, as shown in Figure 3–9. The slope of the fit parameter $\kappa_{R,L}$ increases monotonically with opening angle. In other words, the value of the phase-matching-induced EELS resonance is almost 10 times larger than that of the reflection-induced EELS resonances. For intermediate opening angles (transition between reflection and phase matching), the linear fitting parameter A also exhibits intermediate values. Another way to distinguish phase matching from reflection would be to vary the kinetic energy of the incoming electrons, which only affects phase matching.

In summary, I have clarified the link between the phase matching and the reflection mechanisms contributing to EELS resonances in electron-induced surface plasmons of three-dimensional gold tapers. This was achieved by studying a large range of opening angles both experimentally and by simulation. Phase matching and reflection coexist in the system of gold tapers and can both contribute to the EELS signal. EELS signals due to phase matching and reflection show close similarity. However, the contribution of either reflection or phase matching varies with both the local radius of

the gold taper at the impact location and the distance to the taper apex along the shaft. In the proximity of the apex (< 2–3 μm) the opening angle of the taper can be considered as a crucial parameter. At small opening angles, the reflection of surface plasmon polaritons from the taper apex is dominant, since small radii limit the excitation of higher-order azimuthal plasmons. Moreover, long-range propagation of the plasmons along the taper apex is better supported by such tapers. In contrast, phase matching manifests itself in maxima of the interference pattern recorded in the energy–distance EELS map at larger opening angles, mostly because of the longer interaction length between the electron and the taper along the electron trajectory. In between, a gradual transition from the reflection-based mechanism towards the phase-matching principle is observed by increasing the opening angle.

Additionally, the energy loss due to the reflection-induced EELS resonances is proportional to the inverse distance between the impact location and the reflection end with a virtual length increase, where the virtual length increase represents the phase shift at the reflecting end. On the other hand, the energy dispersion of phase-matching-induced EELS resonances is proportional to the inverse local radius with an extension of interaction length along the electron trajectory. This stems from the fact that the initial interaction starts, when the electron enters the near-field of the taper.

3.4   Far-field radiation of gold tapers

There are several mechanisms for light emission of gold tapers irradiated by fast electrons. They are coherent transition radiation, radiative decay of surface plasmons and recombination of hot carriers.

Coherent transition radiation is a wide-band radiation whenever a fast electron crosses the interface between different dielectric media.[5, 57, 108] In order to adjust to the change of dielectric properties and further reach the equilibrium with the new environment, the fast electron modifies its electromagnetic field by shaking a portion off as radiation.[49] An alternative view to explain transition radiation is within a picture of image charges. The negatively charged fast electron mirrors a positive image charge in the opposite medium below the interface, which forms an effective dipole normal to the interface. The effective dipole vanishes and radiates when the electron passes through the interface. The character of the resulting transition radiation pattern is similar to that produced by a dipole normal to the interface (Figure 3–10 (a)).[49, 57, 109] A more general description is that the fast electron induces local charge and current polarizations near its trajectory while approaching the second medium. These polarizations create an induced field which can radiate to the far-field as transition radiation. Note that transition radiation happens merely at surfaces and is independent on the specimen thickness.[110]

The **radiative decay of surface plasmons** is another luminescence mechanism in plasmonic gold tapers. This kind of radiation belongs to coherent radiations because it ´remembers´ how the surface plasmon modes were excited with respect to the incoming electron in terms of phase relation. In our gold tapers, plasmonic modes with different azimuthal orders $M \geq 0$ can be sustained as reported in Section 3.2 and 3.3. They have different radiation manners (Figure 3–10 (b)). The fundamental mode $M = 0$ can propagate evanescently along the taper axis unless it reaches the geometry singularity at the apex. This causes partial radiation and partial reflection. The radiation pattern of the $M = 0$ mode at the apex is similar to that of a dipole along the taper axis. For higher-order modes $M > 0$ excited at larger radii, the modes can rotate azimuthally and propagate longitudinally along the shaft above critical radii.[41] They mainly radiate in the azimuthal directions, e.g. the xy plane. Therefore, the luminescence contributed by surface plasmons are mainly along $+ x$, $- x$, $+ y$ and $- y$ directions. Normally this radiation mechanism is predominant in plasmonic structures.

According to the electronic band structure of gold, hot carriers (electron–hole pairs) can be created through the 5d–6sp **interband transitions** above 1.94 eV[111] and the 6sp **intraband transitions** below 1.94 eV.[112, 113] They can recombine either radiatively or non-radiatively. This type of radiation is incoherent, since it does not have any memory of the incoming electron in terms of phase relation. Moreover, it is usually not considered as dominant in metals because of strong electron–electron interactions and electron–phonon scattering.[114]
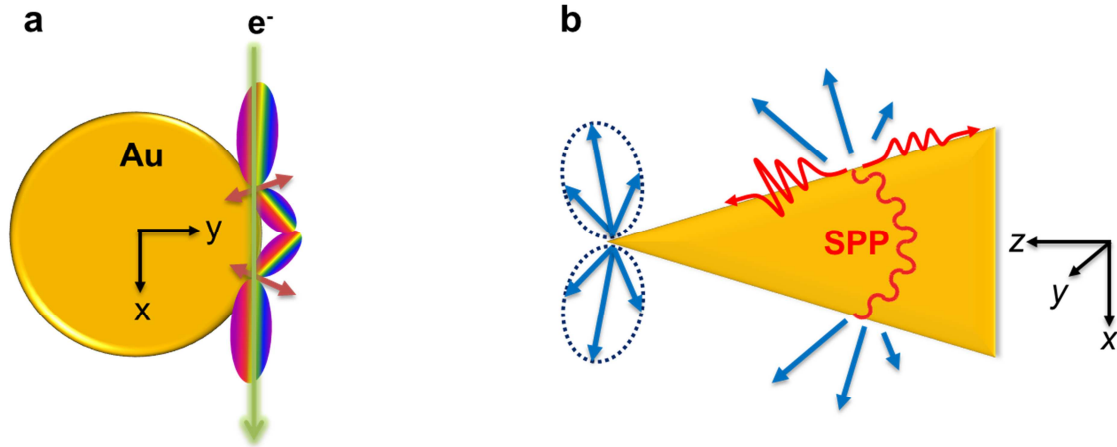
Figure 3–10. Schematic illustration of (a) transition radiation and (b) surface-plasmon radiative decay in gold tapers. In (a), a fast electron (green line) passes through the taper near its shaft viewing along the z-axis. Red arrows represent effective dipoles and the connected colorful lobes for the broadband transition radiation. In (b), red curves indicate the propagation of SPPs in forward, backward and also azimuthal directions. Blue lines depict the light emission due to the radiative decay of SPPs.

Figure 3–11 (c) shows the experimental CL spectra of a 13° gold taper along its shaft as a function of distance from the apex. Note the spectra include also the taper part around 70 nm from its surface. All the radiations from the entire structure were simultaneously collected during the acquisition (Figure 3–11 (a)). I see a weak signal localized at the apex spanning from 700 to 1000 nm. Away from the apex, a strong emission in the wavelength range 500–700 nm rises up. This radiation is red-shifted as the excitation distance increases from 300 to 800 nm approximately, and then gets attenuated at the larger distances. It is hard to distinguish different radiation sources directly from the recorded spectra, since they show no significant difference in spectral responses.

To understand the experimental observations, corresponding numerical simulations were set up with the scenario that the fast electron just passed across the surface of the taper along its shaft (Figure 3–11 (b)). The total scattered electromagnetic fields were calculated by solving the full Maxwell´s equations embedded with the experimentally measured dielectric functions of gold.[70] Later, the Poynting vectors at the six orthogonal planes normal to $\pm x$, $\pm y$ and $\pm z$ axes were computed, respectively. The energy falling on the planes normal to $\pm x$, $\pm y$ and $+ z$ axes represent the electron-induced radiation, whereas the energy captured by the plane normal to $- z$ direction denotes the guided energy propagating away from the apex.
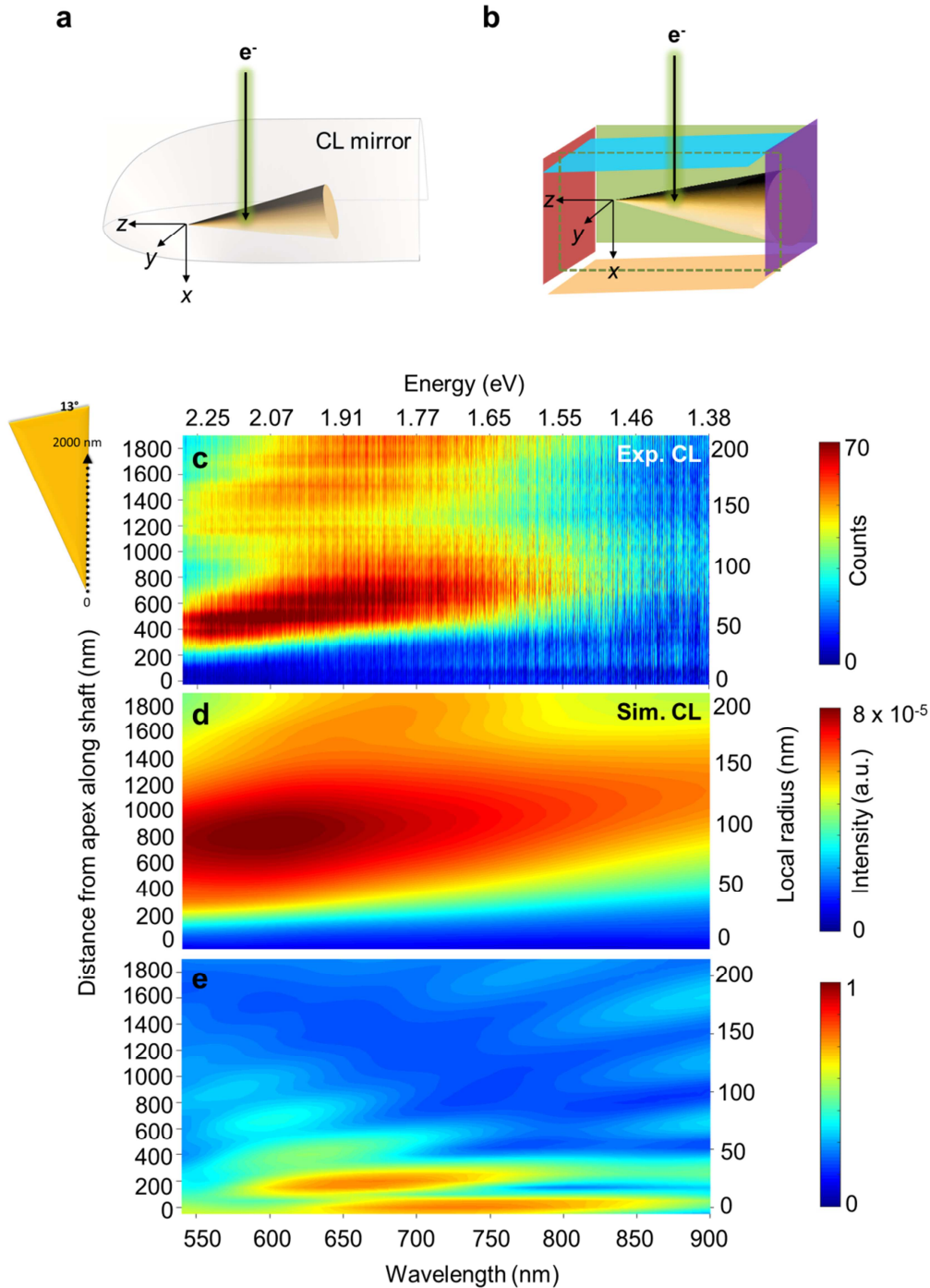
Figure 3–11. (a) Sketch for emission collection in CL experiments. (b) Illustration of decomposing CL signals to orthogonal planes in simulations. Plane units are color codes. Dashed green rectangle denotes a transparent green plane for interior viewing. (c) Experimental and (d) simulated CL spectra of a taper with 13° opening angle as a function of distance from the apex along its shaft (left) and the local radius (right). The inset on the left indicates the scanning direction of the electron beam with respect to the taper. (e) Ratio of the energy guided in − z direction to the total energy collected in the entire orthogonal directions.

To mimic the experimental CL spectra collected by the CL mirror, we integrate the electron-induced radiation arriving at the red, blue, and two green planes in the $x \leq 0$ domain (Figure 3–11 (b)). Figure 3–11 (d) shows in general a good match between the experimental and simulated CL spectra. This implies that scattering and interference, which are modeled well by Maxwell´s equation, should be the

basic phenomena for the gold taper cathodoluminescence. I also notice that the strong radiation in the wavelength range 500 – 700 nm is present, however, around 800 nm away from the apex. This distance discrepancy could be caused by the direction-dependent reflectance of the CL mirror, which is not the case in simulations. Based on the previous knowledge, the weak radiation at the apex could be attributed to the high guidance of the evanescent $M = 0$ mode, which is exclusively excited for small cylindrical radii below 50 nm.[97] This inference is further verified by calculating the ratio of the energy at the purple plane to that at all the six orthogonal planes (Figure 3–11 (e)). It shows that the induced energy, as high as 75%, is guided in the $-z$ direction when the electron excites at the local radii below 50 nm. Meanwhile, two resonances imply the $M = 0$ mode at the apex and the $N = 1$ mode behind the apex (first order reflection of the $M = 0$ mode).
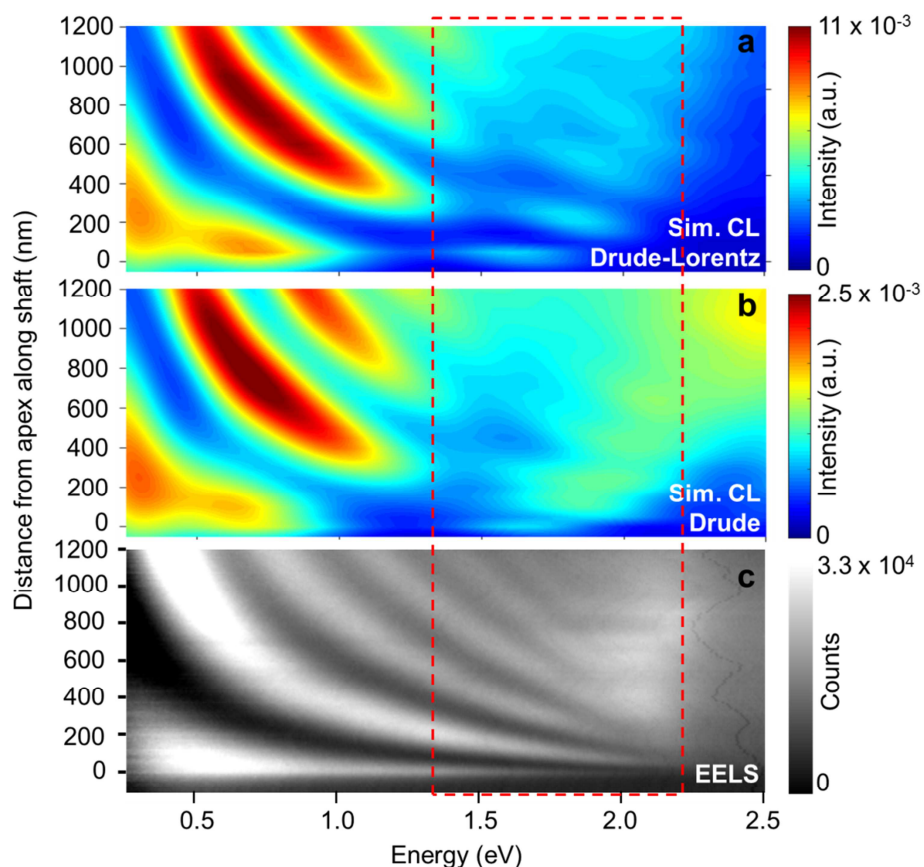
Figure 3–12. Simulated CL spectra (a–b) and experimental EEL spectra (c) of the taper with 13° opening angle as a function of distance from the apex along its shaft. (a) is calculated with the Drude–Lorentz model of the dielectric function of gold and (b) only with the Drude model. The red dashed rectangle specifies the spectral range of the CL measurements.

We further explore the identification of the coherent and incoherent radiations in the CL spectra by modulating the dielectric property of gold in a controlled way. The experimental permittivity of gold incorporates not only the response of the conduction electrons, but also the influence of band structure. In our simulations, this is fitted by the Drude–Lorentz model with two Lorentz poles in the energy range below 4 eV.[115] Here the Drude term is responsible for the conduction electron behavior, such as surface plasmons, whereas the Lorentz poles are for the intra- and inter-band transitions. Surface plasmons give rise to the coherent radiation, whereas band transitions contribute to the incoherent radiation. We can selectively switch off the band transitions by numerically switching off the two Lorentz poles. So that only the Drude model is left. In this way, we switch off the corresponding incoherent radiation in the simulated the CL spectra. A comparison of CL simulations with and

without Lorentzian poles is present in Figure 3–12 (a–b) in the broad energy range from 0.25 to 2.5 eV. The total energy at the entire six orthogonal planes is summated in the spectra. They show almost the same features including the well-defined resonances below 1.5 eV and broadband signals above 1.5 eV. The major difference is that the relatively CL intensity in the spectral range above 1.5 eV increases when switching off the Lorentz poles, which can be explained as less absorption because of inter-/intraband transitions. This result indicates that the incoherent radiation of gold taper cannot be clearly sensed by the CL measurements. It indirectly promotes that scattering and interference between coherent radiations plays the dominant role in the acquired CL spectra.
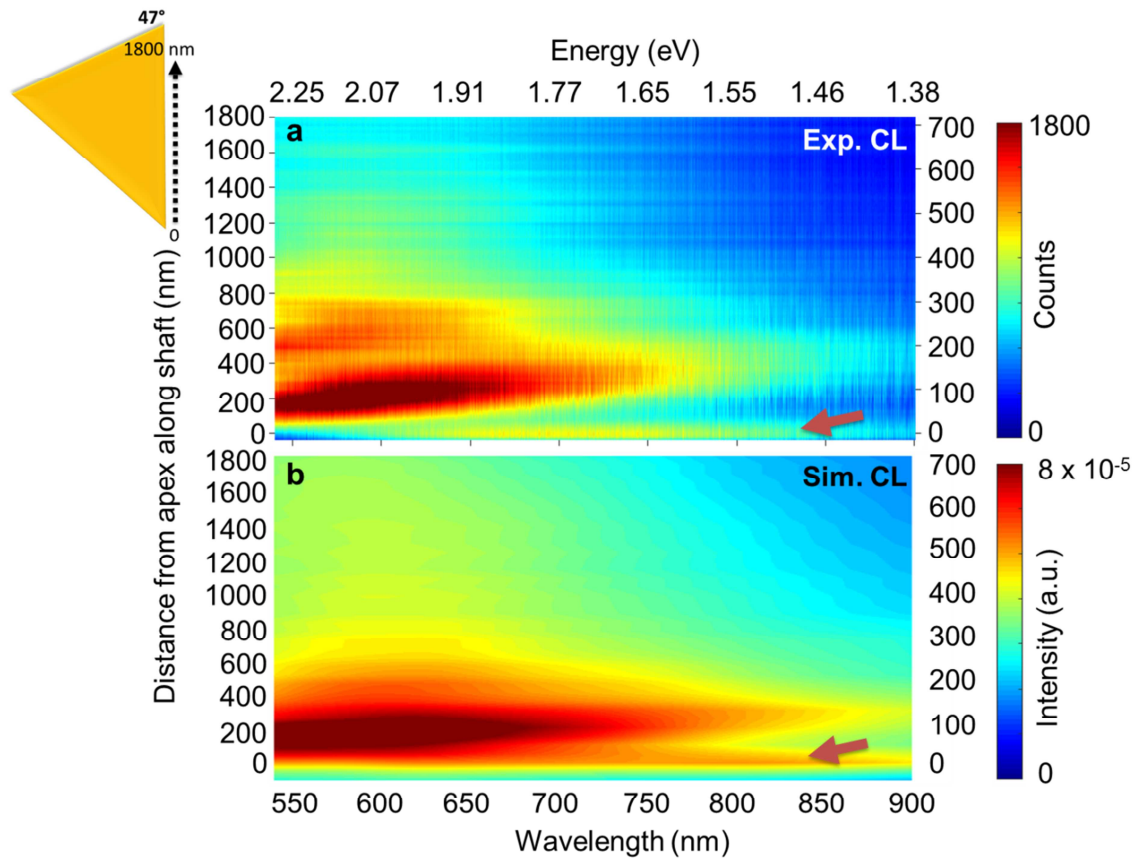
Figure 3–13. (a) Experimental and (b) simulated CL spectra of a gold taper with 47° opening angle as a function of distance from the apex along the shaft. The inset on the left indicates the scanning direction of the electron beam with respect to the taper. Red arrows indicate the broad emission at the apex.

I also compare the simulated CL spectra with the EEL spectra in a broad energy range (Figure 3–12 (c)). EELS probes both the radiative and non-radiative channels, in contrary to CL which is only sensitive to the radiative channels. Therefore, the absorption in gold tapers is expected to be the difference between EELS and CL measurements. By comparing Figure 3–12 (a) and (c), one can see that the plasmonic resonances mapped by EELS have a smooth trend in intensity spreading from 0.25 eV to 2.2 eV. However, in the CL spectra (Figure 3–12 (a)) those resonances display an intensity discontinuation around 1.5 eV to 1.75 eV. Above 1.75 eV those resonances show a slight spectral shift compared to the trend below 1.5 eV. This interesting observation is not yet fully understood, since it cannot be completely explained as absorption. Nevertheless, it might be related to the far-field interference of the emitted light,[116] which is not accessible by EELS. EELS is only sensitive to the near-field phase relation (e.g. near-field interference), in contrast, CL is sensitive to the far-field phase

shift. The far-field interference could happen between two coherent emissions, i.e. the broad-band transition radiation and the narrow-band surface plasmon radiative decay. Therefore, when there exists a phase difference of π between them, resonant Fano scattering, the interference between a continuous background and a discrete scattering process, can occur.[117] This speculation can be further tested by exchanging the excitation source from fast electrons to a dipole, as dipoles do not induce transition radiation.

Besides, we also performed CL experiments on a taper with a larger opening angle of 47° to study the influence of opening angle on the taper luminescence. As shown in Figure 3–13 (a), the signal for the radiation at the apex also becomes obvious between 600 nm to 800 nm compared to the 13° taper (red arrow). As moving away from the apex, a strong light emission in the spectral range between 540 nm to 800 nm is observed, which is similar to that in the spectra of the 13° taper. The strong emission from the taper apex is mostly due to the reduced guidance of plasmonic modes along the shaft, in which the adiabatic conditions are not fulfilled in the case of large opening angles. On the other hand, the simulated CL spectra (Figure 3–13 (b)) present a high similarity with the experimental one. It reconfirms that the scattering and the interference phenomena described by Maxwell´s equations are mainly responsible for the observed CL of gold tapers.

3.5   Conclusions

In this chapter, I resolved the plasmonic modes of gold tapers at nanoscale resolution by EELS and EFTEM (Section 3.2). I disentangled the two different dynamic mechanisms, reflection and phase matching, of surface plasmons excited by relativistic electrons in a three-dimensional single-crystalline gold taper (Section 3.3). Plasmonic modes of gold tapers with various opening angles from 5° to 47° were studied both experimentally and theoretically, by means of EELS and FDTD numerical calculations, respectively. Distinct resonances along the taper shaft were observed in tapers independent of opening angles. It is shown that, despite their similarity, the origin of these resonances is different at different opening angles and results from a competition between two coexisting mechanisms. For gold tapers with large opening angles (above ~20°), phase matching between the electron field and that of higher-order angular momentum modes of the taper is the dominant contribution to the electron energy-loss, because of the increasing interaction length between electron and the taper near-field. In contrast, reflection from the taper apex dominates the EELS contrast in gold tapers with small opening angles (below ~10°). For intermediate opening angles, a gradual transition of these two mechanisms was observed.

The opening angles of tapers determine the local radius as a function of distance from the apex. The local radius constitutes the major part of the interaction cross-section between the taper near-field and the relativistic electrons. Therefore, the larger the cross-section, the longer is the interaction between the structure and the fast electron, which facilitates the phase synchronization of the fields along the electron trajectory.

We also examined the far-field radiation of gold tapers with 13° and 47° opening angles under electron excitation by means of CL. Significant radiation between 500 and 700 nm, regardless of the opening angles, was observed, when the electrons excited the area behind the taper apex. However, when electrons exactly excited at the apex, the emission is weak for the 13° taper, in contrast to the case for a 47° taper. It has been shown that the modes, that were excited at the apex of the 13° taper, were prone to be guided away from the apex rather than coupled to the far-field radiation. We deduce that in the 47° taper adiabatic waveguiding fails and consequently causes the stronger radiation of the

plasmonic modes at the apex. The consistent strong emission between 500 and 700 nm in both tapers is not yet fully understood. Nevertheless, we can exclude the contribution of incoherent radiation (i.e. recombination of electron–hole pairs via band transitions) based on the simulation methods and the good match with the experimental results. Moreover, the far-field interference between emitted light has already incorporated in the CL simulations via solving Maxwell equations. Therefore, the measured CL data is likely to be explained as a combination of different radiation sources and the far-field interefenrence among them.

Contributions to this chapter:

Surong Guo performed the EELS and EFTEM experiments and post-analysis with the help and contribution of Wilfried Sigle (MPI-FKF). Nahid Talebi (MPI-FKF) carried out the numerical calculations. Section 3.3 has been published in ref. [118]. Surong Guo wrote the published article ref.[118] with contributions from Nahid Talebi, Wilfried Sigle and Christoph Lienau (University of Oldenburg). The project was initiated by Ralf Vogelgesang (University of Oldenburg); Martin Esmann (University of Oldenburg) and Simon F. Becker (University of Oldenburg) fabricated the single-crystalline gold tapers. Gunther Richter (MPI-IS) provided gold whiskers. Alfredo Campos and Matthieu Kociak (Université Paris Sud) performed the CL measurements together with Surong Guo. Nahid Talebi, Wilfried Sigle, Christoph Lienau and Peter A. von Aken (MPI-FKF) jointly supervised and oversaw this work.

Chapter 4　　Radiation and coupling of toroidal moments

4.1　　Introduction

Toroidal multipoles have been explicitly obtained from the multipole expansion in addition to electric and magnetic multipoles, which exhibit exotic charge–current configuration, symmetry rules and optical properties. Their fascinating characteristics have been drawing increasing research interest in the fields of solid-state physics and electrodynamics. To enrich the understanding of dynamic toroidal moments, the focus of this chapter is to experimentally and theoretically explore the associated properties of the electrodynamic toroidal moments with the assistance of metamolecules.

As toroidal moments are not as well-known as electric and magnetic moments, a brief review on toroidal moments is introduced in Section 4.2. In this section, a short history, electromagnetic properties, symmetry characters, the interaction energy, and the far-field radiation of toroidal moments will be discussed. These parts serve as background information to understand the investigations in Section 4.3 and 4.4. Although dynamic toroidal moments are the focus of this chapter, their static counterpart (static toroidal moments) have brought novelty to condensed-matter systems and have potentials for data-storing applications. Therefore, as a complement to dynamic toroidal moments, the formation of long-range-ordered static toroidal moments in condensed-matter systems as well as their novel features (symmetry and magnetoelectric effect) are briefly introduced. Sequentially, the construction of dynamic toroidal moments with metamaterials is discussed. An outlook for the application of dynamic toroidal moments is also included.

One question in this field is whether a single toroidal dipole is radiative. The current understanding is that point-like toroidal dipoles have the identical far-field radiation patterns as electric dipoles, but the power is scaled with a factor of $(\omega/c)^2$. However, there is still lack of experimental proof. In Section 4.3, the far-field radiation of toroidal dipoles based on a plasmonic nanocavity has been qualitatively verified by the experimental technique of cathodoluminescence spectroscopy. Interestingly, in the investigated structure, two toroidal modes, consisting of a single toroidal dipole and a pair of toroidal dipoles, are found and show different radiative behaviors.

On the other hand, dipole coupling is widely adopted as manipulating element to tailor optical response of electromagnetic systems. The current research focus of this field is on the novel optical phenomena generated by the interactions between single toroidal dipoles and electric and magnetic multipoles. Instead, fundamental toroidal dipole–dipole coupling is explored in this thesis, as presented in Section 4.4. The excitation configuration for toroidal dipole–dipole coupling is based on a plasmonic decamer nanocavity. The coupling phenomena have been experimentally investigated with electron energy-loss spectroscopy and energy-filtered transmission electron microscopy. All the experimental results are further interpreted with numerical finite-difference time-domain simulations, which give insights into the underlying physical mechanisms.

4.2　　Brief review of toroidal moments

4.2.1　　Toroidal moments in electrodynamics and history

The interactions between electromagnetic radiation and matter play a fundamental role in some of the most important modern technologies, for example, telecommunication, tomography, photovoltaics,

radiotherapy, *etc.* To understand the light–matter interaction, mathematical expansion sets are very useful in analytically finding approximate solutions to simple problems, which can offer a better understanding of the physical properties of systems and matter. One of these mathematical treatments is the multipole expansion that has been routinely applied in many aspects of physics. This method is based on the expansion of either electromagnetic potentials or fields and is useful for representing electromagnetic media by a set of point-like multipole sources. In other words, multipole expansion sets tell how to construct the extended electromagnetic sources by a set of localized sources, whose electromagnetic near-field and far-field radiation patterns are already well known.

Conventionally, there exist two families of sets in multipole expansion, i.e., electric and magnetic multipoles, represented by oscillating charges and looping currents. Static toroidal moments were then first considered by Zeldovich in 1957 to explain the parity violation of the weak interaction in nuclear and particle physics.[119] The derivation of toroidal moments from multipole expansion was subsequently developed and systematically described in ref. [48] by Dubovik and Tugushev. The characteristics of toroidal multipoles have also been analyzed in other refs. [120-124].

A dynamic toroidal dipole moment derived from a Taylor expansion of charge and current densities follows the expression as: [48]

$$\vec{T} = \frac{1}{10c} \int [\vec{r}(\vec{r} \cdot \vec{J}(\vec{r}, t)) - 2r^2 \vec{J}(\vec{r}, t)] d^3 r. \tag{4.1}$$

The dependency on space r and time t denotes its dynamic character. It was originally derived based on the currents flowing along the meridians of an infinitesimal sphere, where the current density $\vec{J}$ was composed of the transverse part $\vec{J_\perp}$ and the longitudinal part $\vec{J_\parallel}$. The longitudinal current $\vec{J_\parallel}$ has a direction normal to the sphere surface, whereas the transverse current $\vec{J_\perp}$ is parallel to the surface. $\vec{J_\perp}$ was shown to be responsible for the origination of toroidal multipoles. In contrast, the longitudinal current $\vec{J_\parallel}$ is related to the multipole expansion of the scalar potential, as it is connected with the charge density. The other approach to complete multipole expansion sets based on expanding potentials also shows the existence of toroidal multipoles. In this case, the consideration of both the longitudinal and the transverse parts of the vector potentials is necessary, or one can substitute the longitudinal part of the vector potential by a scalar potential due to their relation dictated by gauge theories. Furthermore, dynamic toroidal multipoles can be also obtained by the decomposition of the moment tensors according to symmetry groups.[124]

It is worth to mention that only the dynamic toroidal multipoles are suggested to be the third multipole family at the same level of electric and magnetic multipoles. The oscillating dynamic toroidal multipoles have well-defined far-field radiation patterns and can interact with electric and magnetic fields by responding to either conduction or displacement currents. However, static toroidal dipoles do not directly interact with electric and magnetic fields because of their zero external electric field and non-extended magnetic field. Therefore, they are not considered as equivalently as electric or magnetic dipoles. Nevertheless, the static toroidal moments have meaningful implication in condensed matter as promoting a new order parameter with unique symmetry rules, which will be introduced in detail in Section 4.2.4.

4.2.2 Classification of toroidal moments according to symmetry rules

The simplest model for a toroidal dipole moment is a conventional solenoid folded into a torus (Figure 4–1 (a)). In this model, the poloidal currents on the surface have only the transverse component which is parallel to the surface everywhere. As is well known, magnetic moments are generated by current loops. Therefore, the poloidal currents can be substituted by a closed circle of elementary magnets

with head-to-tail connection (Figure 4–1 (b)). This type is called polar or magnetic toroidal moment (green box in Figure 4–1).Toroidal moments in this chapter are referred to magnetic toroidal moments unless specific mentioning.

The dual configuration (e.g. an electric expression) to a polar toroidal moment is an axial toroidal moment usually denoted with $\vec{G}$, which consists of a vortex-like ring of electric moments instead (Figure 4–1 (c)). One may naturally refer to a dual model as poloidal magnetic currents flowing around a torus surface along its meridian. Although magnetic current loops are pseudo, they are mainly taken into account for the sake of completeness and symmetry.
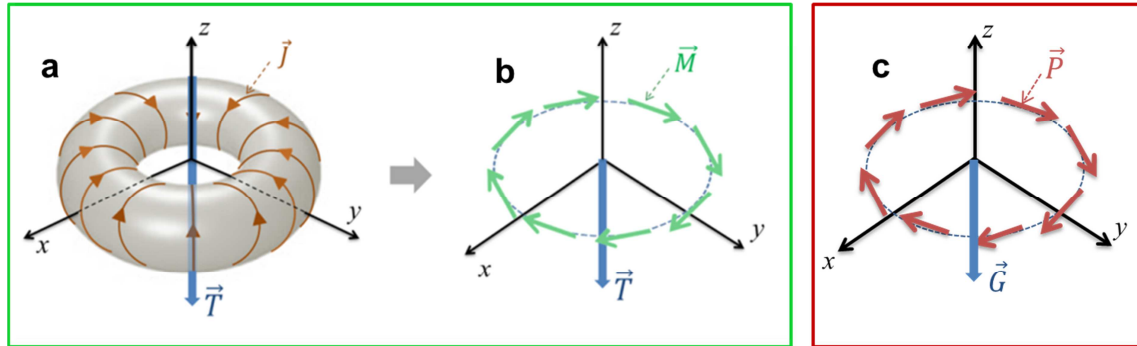
Figure 4–1. Polar (green box) and axial (red box) toroidal moments. (a) A solenoid folded into a torus with poloidal currents flowing on the surface. (b) Equivalently, a ring of magnetic moments $\vec{M}$ is also attributed to form a polar (magnetic) toroidal moment. (c) Axial (electric) toroidal moment consisting of a ring of electric dipole moments $\vec{P}$. Courtesy of Nahid Talebi for (a) and (b).

Within the quasi-static limit, the complete class of multipoles fulfills all the possible symmetry rules accordingly (Table 4–1). In complement to electric and magnetic moments, a polar toroidal moment $\vec{T}$ has odd parity under space inversion and time reversal while an axial toroidal moment $\vec{G}$ remains invariant. Even though, there is still an ongoing discussion whether toroidal multipoles are the *independent* family of elementary electrodynamic point source.[125-127]

Table 4–1. Transformation of electric (P), magnetic (M), polar toroidal (T), and axial (G) moments under space inversion and time reversal.

Parity	P	M	T	G
Space (r → −r)	-	+	-	+
Time (t → −t)	+	-	-	+

4.2.3   Interaction energy and far-field radiation of toroidal moments

Interaction between moments may lead to new energy states, which is a fundamental way of manipulating the electromagnetic properties of a system. The new energy states are associated with the corresponding interaction energy. In a hybridization picture, a negative interaction energy between the moments produces the lower-energy state of a coupled system, whereas a positive interaction energy causes the higher-energy state. In this section, the coupling of two toroidal dipole moments is considered.

The electromagnetic field of a toroidal dipole can be suitably derived by using the retarded Green's function.[122, 123, 128] Considering an infinitesimal toroidal moment with arbitrary orientation as $\vec{T}$ oscillating at the angular frequency ω, the time-harmonic field components at the position $\vec{r} = R \cdot \hat{n}$ is given by

$$\vec{E}(\vec{r}, t) = \left\{ -\frac{i\omega}{c} \frac{3(\vec{T} \cdot \hat{n})\hat{n} - \vec{T}}{R^3} + \frac{\omega^2}{c^2} \frac{3(\vec{T} \cdot \hat{n})\hat{n} - \vec{T}}{R^2} \right.$$
$$\left. + \frac{i\omega^3}{c^3} \frac{\hat{n} \times (\hat{n} \times \vec{T})}{R} \right\} \exp(i\omega t + kR) + \cdots$$

(4.2)

$$\vec{B}(\vec{r}, t) = \left\{ -\frac{\omega^2}{c^2} \frac{\vec{T} \times \hat{n}}{R^2} - \frac{i\omega^3}{c^3} \frac{\vec{T} \times \hat{n}}{R} \right\} \exp(i\omega t + kR) + \cdots$$

$\hat{n}$ is a unit vector in the direction of R. Interestingly, the electric field component of an oscillating toroidal dipole has three components depending on R^{-3}, R^{-2}, and R^{-1}, respectively, dissimilar to the electric and magnetic dipoles which depend on R^{-3} only. This fact has consequences on the interaction between toroidal dipoles and other classes of dipoles, as the interferences between the different parts causes the cancellation of the free energy at specific combinations of distance and frequency, at which the free energy becomes equal to zero.

As seen from equation (4.1), the toroidal dipole interacts with currents, including the external conduction $\vec{J}_{ext}$ and displacement current $\partial \vec{D} / \partial t$.[129] These currents can be viewed equivalently as a vortex of magnetic field according to Maxwell's equation $\nabla \times \vec{B} = \mu_0 (\vec{J} + \partial \vec{D} / \partial t)$. In case of two point-like toroidal dipoles in free space, the external conduction current is thus zero and the displacement current is linked to the electric field by $\partial \vec{D} / \partial t = i\omega \vec{D} = i\omega\varepsilon_0 \vec{E}$. Therefore, the interaction between two toroidal moments $\vec{T}_1$ and $\vec{T}_2$ in free space is given by $W^{int} \propto Re\{-i\vec{T}_2 \cdot \vec{E}_1^*(\omega, R_2)\}$ (page 150–151 in ref. [46]). Using the above equations (4.2), the interaction energy is calculated as:

$$W^{int} = -\left(3(\vec{T}_1 \cdot \hat{n})(\vec{T}_2 \cdot \hat{n}) - \vec{T}_1 \cdot \vec{T}_2\right)\left[\left(\frac{\omega}{c}\right)\frac{1}{R_{12}^3} - \left(\frac{\omega}{c}\right)^3 \frac{1}{R_{12}}\right]$$

(4.3)

with $\hat{n}$ as the unit vector along the direction of R_{12}.[130] Meanwhile, it is assumed that both multipoles oscillate at the same frequency and R_{12} is the distance between two multipoles. Very interestingly, the interaction energy has a dependence on two terms R^{-3} and R^{-1}, dissimilar to the case of coupled electric dipoles with the dependence only on R^{-3}. The interaction energy is zero when $R_{12} = c/\omega$. The interaction energy between two toroidal dipoles can be quite different at distances $R_{12} < c/\omega$ and $R_{12} > c/\omega$, even for a fixed arrangement and orientation of toroidal dipoles. This fact causes switching of the eigenenergies for symmetric and antisymmetric coupling at distances ranging from $R_{12} < c/\omega$ to $R_{12} > c/\omega$.

It should also be mentioned that for localized toroidal moments this switching might not be an obvious fact, as the critical distance $R_{12} = c/\omega$ is comparable to the wavelength, which is usually much larger than the scale of a toroidal dipole moment source. However, the switching becomes better observable in the case of non-localized toroidal moments, which can be constructed by metamaterials. The scale of these non-localized toroidal moments are comparable to the scale of the wavelength. Thus the interaction is still ongoing even at larger distances $R_{12} > c/\omega$.

The radiation pattern associated to a toroidal dipole moment is given by $\vec{S}_T = (c/4\pi)R^2\hat{n} \cdot Re\{\vec{E}(\vec{r}, t) \times \vec{B}^*(\vec{r}, t)\}$ (page 411 in ref. [46]), with here $\hat{n}$ as the unit vector along the direction of R. After algebraic reformulation the above equation is simplified to $(\omega^6/4\pi c^5) \cdot |\vec{T}|^2 \cdot (1 - (\hat{n} \cdot \vec{T})^2)$. This is quite similar to the radiation pattern of an electric dipole moment $(\omega^4/4\pi c^3) \cdot |\vec{P}|^2 \cdot (1 - (\hat{n} \cdot \vec{P})^2)$, but it is scaled with a factor of $(\omega/c)^2$.[129, 131] Particularly, they share the same multipolarity and angular radiation pattern, and show different frequency dependencies. This holds for the higher-order multipoles too, and is very important, when they coexist and compete. Interestingly, different contributions to the near-field profile of a toroidal moment cancel in the far-field pattern, and only the last term with $1/R$ in equations (4.2) contributes to the radiation pattern.

4.2.4 Static toroidal moments: toroidization and magnetoelectric effect in materials

As a complement to dynamic toroidal moments, static toroidal moments constitute the toroidal multipole family as well. They have implication in condensed matters by fostering a new order parameter with unique symmetry rules. Interesting magnetoelecric effects accompany with this long-range ordering of static toroidal moments, which can be utilized in data storing. A glance at static toroidal moments is as follows.

A static toroidal moment exists in various materials both microscopically and macroscopically, covering transition metal ions,[132] biological and chemical macromolecules,[133-138] bulk crystals[139-144] and glasses[145]. In macroscopic condensed matter, the formation of toroidal moments in materials plays a vital role in the asymmetric magnetoelectric effect (ME). The ME describes a phenomenon of a spontaneous magnetization (polarization) induced by an external electric (magnetic) field. The effect can be linear or non-linear (of higher-order), having symmetric or antisymmetric tensors and usually depends on temperature. An antisymmetric tensor is described by $[\xi]^{\mathrm{T}} = -[\xi]$, where T is the transpose operator. Moreover, an antisymmetric tensor is a special case of an asymmetric tensor, where the latter is described by $\xi_{ij} \neq \xi_{ji}$. One consequence of the antisymmetric linear magnetoelectric effect in materials is toroidization, which is denoted by forming an order of vortices of the spontaneously induced magnetization[144] or spins[146].

In solid-state systems where the magnetic fields are induced by localized spins ($\vec{S}_\alpha$) at sites $\vec{r}_\alpha$, the toroidal moment can be derived as $\vec{T} = (g\mu_B/2)\sum_\alpha \vec{r}_\alpha \times \vec{S}_\alpha$, with the gyromagnetic ratio g and the Bohr magneton μ_B. However, toroidal moments have origin-specific values related to the choice of the lattice.[147] By shifting the origin from $\vec{r}$ to $\vec{r}' = \vec{r} + \vec{R}_0$ the toroidal moment changes as $\vec{T}' = \vec{T} + (g\mu_B/2)(\vec{R}_0 \times \sum_\alpha \vec{S}_\alpha)$. In contrast to the moment, changes in toroidization (toroidal moment per volume of unit cell) are uniquely defined values. Nevertheless, as for ferroelectric materials, spontaneous toroidization can be defined in materials with net toroidal moments, which describes the rate of change in toroidal moments, when a vector field is applied. In general, symmetry considerations hint at the contribution of toroidal moments to the magnetoelectric polarization, when considering the free energies of systems with spin ordering and the electrodynamics Hamiltonian of systems showing the linear magnetoelectric effect. However, toroidal moments are not the only source of the magnetoelectric effect. It is almost impossible to provide a direct relation between toroidization and magnetoelectric coupling.[146] Non-equilibrium electrodynamics consideration can describe the differences in the off-diagonal magnetoelectric tensors below a critical temperature, which is related to the coupling between the spontaneous toroidization, magnetization, and polarization.[148-150] In general

the antisymmetric contribution to the magnetoelectric tensor is an indication for the presence of toroidization in materials.

Ferrotoroidicity describes a spontaneous, long-range alignment of toroidal moments in materials. It has been of major interest to investigate, whether the ferrotoroidicity consisting of magnetic toroidal moments can be defined as an individual class of ferroic state, in addition to ferroelastic, ferromagnetic and ferroelectric orders.[144, 146, 151-153] The reason is that the ferrotoroidicity complements the others in terms of space-time-inversion symmetry, whose transformation property is characterized by changing sign under both time reversal and spatial inversion.[142] In this sense, the ferrotoroidic state in materials is expected to be dominant like other primary order parameters. Zimmermann et al. demonstrated for the first time the hysteretic switching of ferrotoroidic domains in $LiCoPO_4$, where they simultaneously applied crossed static magnetic and electric fields.[151] They concluded that the ferrotoroidic order is a primary order parameter as other ferroic states.

It has been further discussed that the toroidal moment might be merely a vortex-like arrangement of magnetic moments from an antiferromagnetic state. Tolédano *et al.*[144] proposed a case study of $LiFeSi_2O_6$ in this aspect. All the magnetoelectric tensor components during the symmetry-breaking transition from a monoclinic to a triclinic magnetic phase at 18 K in $LiFeSi_2O_6$ were measured. In terms of crystallographic symmetry, either a biquadratic coupling of the toroidal-moment vector components or the antiferromagnetic vector components is permitted and is able to explain the observed inversion symmetry breaking. However, in terms of microscopic physics, only the free energy of the toroidal coupling term can be large enough to drive the transition in a single step. This is due to the fact that the free-energy contribution from the antiferromagnetic vector components is geometrically attenuated. Therefore, to distinguish ferrotoroidicity from ferromagnetic order in a material, it is necessary to examine both the crystallographic symmetry and the collective response of the associated moments.

As mentioned previously, in systems with nonvanishing magnetic moments the toroidal moment depends on the choice of origin.[147] It was suggested to choose an origin for which the system is centrosymmetric and nontoroidal in the initial configuration. The change of toroidal moment is then derived from a symmetry-breaking structure distortion at the final state and thus can be interpreted as the spontaneous toroidal moment of the system.[147] Ferrotoroidicity has been demonstrated by the materials whose magnetic order breaks the spatial inversion symmetry. It is waiting for exploration in a variety of material systems and holds a great potential for future applications.[152]

Experimental characterization of ferrotoroidic states requires a probe and a detection mechanism which violates space–time symmetry. Obviously, the measurement of magnetoelectric coefficients is an appropriate, however indirect method for investigating toroidal moments in materials, as was achieved for $Co_3B_7O_{13}Br$[148] and Cr_2O_3, only when it starts to be driven into the spin-flop phase at 58 kOe (or 5.8 T).[154] Moreover, the magnetoelectric tensor of Cr_2O_3 sustains also a relativistic-invariant pseudoscalar term,[155] which is associated with the axionic magnetoelectric effect[156] and the so-called Tellegen term.[157]

Considering the magnetic insulator $LiCoPO_4$ and the *XY*-like spin glass $Ni_xMn_{1-x}TiO_3$ (x ≈ 0.42) as examples, $LiCoPO_4$ has a net toroidal moment $T (0,T_y,T_z) \neq 0$ below 21.8 K.[151] The predominant component T_z of the toroidal moment is induced by two pairs of Co^{2+} (each pair highlighted in purple or green in Figure 4–2 (a)), while the other component T_y caused by spin rotation away from the *y*-axis is approximately two orders of magnitude smaller and thus can be neglected.[151] For the ilmenite structure of the *XY*-like spin glass $Ni_xMn_{1-x}TiO_3$ ($x ≈ 0.42$), the Ni^{2+} and Mn^{2+} ions are randomly distributed in the magnetic (Ni, Mn) plane and form a honey comb lattice. At the presence of the

cross-product of the electric and magnetic field components, a net toroidal moment is polarized in the direction perpendicular to the honeycomb lattices during the spin-freezing process below 10 K (in Figure 4–2 (b)).[145]

Apart from toroidization in bulk material at low temperatures, toroidization might be achieved at room temperature by interface engineering due to structural modification, charge transfer and strain effects.[158, 159] Figure 4–2 (c) shows one possible interface type of (-Fe-FeO-TiO$_2$-BaTiO$_3$) between Fe and BaTiO$_3$, which results in a spontaneous magnetization and polarization at room temperature. Polar vortices for an electric toroidal moment are observed in oxide superlattices (SrTiO$_3$ and PbTiO$_3$),[159] as shown in Figure 4–2 (d). However, in the experiments mentioned here, where the spatial-temporal symmetry was broken with a strong correlation across the interface, it is the quantity $\vec{P} \times \vec{M}$ (electric $\vec{P}$ and magnetic $\vec{M}$ dipole moments) which contributes to the detected time-averaged signal.
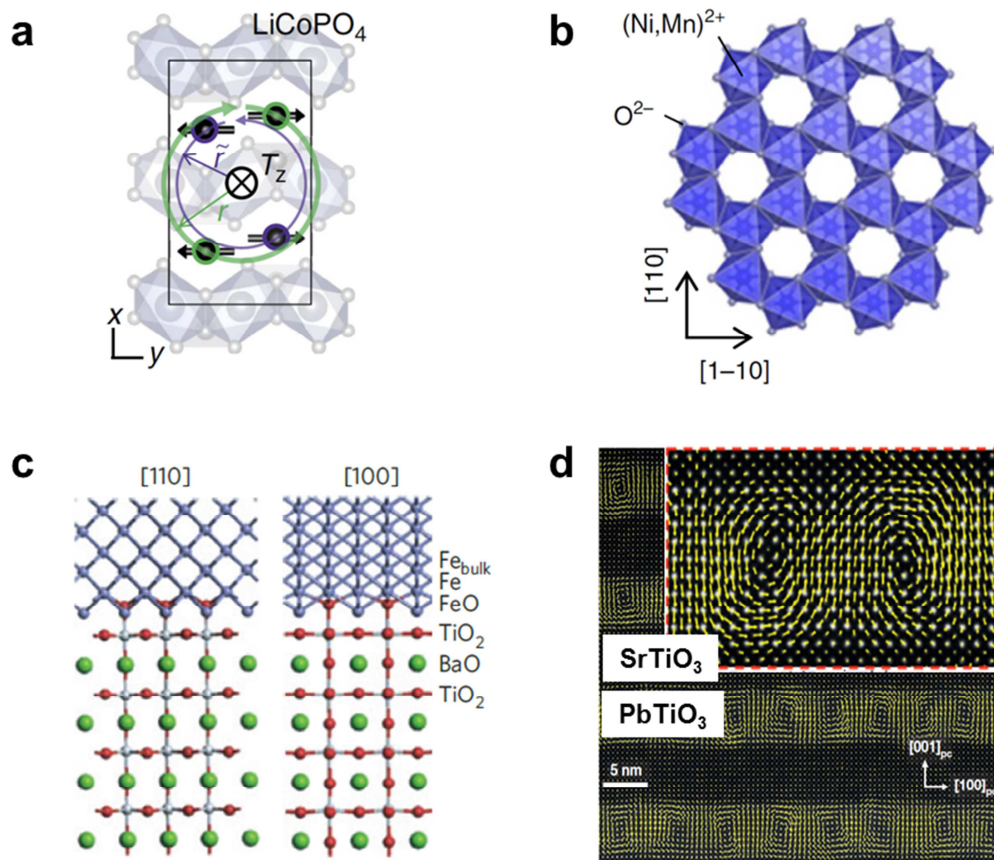
Figure 4–2. Examples of toroidal moment in materials. (a) Z-component of the toroidal moment in LiCoPO$_4$ originated from two spin pairs in Co^{+2} shown for its magnetic unit cell (rectangle).[151] Because of the different radii $\tilde{\vec{r}} < \vec{r}$, the clockwise and counterclockwise contributions from these two pairs do not cancel. (b) Crystal structure of Ni$_x$Mn$_{1-x}$TiO$_3$ projected along the hexagonal c axis [001].[145] (c) Structural model of the interface type (-Fe-FeO-TiO$_2$-BaTiO$_3$) between Fe and BaTiO$_3$.[158] (d) An array of vortex–antivortex pairs present in each PbTiO$_3$ layer indicated by polar displacement vectors (yellow arrows).[159] Figures reproduced with permission from: (a) ref. [151], Nature Publishing Group (NPG); (b) ref. [145], NPG; (c) ref.[158], NPG; (d) ref. [159], NPG.

For long-range toroidal moments in condensed-matter systems, their inherent magnetoelectric effect is of technological interest, since it provides an alternative and convenient way for manipulation of data in, for example, storage discs. Indeed, data storing on the nanoscale can be realized by switchable, ordered electric toroidal moments in low-dimensional ferroelectric structures.[160, 161] Moreover, the

switching of toroidal moments requires no electrode contact on the nanoscale, but is conveniently controlled by time-dependent magnetic fields. Additionally, it exhibits no noticeable cross-talk.[161] As for the case of $LiCoPO_4$, the generation and manipulation of ferrotoroidic domains was implemented by simultaneously applied magnetic and electric fields, not solely by either of the fields alone.[151] It gives the material a promising potential to reject external disturbance in data storage, as an illustration. Moreover, the intrinsic linear magnetoelectric effect of ferrotoroidic materials is anticipated to be a source of giant magnetoelectric effects via effective enhancement.[153]

4.2.5   Dynamic toroidal moments in artificial metamolecules and dielectric nanostructures and their applications

In addition to static toroidal moments in various condensed materials, engineered toroidal moments using the concepts in plasmonic and metamaterials[162] cause growing interest, as such moments can be excited by and interact with electromagnetic fields more efficiently than the toroidal moments in condensed matter.[125] This helps us to understand the basis of dynamic toroidal moments interacting with light as well as modifying the optical properties of materials.

However, the toroidal dipole response in electrodynamics is often masked by more dominant electric and magnetic multipoles at similar energies. Therefore, artificial toroidal metamaterials are initially designed to amplify toroidal moments and suppress the competing electric and magnetic multipoles. This interesting field was set off by mimicking toroidal coils[125, 163] at microwave frequency to explore the toroidal dipole response in a great variety of structures as well as entering the optical regime by scaling structures down to the nanoscale.[164] Figure 4–3 gives a brief but not complete overview of different investigated toroidal metamolecules in catalogues of split-ring resonators and their variants, magnetic resonators, apertures, plasmonic cavities and structures, and dielectric nanostructures. It should be mentioned that the classification of metamaterials is not restricted to a single catalogue, for example, metallic double disks can be considered either as magnetic resonators[165, 166] or as plasmonic cavities.[167] There are also other novel designs, for example, vertically assembled dumbbell-shaped apertures and split-ring resonators resulting in a horizontal toroidal response in the optical region.[168, 169]

The far-field radiation patterns of a toroidal moment are virtually identical with those of dipolar electric and magnetic moments, even though these moments are fundamentally different[129, 131] (see Section 3d). The destructive interference between their radiation patterns has been exploited to construct a non-radiating scatterer. This approach is called the *anapole excitation*,[173] *scattering transparency*[183] or *analogous electromagnetic induced transparency*.[171] Such an intriguing design has promising potential applications in designing low-loss, high-quality factor cavities for sensing, lasers, qubits, and non-scattering objects for cloaking behavior.

In parallel, the dielectric metamaterial[186] was proposed to overcome dissipation loss of metals as encountered in metal-based toroidal metamaterial.[181] It has been pointed out that dissipation losses in metals originating from the Ohmic resistance can hinder the excitation of toroidal multipoles, especially in the optical regime, resulting in weak coupling to external fields.

A fantastic characteristic of toroidal metamaterials as aforementioned is the feasibility in tuning toroidal responses via size, shape, material,[183] spatial arrangement and symmetry[187] of the constitutive elements.[188] So far, the major existing toroidal metamolecules are designed to achieve pronounced magnetic toroidal dipole response due to their peculiar property of asymmetry in both spatial inversion and time reversal. In this case, introducing space-inversion asymmetry, from either the geometry or the

excitation source, is necessary for toroidal moment excitation, while breaking time-reversal symmetry has already been fulfilled by the magnetic dipole intrinsically. These toroidal artificial structures open an avenue to study the interaction with electromagnetic radiation in both the far-field and the near-field.
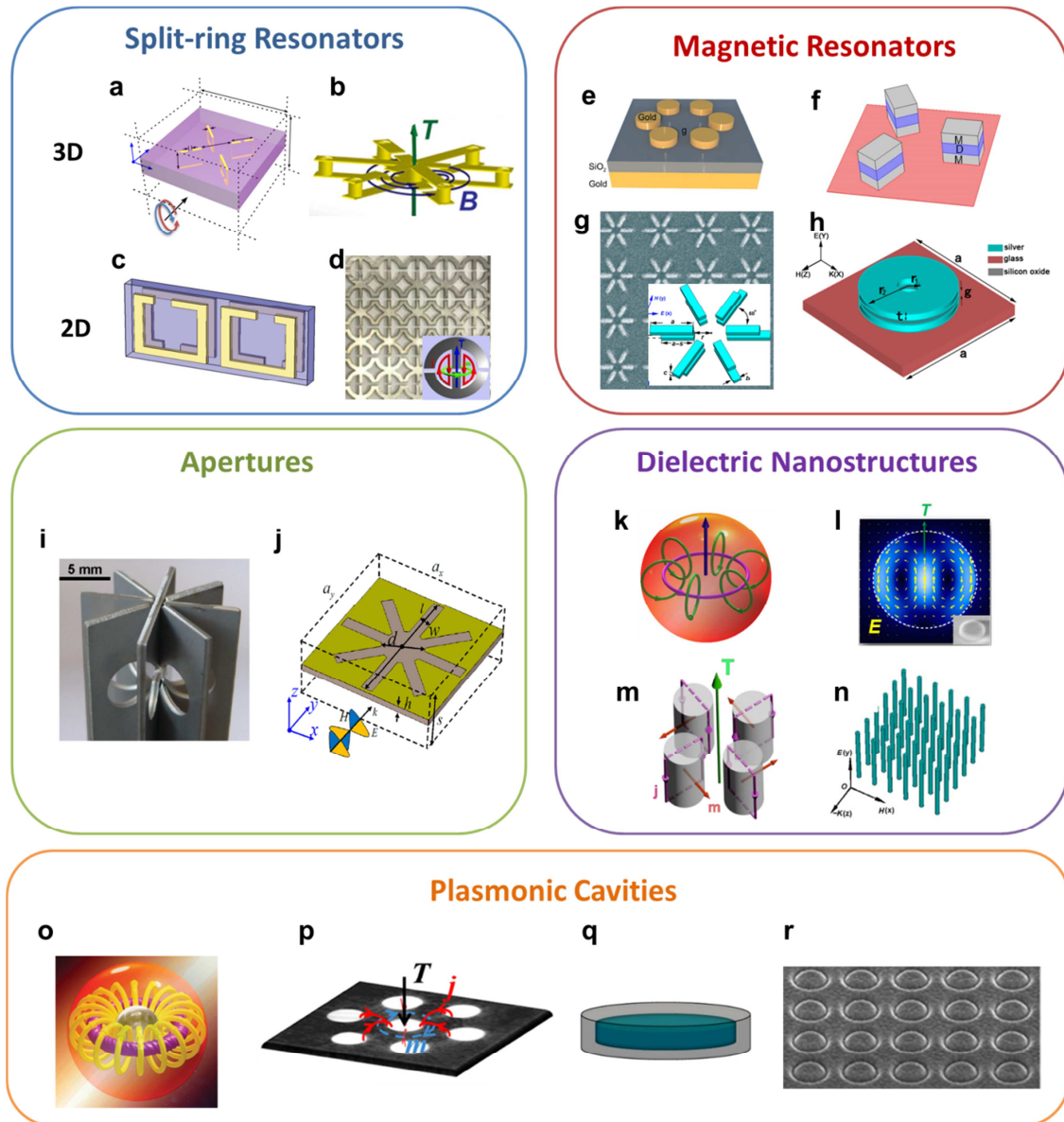
Figure 4–3. Split-ring resonators (SRR): (a) Schematic drawing of 3D SRR constituted by four rectangular metallic wire loops embedded in a dielectric slab.[170] (b) A combined SRR by sharing a central connecting bridge.[171] (c) An asymmetric SRR-based planar toroidal metamaterial.[172] (d) Planar conductive metamaterial formed by two symmetrical split rings.[173] Magnetic resonators: (e) an optical toroidal structure composed of a gold hexamer and metallic mirror separated by a dielectric layer.[174] (f) Three magnetic resonators consisting of two metallic rods and a dielectric spacer.[166] (g) An infrared toroid metamaterial composed of asymmetric double bars.[175] (h) A THz flat-ring-dimer (metallic double disks) toroidal metamaterial.[176] Apertures: (i) Toroidal metamaterial arrays consisting of dumbbell-shaped apertures manifests the destructive interference between electric and toroidal dipole moments leading to scattering transparency.[177] (j) An electric toroidal dipolar response has been achieved by a metamaterial-based on sun-like aperture element at microwave frequency.[178] Dielectric nanostructures: (k) Dielectric nanoparticle.[179] (l) Dielectric nanodisk with illustration of toroidal electric field distribution.[180] (m) Dielectric cylinders.[181] (n) Dielectric nanotubes.[182] Plasmonic cavities: (o) Core–shell nanoparticles support toroidal dipole excitation by a plan wave.[183] (p) Plasmonic oligomer nanocavities with 7 nanoholes in metallic films sustain toroidal responses at visible wavelengths.[47] (q) Toroidal modes are sustainable in the infrared and visible regime by

sidewall-coated plasmonic nanodisk antenna.[184] (r) Circular V-groove array supports plasmon toroidal mode at optical frequencies.[185] Figures reprinted with permission from: (a) ref. [170], American Physical Society (APS); (b) ref. [171], WILEY-VCH Verlag GmbH & Co. KGaA,Weinheim; (c) ref. [172], APS; (d) ref. [173], APS; (e) ref. [174], NPG; (f) ref. [166], by courtesy of Jing Chen; (g) ref. [175], American Institute of Physics (AIP); (h) ref. [176], Elsevier B.V.; (i) ref. [177], NPG; (j) ref. [178], AIP; (k) ref. [179], The Optical Society (OSA); (l) ref. [180], NPG; (m) ref. [181], APS; (n) ref. [182] , OSA; (o) ref. [183], WILEY-VCH Verlag GmbH & Co. KGaA,Weinheim; (p) ref. [47], AIP; (q) ref. [184], American Chemical Society (ACS); (r) ref. [185], OSA.

Depending on the polarity of the light and the spatial symmetry of the metamaterial structures, different strategies are used to excite toroidal moments in metamaterials. In the literature, external light, with either linear,[190] radial,[174, 189] or circular polarization[170, 178] has been used to illuminate the metamaterials normally, laterally, or obliquely (Figure 4–4).

In general, the polarization of the electric field of the incident light induces effective current loops in the structure, which generates magnetic dipoles. By carefully arranging the structure elements and the polarization direction of the incident light, a vortex of magnetic dipoles, i.e. a toroidal moment, is thus achieved. For instance, split-ring resonators usually are illuminated from a lateral direction.

Formation of toroidal moments in a spatially confined hybrid electric-magnetic configuration leads to unusual properties, which opens a horizon of potential applications in data storing[160] and designing of low-loss metamaterials or metadevices,[190-193] such as ultrasensitive sensors and diagnostic tools,[170, 194] polarization twister,[178] near-field lasing,[195] and lasing spacer.[196]
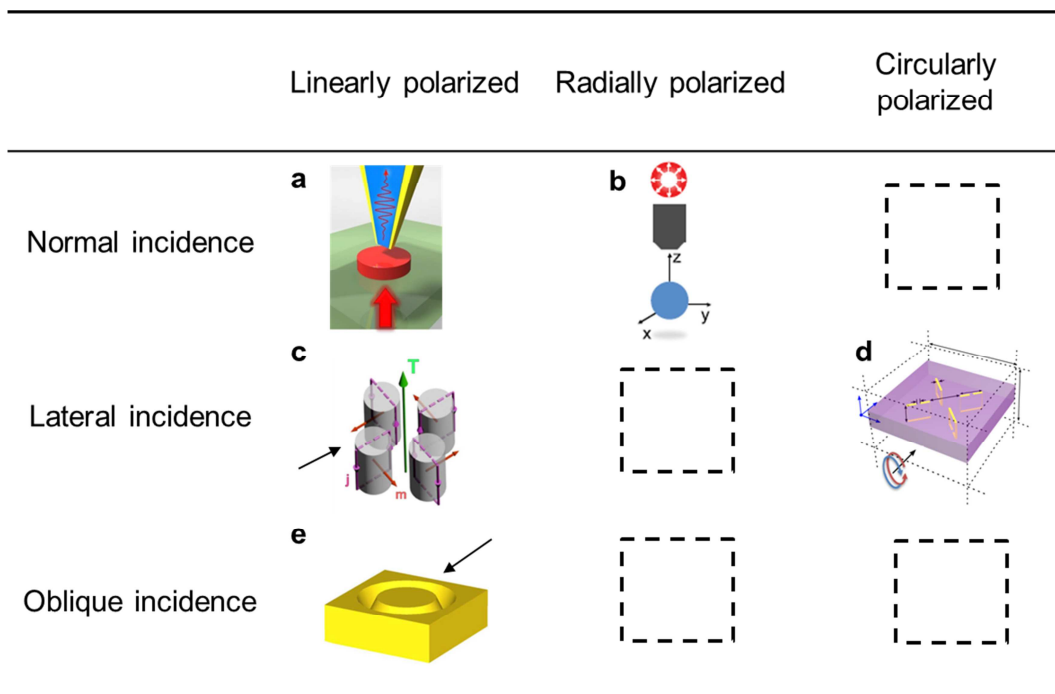
Figure 4–4. Different excitation strategies for toroidal moments in metamaterials via polarization and incidence directions. Dashed boxes denote no published result yet. Figure reproduced from: (a) ref. [180], Creative Commons CC-BY license; (b) ref. [189], OSA; (c) ref. [181], APS; (d) ref.[170], APS; (e) ref.[185], OSA.

Benefiting from more confinement in real space, dynamic toroidal dipolar excitation in metamaterials usually achieves higher quality factors by carefully designing the geometry[190-192] and the chemical component.[195] It paves the road for applications as low-loss, high-Q cavities in meta-devices (Figure 4–3 (c) and (d))[172, 173, 190, 192, 193] and laser spacer.[196] Through destructive or constructive interference between toroidal multipoles and electric or magnetic multipoles astonishing electromagnetic

phenomena can be achieved, such as manipulation from non- to super-radiating,[189, 197] resonant transparency (Figure 4–3 (i) and (n)),[177, 183, 198] extremely high Q-factors[173] and nanolasering in the near-field.[195]

Instead of local toroidal excitations, a propagating toroidal excitation in free space, as a peculiar form of delivering an electromagnetic field, is intriguing. This concept was introduced in 1996 as *focused doughnuts,* a single-cycle, broad-bandwidth pulse with a spatially localized toroidal field configuration and longitudinal field components.[199] It was numerically shown that such pulses allow to excite a prominent toroidal dipole mode in a dielectric nano-sphere.[200] The challenge of realizing such a focused doughnut lies in simultaneously controlling frequency and spatial dispersion over a wide bandwidth.[129]

Another peculiar feature of toroidal moments is circular dichroism.[170, 194] It is seemingly challenging the common interpretation based on electric and magnetic quadrupoles, and also might have a potential in diagnosing and sensing fields.[170] Moreover, an effective conversion between left-handed to right-handed circularly polarized waves at the same frequency has been demonstrated via arrays of sun shape apertures Figure 4–3 (j).[178] It can be potentially applied as polarization twister at the microwave region.

4.3   Radiation of dynamic toroidal moments in oligomer nanocavities

Plasmonic heptamer nanocavity in a silver thin film has been proved to support toroidal dipole excitations. Under the irradiation of fast electrons, a magnetic toroidal dipole is induced on the central hole with a head-to-tail vortex configuration of magnetic dipoles in the outer 6 nanoholes.[8] I adapted toroidal moments sustained by this structure to investigate their corresponding radiation properties. As shown in Figure 4–5 (a), the fabricated heptamer structure has a hole diameter of 80 ± 10 nm, and the thickness of the silver thin film is around 30 ± 15 nm.

I first employed near-field measurements with EELS to probe the resonances of supported toroidal modes in the heptamer structure with a selective excitation scheme along its symmetry axis (Figure 4–5 (a)). First of all, the single toroidal dipole moment is easy to be recognized in energy-loss spectra by its characteristic excitation location. This mode has the energy highly concentrated at the central hole and the nearby silver bridges,[8] where exactly the corresponding energy-loss signal should be present (vertical dashed red line, named T1 mode). The extracted experimental EEL spectra at the positions depicted by colored spots between the central and upper holes are displayed in Figure 4–5 (c) left column. It shows that the T1 mode is excited at both the central hole and neighboring silver bridge. Meanwhile, it has a broadband feature with the peak center at around 2.12 eV. On the other hand, there is another pronounced resonance at 2.58 eV with the energy concentrated just at the silver bridges (vertical dashed black line in Figure 4–5 (a) and (c), named T2 mode). Contrary to the T1 mode, this mode is absent at the central hole, but is excited at the silver bridges and the rims of the holes (Figure 4–5 (c)). Certainly, other cavity modes can also be excited in this structure as reported previously in the ref. [8] and [47]. However, here I only focus on the toroidal moments for the sake of relevance. The zig-zag curve above 2.6 eV is a camera artifact due to the afterglow of ZLP, which will not affect the data interpretation.

Figure 4–5 (b) shows the corresponding simulated EEL spectra via the FDTD numerical calculations. The individual spectra extracted between the central and upper holes are shown in Figure 4–5 (c) right column with the same color code used for the experimental spectra. Two pronounced resonances are observed at 2.1 and 2.5 eV, respectively (vertical dashed red and black lines). They show good

agreement with the experimental T1 and T2 modes despite of a slight energy shift of around 0.1 eV. By displaying the electromagnetic field distributions at 2.1 eV (Figure 4–6 (a)), it confirms the excitation of the single toroidal dipole moment with the clockwise rotation of the magnetic dipoles in the outer 6 nanoholes (red arrow in H_z field) and high electric field concentration at the central hole and the nearby silver bridges (E_z field). Very interestingly, the resonance at 2.5 eV demonstrates an antiparallel pair of toroidal dipoles (Figure 4–6 (b)). The instant magnetic field distribution at $\pi/4$ shows a clockwise dipole loop in the upper 4 nanoholes (including the central hole) as well as a counter-clockwise dipole loop in the lower 4 nanoholes (including the central hole), indicating an antiparallel pair of toroidal dipoles perpendicular to the paper plane. The corresponding electric field distribution reveals that the energy of this mode is mainly concentrated between the holes (silver bridges) along the symmetry axis. Figure 4–6 (c) gives a glance of the field evolution of the T2 mode over half a harmonic period of π, where the full harmonic period of the T2 mode takes 2π. In general, the magnetic field H_z (red curve) has a time shift of $\pi/2$ with respect to the electric field E_z (black curve) due to the dynamic nature of electromagnetism. At the beginning of the period (i.e. 0), a loop of magnetic dipoles is only observed in the lower 4 nanoholes (H_z field at the bottom in Figure 4–6 (c)), and the corresponding electric field is mostly concentrated in the silver bridge between the lower 4 nanoholes. Hence, only one toroidal dipole is shown. After a time of $\pi/4$, an additional loop of magnetic dipoles appears in the upper 4 nanoholes, which assembles another toroidal dipole. Together with the toroidal dipole excited in the lower 4 holes, they now form an antiparallel pair of toroidal dipoles as already presented in Figure 4–6 (b). At the time of $\pi/2$, only the toroidal dipole in the upper 4 nanoholes is dominant (H_z field in Figure 4–6 (c)). Therefore, these two constituent toroidal dipoles appear one after another in the time domain with a shift of $\pi/2$. Over a complete time period, the net dipole moment is zero, which indicates a character of a dark mode. It implies a non-radiative behavior of this mode unless retardation plays a role.[201] Retardation becomes important when the size of the structure is larger than the resonance wavelength. In our case, however, the diameter of the entire heptamer structure (350 nm) is smaller than the wavelengths of the T2 mode (585 nm). Therefore, I expect a strong CL signal of the T1 mode but no significant CL signal of the T2 mode.

With the above knowledge on the toroidal moments in the investigated plasmonic heptamer nanocavity, we first calculated the corresponding CL spectra on the same structure along the symmetry axis in order to correlate the simulated EELS results in a controlled way (Figure 4–7 (a)). The qualitative correlation between the simulated CL and EEL spectra on the same structure can be later applied to interpret the experimental CL data. In the following, I consistently use vertical dashed red and black lines for the denotation of the T1 and T2 modes at their free-space wavelengths, respectively. The main feature of the simulated CL spectra is a strong emission spanning from 500 to 650 nm present on the silver bridges, whereas such signal is weaker inside the central hole. I compare the simulated CL and EELS spectra at the positions of the central hole and the neighboring silver bridge, which are the representative excitation locations for T1 and T2 modes, respectively (red and black crosses in Figure 4–7 (a)). At the central hole, the T1 mode is exclusively excited according to the EEL spectrum (solid red curve in Figure 4–7 (c)). The corresponding CL spectrum indicates a blue-shift of the T1 mode to 510 nm with respect to its near-field resonance (blue arrow with red edge and the dotted red curve in Figure 4–7 (c)). It is not unusual to observe spectral shift between EELS and CL spectra because of electromagnetic dissipation of excited modes.[17] In addition, the T1 mode displays a higher intensity in the silver bridges than in the central hole either in the CL (Figure 4–7 (a–b)) and EEL spectra (Figure 4–5 (a–b)). This feature is likely attributed to a higher coupling efficiency of inducing polarized currents on the material rather than in the void in order to form the toroidal moments. On the other hand, at the silver bridge both T1 and T2 modes can be excited (solid black curve in Figure 4–7 (c)). However, only the peak of the T1 mode at 510 nm is observed (vertical solid red line) in the simulated CL spectrum (dotted black curve). Assuming that the simulated CL signal of
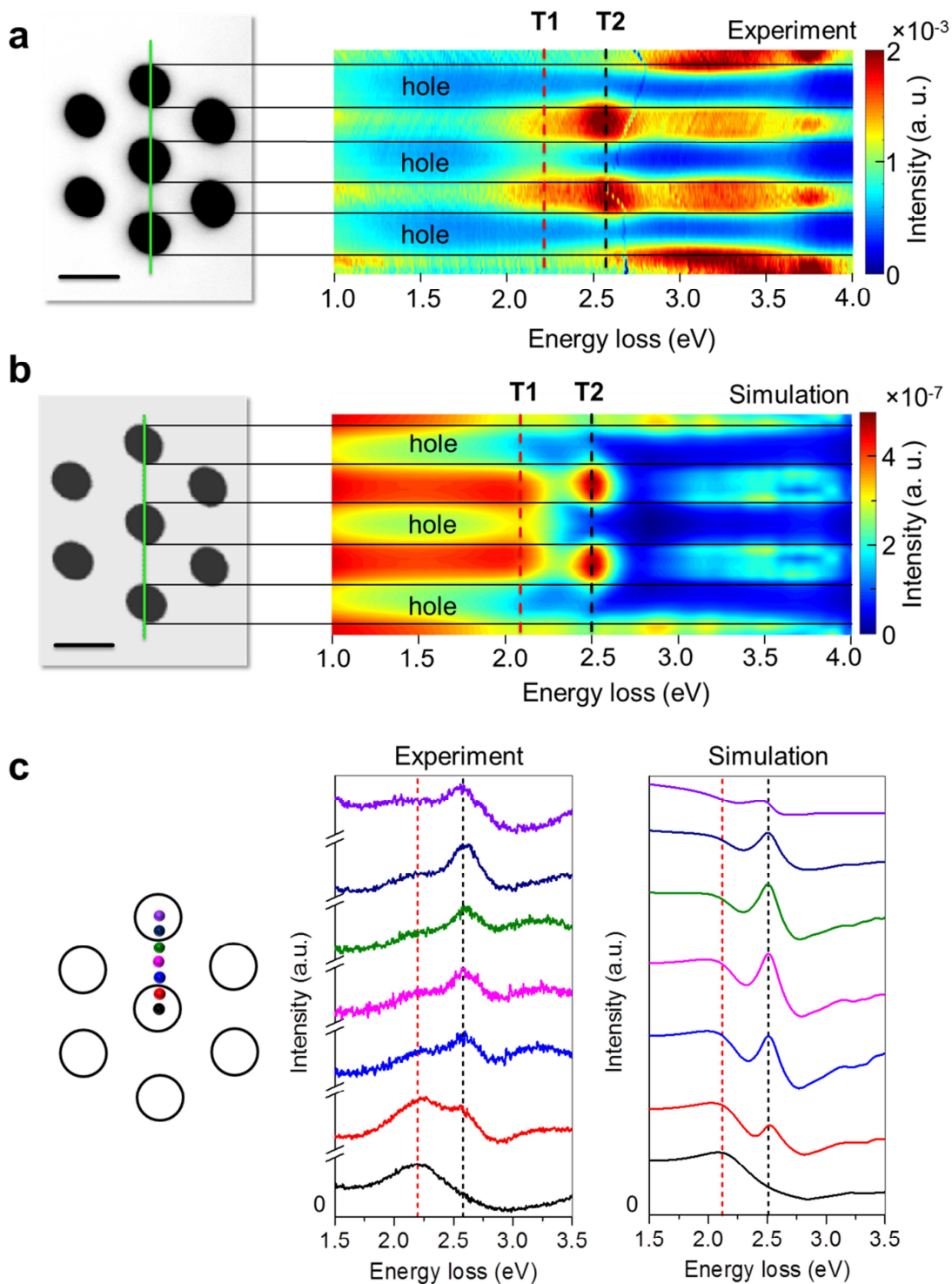
Figure 4–5. (a) HAADF image (left) and ZLP-normalized EEL spectra recorded along the green line of a fabricated heptamer nanocavity. (b) Image of the simulated heptamer cavity (left) and the corresponding EEL spectra along the cavity axis (green line). Scale bars are 100 nm. Vertical dashed red and black lines indicate the toroidal modes T1 and T2 at (a) 2.12 eV and 2.51 eV, and (b) 2.2 eV and 2.58 eV, respectively. (c) Experimental (left) and simulated (right) EEL spectra of the investigated plasmonic heptamer cavity along the symmetric axis from the central to upper holes as depicted by colored spots in the inset.

the T2 mode is subjected to the same amount of blue-shift as the T1 mode has, it is then expected to see a peak around 419 nm indicated by the vertical solid black line. However, no significant peak but a very shallow raise is observed (dotted black curve). In fact, this shallow raise is also observed in the simulation CL spectrum at the center of the central hole (dotted red curve), at which the T2 mode is absent. Therefore, the shallow raise at 419 nm might be the signal of other cavity modes. Nevertheless, compared to the relative CL intensity of the T1 mode (vertical solid red line), the CL probability at 419 nm (vertical solid black line) is obviously lower (dotted black curve). In general, the simulated CL results match the previous prediction that the T1 mode is radiative (i.e. bright mode) in contrast to the non-radiative behavior of the T2 mode (i.e. dark mode). The above observations via comprising the simulated EEL and CL spectra offer an important hint to interpret the corresponding experimental CL data.

Figure 4–7 (b) shows the experimental CL spectra along the structural symmetry axis. Similar characters, like broad signal from 500 to 650 nm and the higher intensity in the silver bridges than in the central hole, appear as in the simulated CL spectra. For details, Figure 4–8 (a–b) shows the simulated CL spectra alongside the experimental spectra extracted from similar locations along the structural symmetry axis (color-coded locations in Figure 4–7 (b)). Despite the similarity, the measured emission of the single toroidal T1 mode has almost no spectral shift with respect to its EELS resonance at 2.2 eV (vertical dashed red line at 564 nm in (b)). This may imply a low damping rate of the single toroidal dipole mode in the investigated structure. However, there are two small peaks appearing around 565 nm highlighted by the inverse black and red triangles in Figure 4–8 (b). To further investigate the possible difference between them, I examined the corresponding spectral-spatial distribution at these 3 resonances (590, 564 and 540 nm) by displaying their chromatic CL maps (first row in Figure 4–8 (c)). Interestingly, they all show the same distribution feature corresponding to the electric field E_z of the T1 mode (Figure 4–6 (a)). Therefore, it indicates the single excitation of the T1 mode and the broadband emission feature of the single dynamic toroidal dipole moment. As a speculation, these small peaks may be the intensity variation resulting from the far-field interference between multiple plasmonic modes.
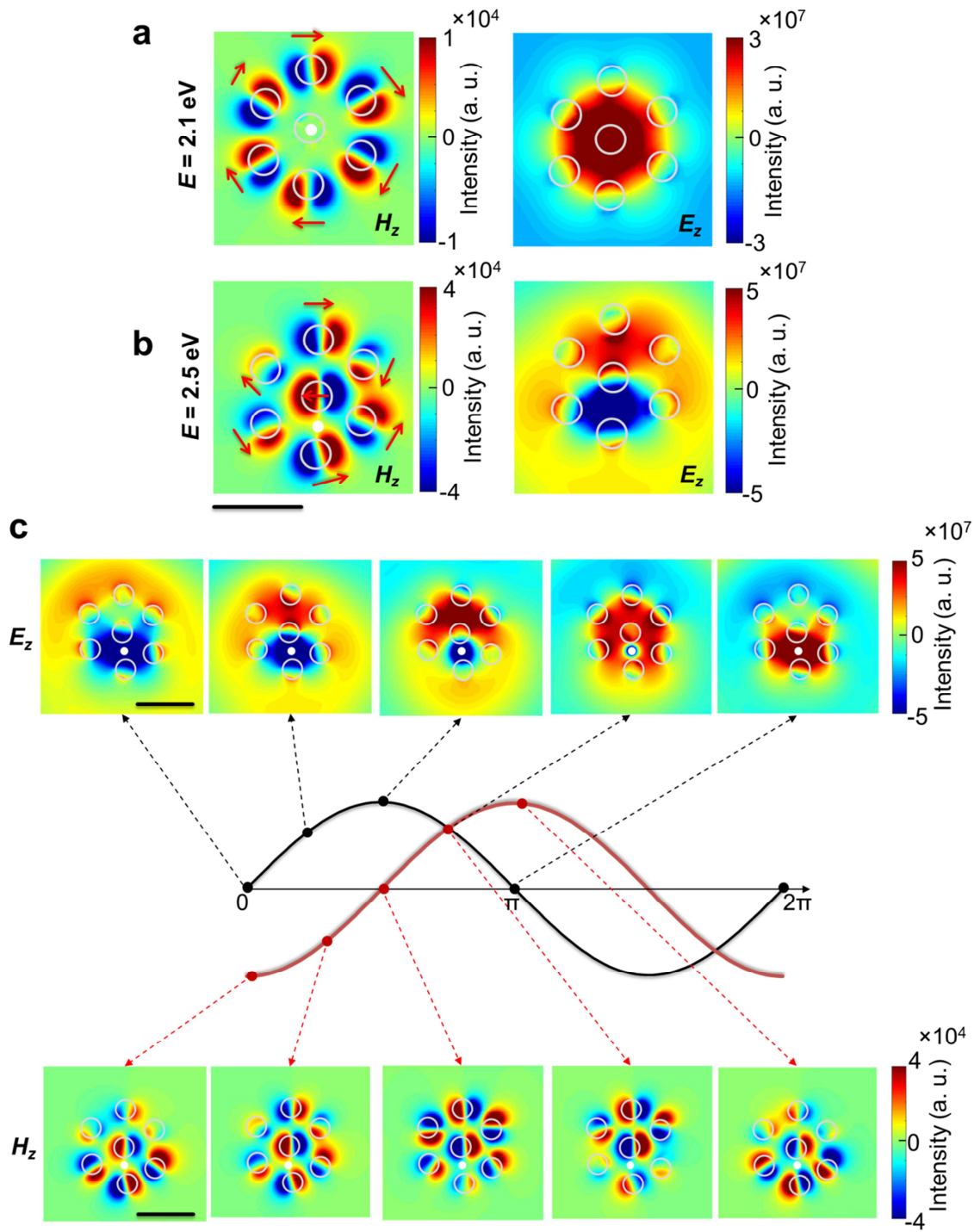
Figure 4–6. Simulated magnetic and electric fields, H_z and E_z, along the electron trajectory of the heptamer structure (a) at 2.1 eV without time delay and (b) at 2.5 eV with $\pi/4$ time delay, respectively. (c) Evolution of the simulated electric field E_z and magnetic field H_z of the T2 mode at 2.5 eV from 0 to π at $\pi/4$ intervals. Grey circles denote the nanoholes. The impact locations of the electron probe are indicated by the white dots. Red arrows show the directions of magnetic dipoles. Scale bars are 200 nm.
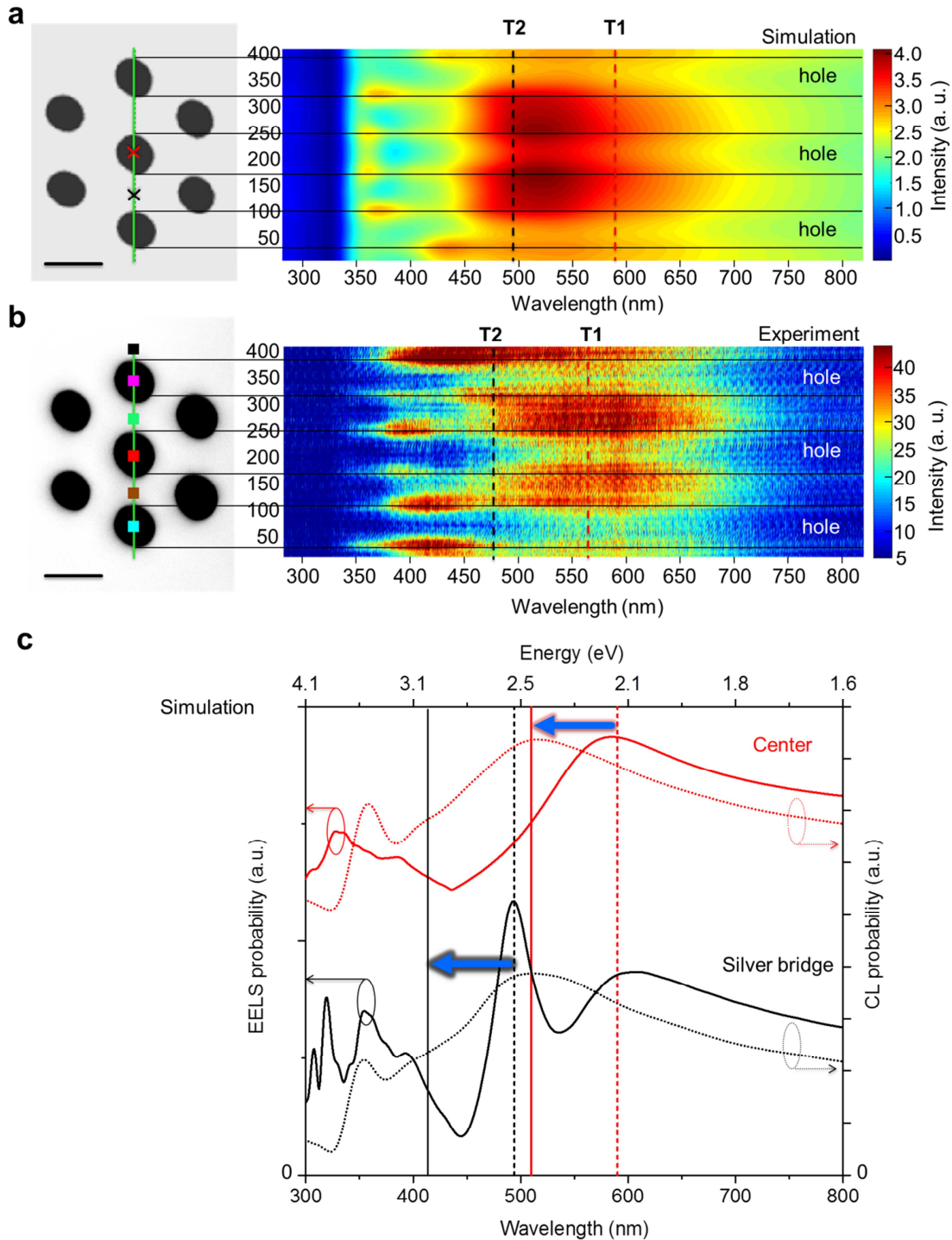
Figure 4–7. (a) Image of the simulated heptamer cavity (left) and the corresponding CL spectra along the cavity axis (green line). (b) HAADF image (left) and experimental CL spectra recorded along the green line of a fabricated heptamer nanocavity. Scale bars are 100 nm. (c) Simulated EELS and CL probabilities at the central hole and the center of silver bridge between holes, as the red and black crosses indicated in (a). Vertical dashed red and black lines mark the corresponding near-field resonances of toroidal T1 and T2 modes at (a,c) 585 and 494 nm or (b) 595 and 480 nm, respectively. The blue arrow with red edge displays the blue-shift of the T1 mode to 510 nm in the CL simulation (vertical solid red line). The blue arrow with black edge indicates the same quantity of blue-shift as the T1 mode has, and is applied on the T2 mode to 419 nm in the CL simulation (vertical solid black line).
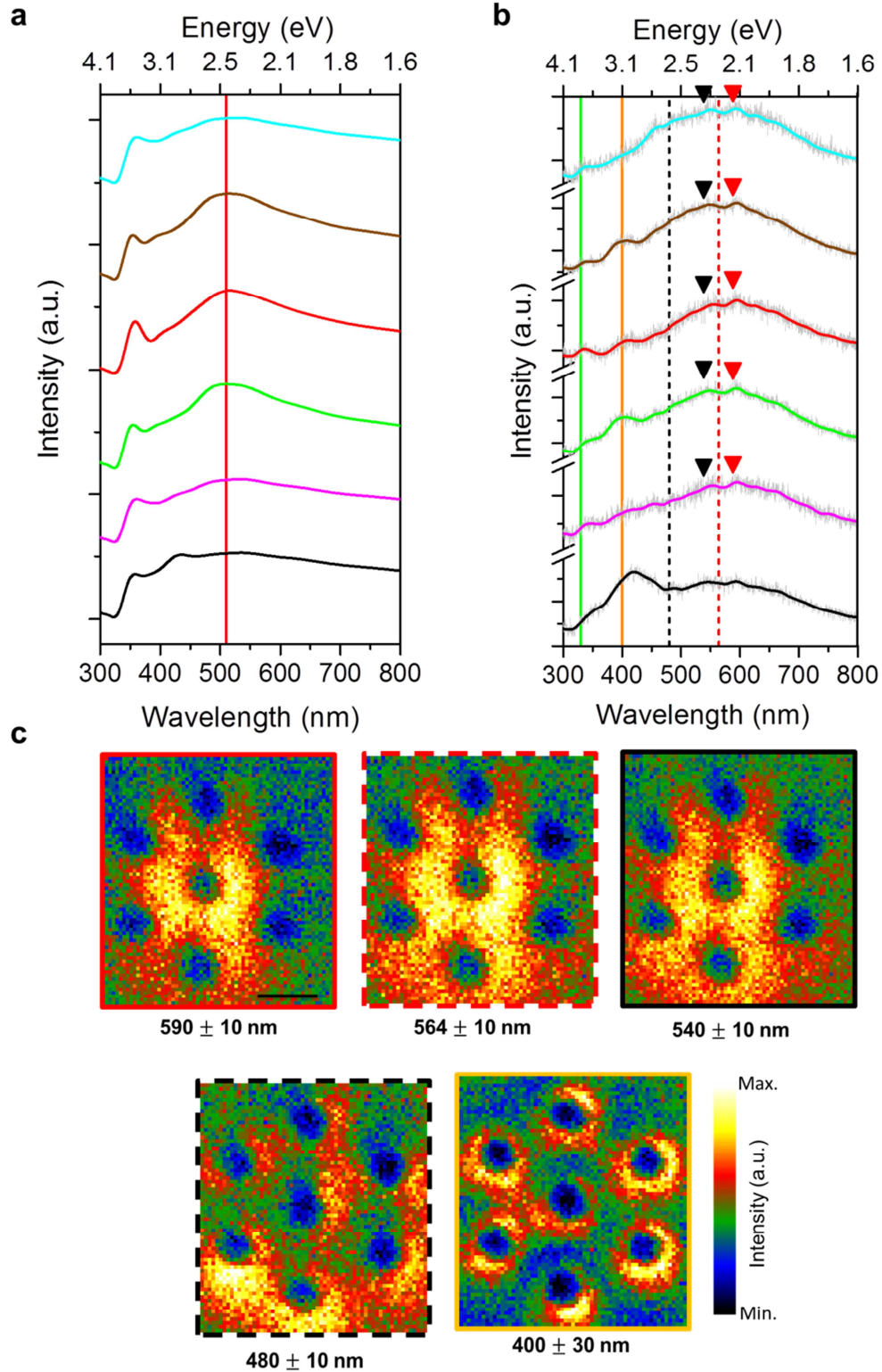
Figure 4–8. (a) Simulated and (b) experimental CL spectra extracted from the 6 color marked locations in Figure 4–7 (b). Each experimental spectrum is a sum over an area of 24×24 nm². Smoothened curves are present in front of the raw data (light grey). Vertical solid red line marks the simulated radiation peak of the T1 mode at 510 nm. Vertical dashed red and black lines correspond to the T1 and T2 modes at 595 and 480 nm, respectively. Vertical solid orange and green lines label the wavelengths of the emission at 400 nm and the silver bulk plasmon at 330 nm. Inverse black and red triangles highlight the emission peaks at 540 and 590 nm. (d) CL chromatic maps showing the spatio-spectral dispersion of the emissions at 590 $\pm$ 10 nm, 564 $\pm$ 10 nm, 540 $\pm$ 10 nm, 480 $\pm$ 10 nm, and 400 $\pm$ 30 nm.

Regarding the T2 mode, at its free-space wavelength of 480 nm, the experimental CL spectra do not show a pronounced peak, especially at the characteristic excitation positions of the T2 mode (brown and green curves in Figure 4–8 (b)). The corresponding chromatic CL map (with dashed black frame in Figure 4–8 (c)) also confirms no characteristic spatial excitation of the T2 mode in relation to its electric field E_z as shown in Figure 4–6 (b). It verifies the non-radiative character of the T2 mode.

Besides, there is an evident peak at 400 nm (vertical orange line in Figure 4–8 (b)). The corresponding chromatic CL map also is present in (c) with an orange frame. It clearly shows an excitation of a cavity mode, neither the T1 nor the T2 mode.

To summarize this part of the section, the radiation behaviors of the single toroidal moment and the antiparallel toroidal dipole pair mode were investigated experimentally by CL measurements and numerically by FDTD simulations. These toroidal modes were sustained by plasmonic heptamer nanocavities. It was the first time to experimentally observe the pronounced far-field CL signal of a single toroidal dipole moment. On the other hand, the mode consisting of an antiparallel pair of toroidal dipoles was ´dark´ (non-radiative) via CL measurements because of a net zero dipole moment.

4.4 Toroidal dipole–dipole coupling in decamer nanocavities

Atomic and molecular dipoles and their interaction with electromagnetic radiation have formed our understanding of light–matter interactions for decades. Being the most prominent family of the multipolar expansion set, their corresponding selection rules and concomitant effects in solid state systems and electrodynamics have been thoroughly investigated.[202-204] Short- and long-range coupling between dipoles manipulates the state of matter to form polar systems.[205] Additionally, higher-order electric and magnetic multipoles have been shown to contribute significantly to light–matter interaction, by increasing the photon energy,[206] or reducing the effective wavelength in materials like graphene.[207]

In addition to solid-state systems, the oscillations of conduction electrons in a metallic nanostructure may form a dipolar response, requiring that the size of the nanostructure is sufficiently smaller than the wavelength of excitation.[208] Such collective oscillations in metals are the basis for the field of nanoplasmonics.[23, 68, 69, 209-213] Moreover, multipolar coupling between adjacent nanostructures can be exploited to tailor the electromagnetic response, and to generate the macroscopic counterparts of electromagnetic induced transparency.[214, 215]

However, electric and magnetic moments are not the only possible family of multipoles. In addition to electric and magnetic multipoles which are the outcomes of the Taylor expansion of the potentials and sources, the set of toroidal multipoles has been shown from the decomposition of the electromagnetic moment tensors.[130] Dynamic toroidal multipoles are now considered as a third independent family of elementary electromagnetic sources.[170]

A toroidal dipole moment can be determined by poloidal currents flowing on the surface of a torus along the meridians,[48] leading to a loop of magnetic moments (Figure 4–9 (a)). This is a so-called magnetic toroidal moment which exhibits the peculiar character of processing odd parity under space and time inversion in contrast to electric and magnetic dipoles.[216] This behavior makes the magnetic toroidal moment distinctive from the well-known electric and magnetic moments. Such type of moment exists in materials at a wide variety, from nuclei,[132] atoms,[139] molecules[134] to solid state crystals and compounds.[144, 145, 151] For the sake of experimental feasibility, a ring of head-to-tail aligned magnetic moments can be viewed as a possible configuration for realizing a magnetic toroidal moment.

Coupling among toroidal moments is expected to form exotic new optical states, similar to the coupling of electric or magnetic dipoles tailoring the optical responses.[217] However, the fundamental toroidal dipole–dipole coupling is still open for theoretical and experimental exploration. We propose a plasmonic decamer cavity structure in silver thin films to experimentally study the coupling between toroidal dipoles. It has been demonstrated in our previous study that a magnetic toroidal dipole in the optical energy range can be excited by fast electrons in a single heptamer nanocavity.[8] As sketched out in Figure 4–9 (b), the toroidal dipolar moment is located in the central hole (green cross) and is dual to a circular head-to-tail configuration of magnetic dipoles in the outer 6 nanoholes (red arrows). Instead of creating two independent toroidal dipoles via two sets of heptamer cavities, we propose a merged structure where four nanoholes in the center are mutually shared (dashed circles). This entangled decamer cavity structure not only supports spontaneous excitation of several toroidal moments, but also creates a strong interaction between them, which serves for the purpose of strong coupling effects.

In this section, I focus on investigating the coupling between toroidal moments which are arranged in a transverse configuration. I use electron energy-loss spectroscopy in a scanning transmission electron microscope (STEM-EELS) as well as energy-filtered transmission electron microscopy (EFTEM). The

experimental work and its interpretation are further supported by finite-difference time-domain (FDTD) numerical calculations. EELS can provide a direct access to the photonic local density of states projected along the electron trajectory.[56] Toroidal moments excited in our structures contribute significantly to the EELS signal, as they support a nano-localized electric field distribution, which is polarized in the direction parallel to the electron trajectory.
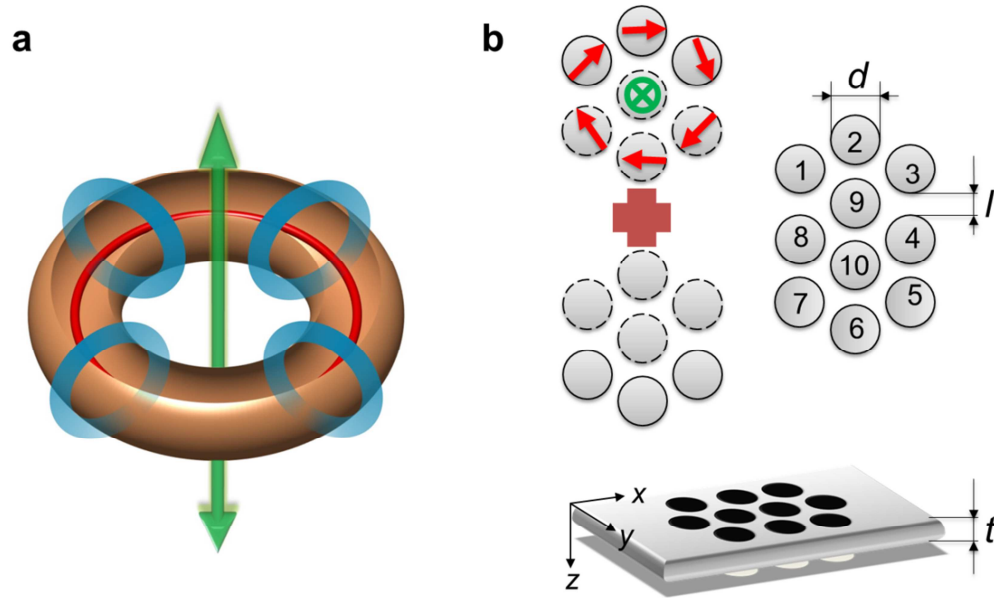
Figure 4–9. (a) Illustration of a toroidal dipole (green), consisting of poloidal currents (blue) and magnetic loops (red) along the meridians of a torus. (b) Schematic illustration for a plasmonic decamer nanocavity consisting of 10 circular nanoholes originated from two heptamer nanocavities. Red arrows and green cross represent magnetic dipoles and toroidal dipole, respectively. Circles with dash frames in the heptamer cavities mark the mutually shared holes in the designed decamer cavity. Each hole has a number index. Symbol d, l and t denote the hole diameter, the distance between two holes from rim to rim and the thickness of the silver film, respectively.

Results and Discussion

Employing a focused ion beam, I have structured plasmonic decamer nanocavities in a smooth and free-standing polycrystalline silver thin film (for details see Section 2.1.2 in Chapter 2). The fabricated decamer shown in Figure 4–10 (a) has a hole diameter d of 150 ± 10 nm and a thickness t of 67 ± 15 nm. The corresponding EEL spectra were acquired along the decamer symmetry axis in the x-direction (green line) with the electron probe perpendicularly passing through the film along the z-direction. Along the symmetric axis toroidal moments can be selectively excited, whereas other cavity modes like azimuthally polarized modes can be effectively avoided.[47] In Figure 4–10 (a), the experimental zero-loss-peak (ZLP)-subtracted EEL spectra are presented versus the electron impact location. Because of elastic scattering in the silver film, both the zero-loss intensity and the plasmon intensity vary with film thickness and, in particular, differ strongly between measurements in the hole and in the silver film. This effect can be eliminated by dividing the plasmonic signal by the ZLP intensity. I observe several resonances within the energy range from 0.6 eV to 3.8 eV. I first focus on the modes below 2.0 eV.

At energies below 2.0 eV, three significant maxima are marked by red inverse triangles and named as H1, H2 and H3, respectively (Figure 4–10 (a)). Individual EELS spectra obtained at the impact locations marked by colored circles reveal the details of the distinguished resonances (Figure 4–10 (c) left column). H1, H2 and H3 resonances appear at energies of 1.22, 1.56, and 1.75 eV, respectively (dotted lines). Furthermore, they appear at different locations along the decamer symmetry axis. The

EELS signal of the H1 mode is found at the central two holes and the silver bridge in between (exp. spectra 3–5 in Figure 4–10 (c)); mode H2 appears at the upper and lower silver bridges along the axis (exp. spectra 2 and 6 in Figure 4–10 (c)); the third mode H3 is localized on all three bridges (exp. spectra 2, 4 and 6 in Figure 4–10 (c)). These results demonstrate that fast electrons excite characteristic modes at displaying hot spots with high concentration of electromagnetic energy.

Prominent for the excitation of toroidal moments is the head-to tail arrangement of the magnetic moments in the form of a ring. However, in EELS the magnetic field is not probed as this does not change the energy of the exciting electron. To explicitly understand the experimental findings, we replicated the experimental scenario by numerical FDTD calculations of the plasmonic decamer structure in the same excitation scenario (Figure 4–10 (b)). For the simulated decamer structure we used the following parameters: hole diameter d = 100 nm, rim-to-rim distance l = 50 nm and thickness t = 50 nm. In the simulated energy–distance EEL map, three maxima of the energy-loss probability are well visible at energy losses of 1.7, 1.8 and 2.1 eV, respectively (red inverse triangles in Figure 4–10 (b)). The spatial distribution of these modes is similar to the characteristics of the experimental H1, H2 and H3 modes, but with a strong extension to the nearby nanoholes. The good correspondence between experiment and simulation is even better discernible in Figure 4–10 (c), where the simulated EEL spectra are presented alongside the experimental spectra extracted from similar locations in the corresponding structures (locations 1–6 in Figure 4–10 (a–b)). Thus I ascribe the three resonances at 1.7, 1.8, and 2.1 eV in the simulated EEL spectra to the excitation of H1, H2 and H3 modes. The simulated data are blue-shifted with respect to the experimental data, because the simulated structure had a slightly smaller size.

Now I show that the simulated magnetic field distributions of H1, H2 and H3 modes help to unveil the physics behind our observations. First, I notice that each hole sustains a magnetic dipolar moment, in a Babinet analogue to nanodiscs which support electric dipoles. Second, the orientation of the excited magnetic dipoles at each mode can be understood from the corresponding simulated z-component of the magnetic field in the decamer structure (Figure 4–11 (a)), where magnetic dipoles are outlined from the negative to the positive field amplitude in each hole. In general, each hole holds a magnetic dipole for all the modes, except for the holes 1, 3, 5 and 7 at 2.1 eV (for hole index see Figure 4–9 (b)), where the magnetic moments are slightly split into two dipoles in the case of the H3 mode. Several circles of magnetic dipoles can be distinguished for different modes in Figure 4–11 (b). For the H1 mode, head-to-tail circulating magnetic dipoles are displayed in the nanoholes 1-2-3-4-10-8 and 4-5-6-7-8-9 (red arrows), which indicates two parallel toroidal dipoles, each supported by 6 magnetic dipoles. The excited toroidal dipoles are located at the center of the holes 9 and 10 (green arrows) at a lateral distance of 252 nm. Accompanying that, the distorted magnetic loops along the holes 8-9-4-10 and 1–8 indicate the coexistence of two toroidal moments which are commonly located at the center of the structure (between holes 9 and 10). All the excited toroidal moments in the H1 modes are degenerate and parallel to each other. For the H2 mode, two circles composed of 4 magnetic dipoles are found in the nanoholes 9-3-2-1 and 10-5-6-7, indicating two antiparallel toroidal moments located at the silver bridges between the holes 2-9 and 10-6 with a distance of 504 nm. I note that, as a counterpart to mode H1, antiparallel alignment of two heptamer toroidal moments (along the holes 1-2-3-4-10-8 and 9-8-7-6-5-4) could be expected. However, this would require that the mutual nanoholes 8 and 4 hold two differently oriented magnetic dipoles spontaneously, which lead to a single moment as shown in Figure 4–11 (b). For the H3 mode, three circles of magnetic dipoles displayed in the nanoholes 1-2-3-9, 9-8-10-4 and 10-5-6-7 form three asymmetrically aligned toroidal moments located on the bridges between the holes 2-9, 9-10 and 10-6. The lateral distance between the neighboring toroidal moments for this case is approximately 252 nm. Very interestingly, the slight splitting of magnetic dipoles (in holes 1, 3, 5 and 7 at 2.1 eV) is only observed in this exotic coupling
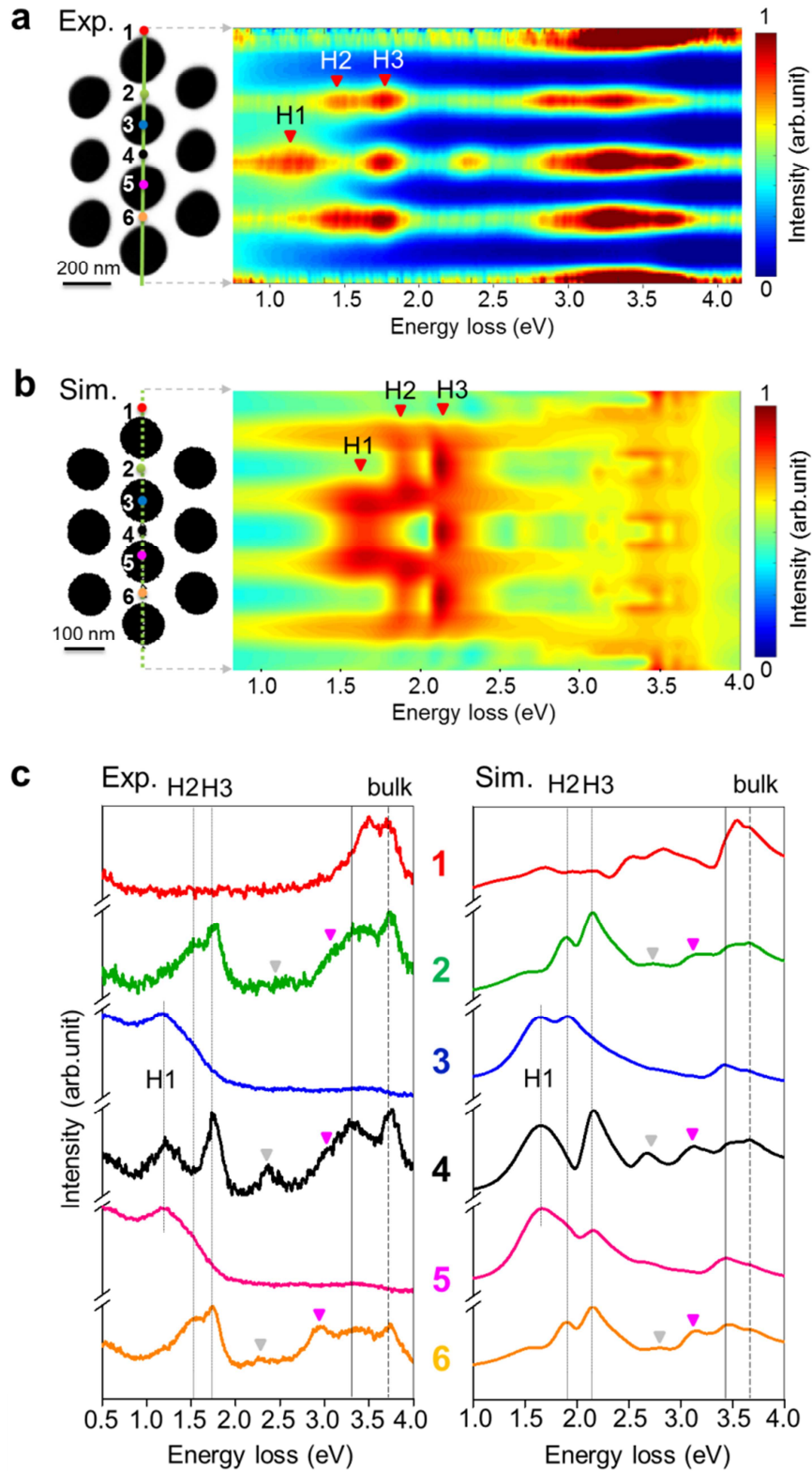
Figure 4–10. (a) HAADF image (left) and ZLP-normalized EEL spectra recorded along the green line of a fabricated decamer nanocavity. (b) Image of the simulated decamer cavity and the corresponding EEL spectra along the cavity axis (dotted green line). (c) Experimental ZLP-subtracted and simulated EEL spectra extracted from the 6 marked locations in (a) and (b), respectively. Dotted lines indicate the peak positions of the H1, H2 and H3 modes. Grey and magenta inverse triangles highlight the cavity modes. Localized surface plasmons confined between the holes are marked by a solid line just before the bulk mode (dashed line).
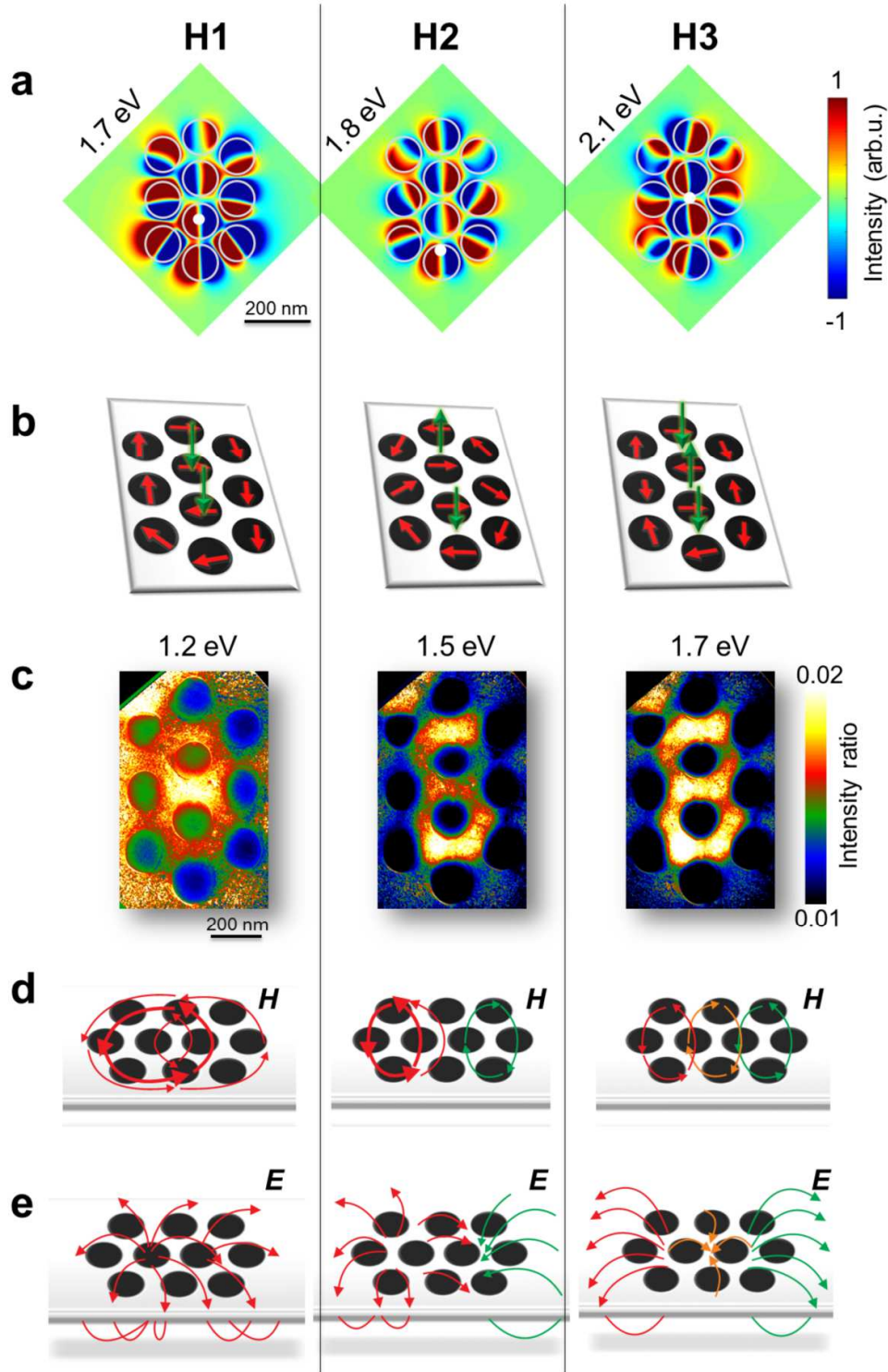
Figure 4–11. (a) Simulated magnetic fields, H_z, along the electron trajectory of the decamer structure at the H1 (1.7 eV), H2 (1.8 eV), and H3 (2.1 eV) resonances, respectively. Grey circles denote the nanoholes. The impact locations of the electron probe used for the calculation are indicated by the white dots in the corresponding figures. (b) Schematic illustration for the H1, H2 and H3 modes in the plasmonic decamer nanocavity. Red and green arrows represent magnetic and toroidal dipoles, respectively. (c) ZLP-normalized EFTEM images of the decamer nanocavity at energy losses of 1.2 ± 0.1, 1.5 ± 0.1, and 1.7 ± 0.1 eV, respectively. The black triangular areas at the upper left and right corners are beyond the acquisition area of the CCD camera. Sketches for the three-dimensional distribution of (d) magnetic and (e) electric fields at the H1, H2 and H3 resonances according to the plots of vectorial fields in Figure 4–12. Different color and thickness of the lines denote different group and relative amount of the contribution.
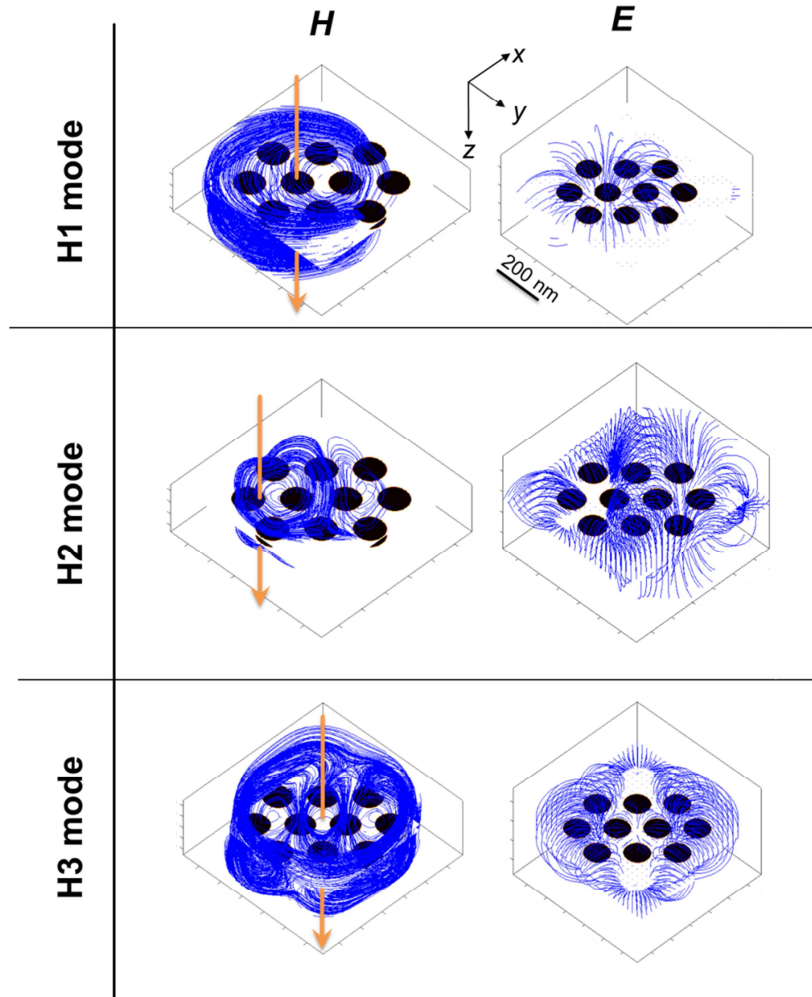
Figure 4–12. Simulated three-dimensional stream plots of the magnetic *H* and electric *E* fields of the modes H1, H2 and H3. Vertical arrows with orange color represent the impact trajectories of the electron beam. The scale bar of 200 nm applies to all the plots in *x*, *y*, *z* directions.

configuration. It is likely due to the compromise between the assisting circular connection with neighboring dipoles and keeping the system´s electromagnetic energy at a minimum. To further confirm the excitation of toroidal moments, the three-dimensional plots of both the magnetic and electric fields of the H1, H2 and H3 modes are provided in Figure 4–12. Simplified field illustrations are displayed in Figure 4–11 (d–e). It shows the essential character for toroidal moments in all the cases, i.e., the magnetic fields have loops in the *xy* plane while the electric fields loop around the magnetic flow perpendicularly. Both the magnetic and electric fields are well confined in or near the structure region. The spatial distribution features of these three modes are well captured in the ZLP-normalized EFTEM measurements (Figure 4–11 (c)), again confirming the excitation of three different toroidal modes along the axis of the decamer cavity with high electromagnetic energy concentration.

To further support the identification of toroidal moments, the decomposition of excited modes in the decamer structure can provide clear evidence which modes are exactly dominant (Figure 4–13). First, the induced current and charge density with space dependence on the structure are calculated (Figure 4–13(a)). With these, the individual moments and the corresponding far-field radiation are further computed. Please note that the radiation is calculated excluding the matter. Hence, the actual radiation should be less intense due to the absorption of the matter. The contribution of the toroidal dipole moment in the *z*-direction is significantly dominant than other moments below 2.5 eV (*T_z*, green curve

in Figure 4–13 (b) plotted on a log scale). These peaks marked by the red arrows (1.75, 2.0 and 2.2 eV) correspond to three coupled toroidal modes (1.7, 1.8, and 2.1 eV in Figure 4–10 (b)). Since EELS is a near-field measuring technique, slight energy differences are expected when compared to the far-field radiation. The plot of the modal decomposition reconfirms the excitation of pronounced toroidal moments.
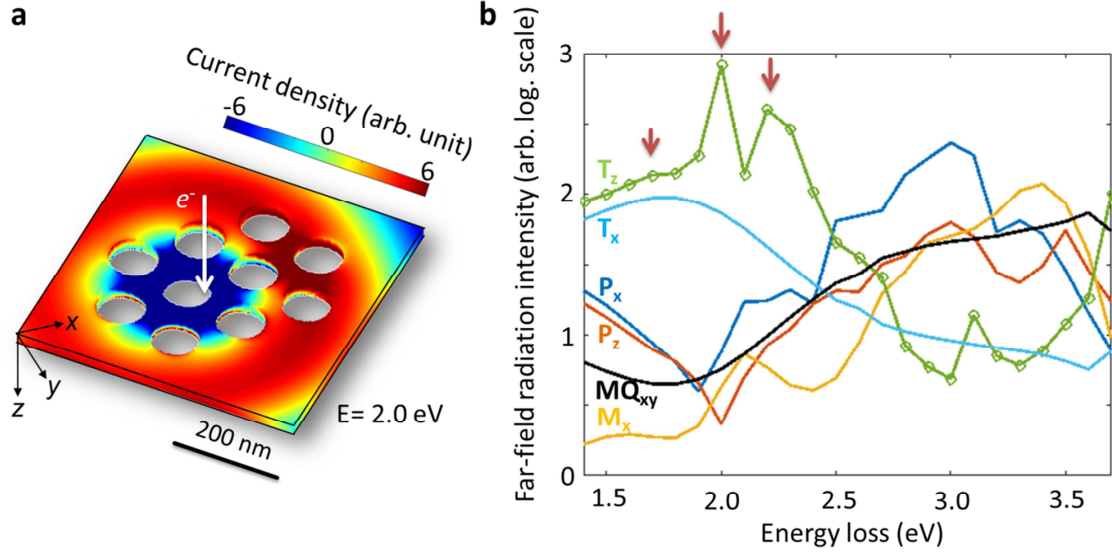
Figure 4–13. (a) Current density on the surface of the plasmonic decamer nanocavity induced by a fast electron (white arrow) at 2.0 eV. (b) Corresponding far-field radiation (scattered power) for 6 multipole moments induced in the structure. The peaks of the toroidal moment contribution Tz are marked by red arrows. Notations: P_x–electric dipole moment along x-axis; P_z–electric dipole moment along z-axis; M_x–magnetic dipole moment along x-axis; T_z– toroidal dipole moment along z-axis; T_x– toroidal dipole moment along x-axis; MQ_{xy}–magnetic quadrupole moment in x-y plane. The coordinate system shown in (a) is used for the computation of the model decomposition.

So far, we have understood that multiple toroidal dipoles consisting of 4, 6 or 8 magnetic dipoles were spontaneously excited in the designed decamer structure at 1.22, 1.56, and 1.7 eV. The excited toroidal dipoles are transversely aligned either parallel (mode H1) or antiparallel (modes H2 and H3). The ascending energies of the observed modes H1, H2, and H3 (Figure 4–14 (a)) indicate a coupling effect between the excited toroidal moments with a lower interaction energy for parallel alignment rather than for antiparallel alignment.

To understand and clarify the associated coupling phenomena, we outline a simple theoretical model. The interaction between two toroidal moments takes place through the external conduction and displacement currents, which are equivalent to a vortex of the magnetic field.[129] In the case of two point-like toroidal dipoles in free space, the external conduction current is therefore zero and the displacement current is related to the electric field by $\vec{D} = \varepsilon_0 \vec{E}$, i.e., the electric field associated to one toroidal moment is acting on the second toroidal moment. The electromagnetic field attributed to an oscillating toroidal moment has been derived elsewhere.[122] In free space, the interaction energy between two transversely coupled toroidal moments is given by

$$W^{int.} = (\vec{T}_1 \cdot \vec{T}_2)\left[\left(\frac{\omega}{c}\right) \cdot \frac{1}{r^3} - \left(\frac{\omega}{c}\right)^3 \cdot \frac{1}{r}\right], \tag{4.4}$$

where r is the center-to-center distance between two toroidal dipoles (inset in Figure 4–14 (a)).[130] Equation ((4.4) demonstrates the coexistence of two types of electromagnetic interaction, which in

general are associated to the near-field and far-field contributions, with r^{-3} and r^{-1} dependences, respectively. Assuming that both toroidal moments have identical energies, the calculated interaction energy for parallel or antiparallel schemes is plotted as a function of distance r and the energy of the single toroidal moment in Figure 4–14 (c and d), respectively. Surprisingly, the toroidal dipoles can still interact at separations of several hundreds of nanometers. I note from equation (4.4) that the interaction energy flips sign when the separation crosses a critical distance of $r_c = c/\omega$, which is a result of the competition between the near-field and far-field terms. This means that along a certain energy–distance line the near- and far-field terms cancel each other. Within the energy range of 1 to 2.2 eV, the critical distance r_c is generally smaller than 200 nm. Above that, in the long-distance regime ($r > r_c$), the interaction energy for parallel coupling is negative in contrary to the positive interaction energy for the case of antiparallel coupling. We briefly notify here that the transfer of the electromagnetic energy seems to be facilitated via the vacuum region; otherwise the effective refractive index of the surface plasmons inside the silver would shorten the critical radius to only a few nanometers.
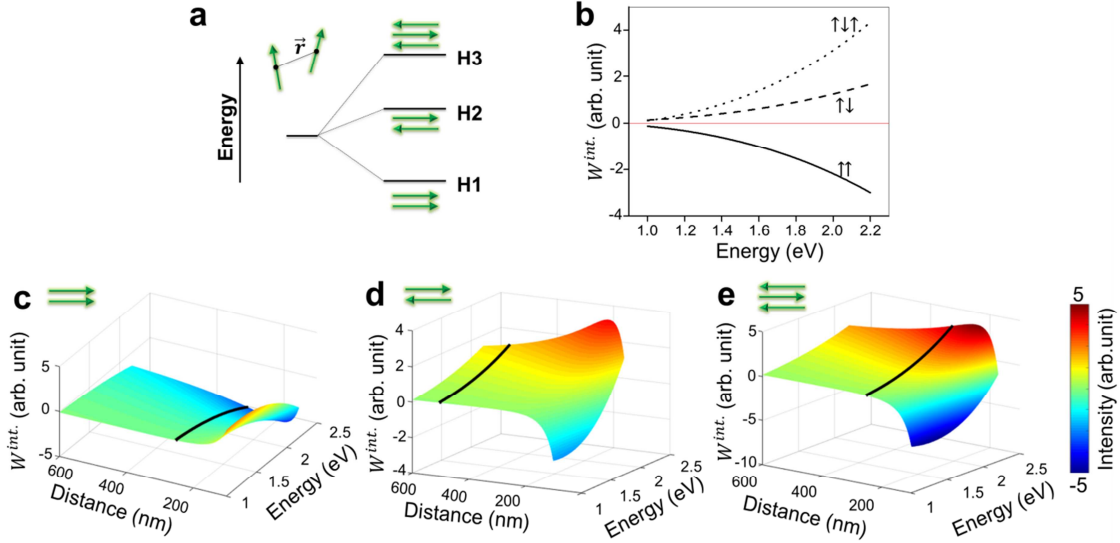
Figure 4–14. (a) Energy level scheme of the experimental H1, H2 and H3 modes. Green arrows denote toroidal dipoles. The inset shows two coupled toroidal dipoles with a center-to-center distance r. (c–e) Interaction energies of two parallel aligned, two anti-parallel aligned, and three anti-parallel aligned toroidal dipoles as a function of the single toroidal moment energy and the dipole distance r, respectively. Same color codes are applied to (c–e) to make them comparable. Black curves in (c–e) specify the interaction energy at dipole distances of 252 nm, (c, e) and 504 nm (d). A comparison of the interaction energies specified by these black curves is present in (b), where a horizontal red line denotes the interaction energy at zero.

When three identical toroidal dipole moments T_1, T_2 and T_3 couple with each other at a certain lateral distance r, the total interaction energy follows

$$W_{\uparrow\downarrow\uparrow}^{int.} = W_{T_1,T_2}^{int.}(r) + W_{T_2,T_3}^{int.}(r) + W_{T_1,T_3}^{int.}(2r). \tag{4.5}$$

The corresponding plot of interaction energy is shown in Figure 4–14 (e), which exhibits a similar behavior as for the interaction energy of two antiparallel coupled toroidal moments, yet with larger amplitude.

The above mentioned first principles describe the energy trends of the modes H1, H2 and H3. For the mode H1, the two initial toroidal moments have a distance of 252 nm (center-to-center distance

between the holes 9 and 10). The corresponding parallel coupling energy at this distance is highlighted in Figure 4–14 (c) by the black curve and replotted in Figure 4–14 (b) (also black curve) for clarification. The two antiparallel toroidal moments of the mode H2 have a separation of 504 nm (distance between location 2 and 6 in Figure 4–10 (a)). The corresponding interaction energy is highlighted (black curve in Figure 4–14 (d)) and replotted as dashed line in Figure 4–14 (b). Finally, the excited toroidal moments of the mode H3 are separated by 252 nm. The corresponding interaction energy is marked as a black curve in Figure 4–14 (e) and replotted as a dotted line in Figure 4–14 (b). For the energy landscapes of the toroidal moments situated between 1 and 2.2 eV, the interaction energies calculated from different coupling configurations clearly reveal that parallel coupling lowers the entire energy of the structure, whereas antiparallel coupling raises the entire energy. Moreover, antiparallel coupling of the triple toroidal moment H3 has a larger interaction energy than that of the double antiparallel coupled toroidal moment H2. This difference becomes even more pronounced when increasing the single toroidal energy (Figure 4–14 (b)). These results fit very well with the experimentally observed energy tendencies of the modes H1, H2 and H3.

Although theoretical calculations show that the long-range interaction between toroidal moments is relatively weak (Figure 4–14 (c–e)), the long-range coupling effect observed in the experiments is rather pronounced. In theory, electromagnetic sources are considered as point sources. What we see from our experiments is that the toroidal modes are extended over hundreds of nanometer. Hence, they can couple to each other. In addition, the coupling is further enhanced by retardation, which is described by the dynamic nature of toroidal moments.
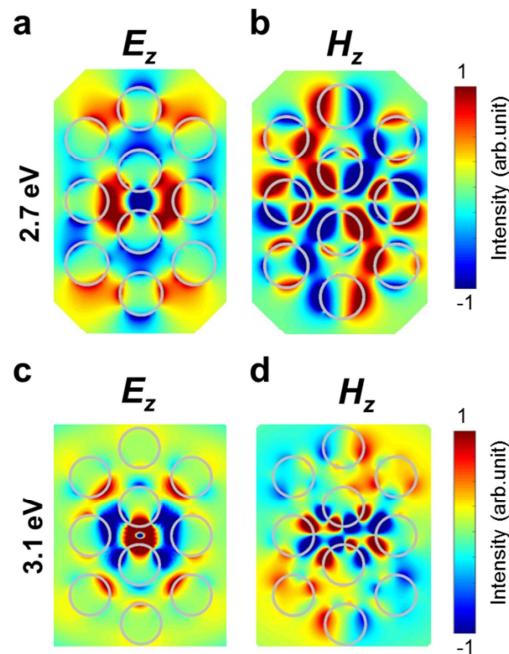
Figure 4–15. Electric and magnetic field presentation projected along the *z*-direction in the *xy* plane of the resonances at (a,b) 2.7 eV and (c,d) 3.1 eV, respectively. The diameter of the hole is 100 nm. Grey circles denote the locations of the nanoholes.

Apart from these three coupled toroidal moments, we observe an additional resonance at 2.4 eV (grey inverse triangle in Figure 4–10 (c) left column). This feature was also found in the simulated electron energy-loss spectra at 2.7 eV (right column in Figure 4–10 (c)). By analyzing the corresponding magnetic field (Figure 4–15 (a)), I find that at this resonance energy both magnetic dipoles and

quadrupoles (hole 2 and 6) are simultaneously excited in the nanoholes. Even more, the magnetic flow displayed in three-dimensional space (Figure 4–16 (a)) shows that the corresponding magnetic loops extrude out of the *xy* plane, which is significantly different from the aforementioned hybridized toroidal modes. The configuration of the corresponding electric field is relatively simple. As shown in Figure 4–15 (a), it indicates a flipping of the longitudinal polarization along the *x*-axis.[47]
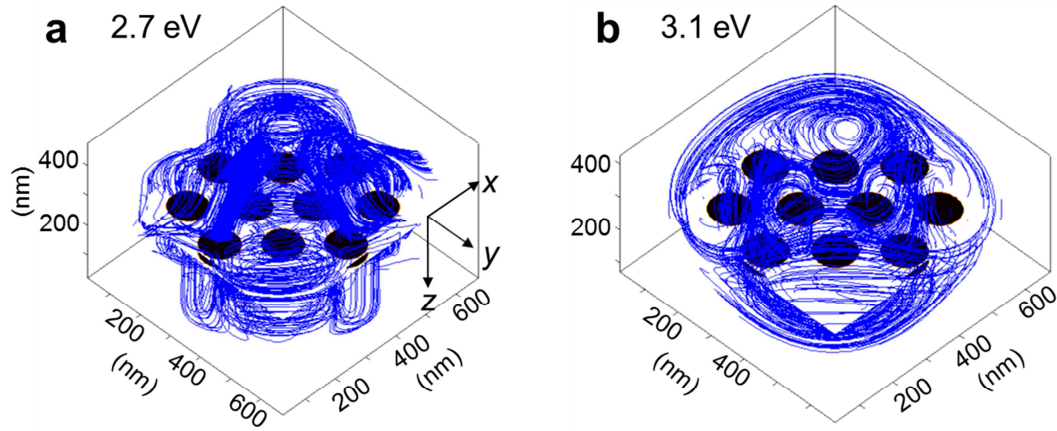
Figure 4–16. Simulated three-dimensional stream plots of the magnetic fields *H* at (a) 2.7 and (b) 3.1 eV, respectively. The electron position is at the center of the structure.

In addition, there is a resonance at a higher energy of 2.9 eV in the experimental EEL spectra, which corresponds to the double peak around 3.1 eV in the simulated EEL spectrum (magenta inverse triangles in Figure 4–10 (c)). The corresponding electric-field distribution (Figure 4–15 (c)) indicates radial polarization from the center of the decamer structure, while the magnetic field (Figure 4–15 (d)) displays the coexistence of both a magnetic quadrupole and a hexapole (three-dimensional magnetic flow in Figure 4–16 (b)). This configuration is associated with an electric radial cavity mode. The imperfect structure in the fabricated decamer cavity results in a slight energy shift along the axis.
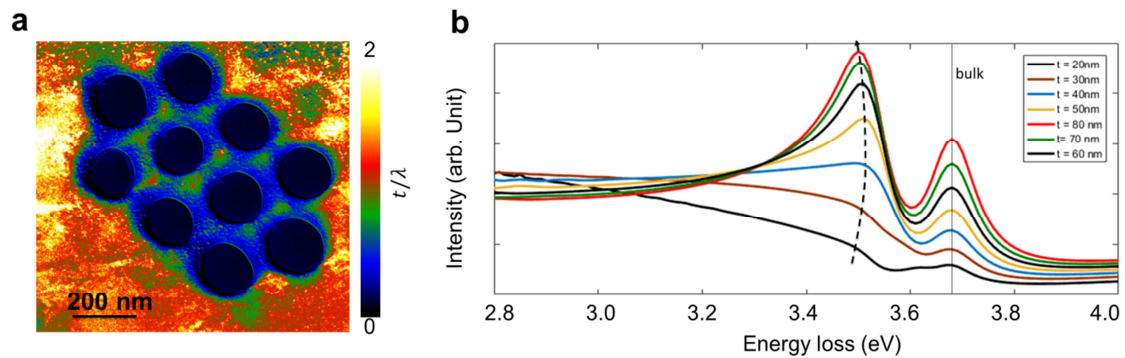
Figure 4–17. (a) Thickness map of the plasmonic decamer cavity structure shown in Figure 4–10 (a). (b) Simulated EEL spectra of infinite silver thin films with thicknesses from 20 to 80 nm at a step of 10 nm. The black dashed line indicates the energy shift of the surface plasmon polariton mode (slab mode) at about 3.5 eV. The black solid line shows the location of silver bulk plasmon.

Close to the bulk plasmon energy at 3.8 eV, there is another spectral feature at around 3.4 eV resolved in both the simulated and experimental EEL spectra, as indicated by the black solid line in Figure 4–10 (c). The energy range is typical for surface plasmon polariton excitation on infinite silver thin films (slab mode, Figure 4–17 (b)). However, the energy shifts when the film morphology changes. The observed peaks are probably due to the excitation of a localized surface mode, in which a small energy shift can be seen between the spectra extracted from the location 1 (outside the structure) and the locations inside the structure (Figure 4–10). Meanwhile, the thickness variations of the fabricated structure also have an effect on the energy and the width of the corresponding EELS signals (Figure 4–17 (b)). The thickness map of the investigated decamer cavity structure (Figure 4–10 (a)) is shown in Figure 4–17 (a). The thickness between the nanoholes is approximately constant, which is 67 nm calculated from 0.8 t/λ with the mean free path $\lambda = 83.8$ nm. However, the thickness varies slightly along the decamer long axis by about 16 nm.

Additionally, I present the experimental EELS results of another plasmonic decamer structure in Figure 4–18. Three resonances at 1.23, 1.56 and 1.82 eV are pronounced and well visible (vertical dashed lines in Figure 4–18 (b)). Moreover, the locations of these modes fit very well with the characteristic locations of the hybridized modes H1, H2 and H3, which indicates the reproducibility of the toroidal moment coupling phenomena in plasmonic decamer cavities.
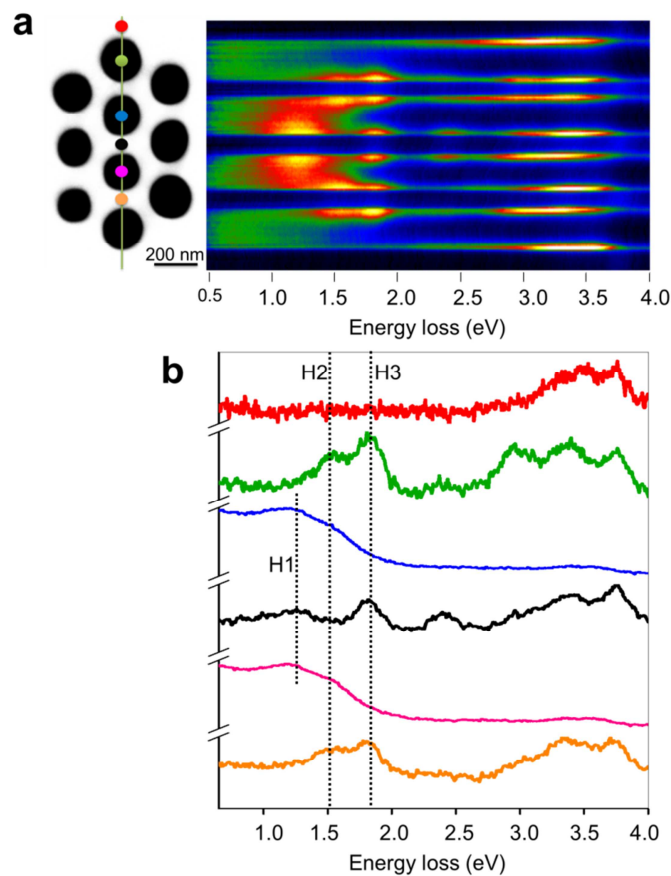
Figure 4–18. (a) HAADF image and spectroscopy of a fabricated decamer nanocavity. The experimental ZLP-subtracted EEL spectra are plotted as a function of impact location along the long axis of the cavity (green line). (b) Experimental ZLP-subtracted EEL spectra extracted from the 6 color marked locations in (a). Dotted lines indicate the peaks of the modes H1, H2 and H3.

In summary, we have designed and demonstrated the coupling of toroidal dipole moments in plasmonic decamer nanocavities by EELS, EFTEM and FDTD numerical calculations. Several toroidal dipole moments comprised of different numbers of magnetic dipoles were excited at optical frequencies. They couple transversely and give rise to three hybridized modes. The coupling effect of toroidal moments is remarkably pronounced and even observable at a separation of hundreds of nanometers. Based on the simulation of a decamer cavity structure, we have seen single magnetic dipole excitations partially splitting into two individual dipoles in order to facilitate complex hybridization of toroidal moments in such an entangled structure.

The energy of the hybridized modes increases while increasing the number of antiparallel aligned toroidal moments. These experimental findings can be well explained by calculations of the interaction energy; in the long-range regime ($r > r_c$), the antisymmetric mode possesses a positive contribution from the interaction energy, whereas the symmetric mode yields a negative contribution from the interaction energy. Indeed, the long-range interaction of spin-based toroidal moments in solid-state systems has led to the emergence of new ordering in materials, i.e., the so-called toroidization effect. Here, the dynamic counterpart of toroidal interactions which we have investigated described in this work would be the cornerstone for the development of metamaterial-based toroidization. The dominant coupling effect between toroidal dipole moments, as a prototype or a constituent element, paves the way for further research and exploitation in the fields of nanooptics and metadevices, for example, designing metafaces with novel optical properties or low-loss planar waveguides by virtue of transverse toroidal moment coupling.

4.5 Conclusions

Toroidal multipoles were systematically described by Ginzburg, Dubovik and Tugushev in the former Soviet Union (Section 4.2) as early as in 1980s. A dynamic toroidal dipole moment can be derived from a Taylor expansion of charge and current densities in the form of

$$\vec{T} = \frac{1}{10c} \int [\vec{r}(\vec{r} \cdot \vec{J}(\vec{r}, t)) - 2r^2\vec{J}(\vec{r}, t)]d^3r$$

One type of the toroidal multipole family is the magnetic toroidal multipole. The magnetic toroidal dipole is of the lowest order, which can equivalently be constructed by a closed circle of elementary magnets with head-to-tail connection. It exhibits the peculiar character of processing odd parity under space and time inversion in contrast to electric and magnetic dipoles.The fascinating characteristics have been drawing increasing research interest in the fields of solid-state physics and electrodynamics, with application potentials in data storage, ultrasensitive sensors, and lasing.

There is plenty of new territory to be explored in the field of toroidal moments. To enrich the understanding of dynamic toroidal moments, I focused on exploring the far-field properties and the coupling effects of magnetic toroidal moments both experimentally and theoretically by means of EELS, CL and FDTD simulations.

In Section 4.3, the near-field EELS measurements and the corresponding simulations revealed the excitation of both a single toroidal dipole mode and an antiparallel pair of toroidal dipoles on a plasmonic heptamer nanocavity. Interestingly, the single toroidal dipole mode showed a pronounced far-field radiation signal with little damping in the CL measurements. In contrast, the antiparallel pair toroidal dipole mode hardly coupled to the far-field radiation due to the net dipole moment. To the

best of my knowledge, it was the first experimental report on the far-field radiation of a single toroidal moment, which confirmed the new understanding of radiative behavior of single toroidal dipoles.

In Section 4.4, the transverse coupling of several toroidal dipole moments at optical frequencies have been demonstrated in plasmonic decamer nanocavities by EELS, EFTEM, and FDTD numerical calculations. The coupling led to three pronounced hybridized modes, whose energy increased as the number of antiparallel aligned toroidal moments increased. The underlying mechanism was that the antisymmetric alignment contributed positively to the interaction energy, whereas the symmetric alignment contributed negatively to the interaction energy in the long-range regime.

Contributions to this chapter:

Section 4.2 has been adopted partially from the published article ref. [130]. The adopted parts were written by Surong Guo with contributions of Nahid Talebi (MPI-FKF). Section 4.4 has been published in ref. [218], which was written by Surong Guo with contributions of Nahid Talebi (MPI-FKF). Surong Guo prepared the samples, conducted the experiments, and analyzed the data. Nahid Talebi (MPI-FKF) performed the numerical calculations. The project was supervised by Nahid Talebi (MPI-FKF) and Peter A. van Aken (MPI-FKF). The idea was conceived by Nahid Talebi (MPI-FKF).

Chapter 5   Conclusions and outlook

The core of this thesis is to characterize and study plasmon-associated phenomena and physics on the nanoscale in the fields of nano-optics, metamaterials, and fundamental electrodynamics. For this purpose, characterization techniques, particularly with high spatial resolution, are employed to fulfill diverse tasks in the framework of relativistic (fast) electron excitation. EFTEM has been applied for mapping the spatial distribution of excited plasmonic modes by forming high-resolution images with specific energy-loss electrons; STEM-EELS has been applied especially for measuring the dedicated spectral response of excited plasmonic modes in an ultrabroad spectral range via counting the energy losses of the primary electrons; STEM-CL gives access to exclusively detect the radiative components of the excited plasmonic modes. Besides the experimental methods, numerical FDTD calculations based on Maxwell´s equations reveal the underlying physics and dynamics of relativistic electron–plasmon interaction, near- and far-field scattering, and induced field polarization.

The focuses of the thesis are (i) mapping the plasmonic modes of three-dimensional gold tapers close to the apex by EELS and EFTEM with high spatial and spectral resolution, (ii) the resonant interaction mechanism between fast electrons and the surface plasmonic modes of gold tapers, (iii) the corresponding radiation behavior of surface plasmons on gold tapers, (iv) the peculiar character of toroidal multipoles, (v) the radiation behavior of toroidal dipole moments in a plasmonic heptamer nanocavity, and (vi) the fundamental dipole–dipole coupling in the toroidal multipole family.

In chapter 1, I have briefly introduced that the oscillations of conduction electrons of metals (plasmons) have the capacity of guiding and concentrating electromagnetic field on the nanoscale. This boosts the study of light–matter interaction in many fields and has large potentials for applications. In this thesis, several high-resolution methods, namely EELS, EFTEM and CL, have been employed to characterize plasmons on the nanoscale. All these advanced techniques make use of relativistic electrons as excitation sources. The near-field of a fast electron has a broad distribution of frequencies and plane-wave momenta and decays exponentially from the point of the electron. This electron near-field excites plasmons through Coulomb interaction in the energy- and momentum-conservation picture. Fast electrons suffer energy losses due to the work done by the Lorentz force of the total plasmon scattered field. Furthermore, the excited plasmonic modes can also couple to radiation in a coherent way. The above are the fundamentals to interpret the sequential experimental results.

In chapter 2, all sample preparation procedures, experimental techniques, and data processing methods that were used in this research thesis, were explained. Electropolishing, FIB and ion milling were used for fabricating plasmonic nanocavities on the nano-scale. EFTEM, STEM–EELS, and STEM–CL were employed to characterize plasmons with a focus on visualization with high spatial sampling, broadband detection with high spectral sampling, and the radiation properties, respectively. Data processing was applied according to the need with the aim of extracting the correct plasmon signals and rendering them in a clearer way.

These powerful tools recently have a fast development, which allow us to explore more fingerprints of plasmons. For example, the energy resolution of EELS has reached values as small as a few meV,[219] which gives access to study phonon properties and should be useful for understanding the phonon–phonon, phonon–plasmon, and phonon–photon coupling.[220] The ultrafast EELS equipped with a pulsed electron beam enables the study of the dynamics of plasmons in the femto-second regime. The angular-momentum-resolved CL is helpful to investigate the propagation behavior of surface plasmon polaritons by measuring the dispersion relation of the corresponding coherent radiation. These

fascinating developments in the relevant methodology will benefit the current projects, as explained below in the corresponding parts.

In chapter 3, the plasmonic properties of three-dimensional gold tapers in the apex proximity and the interaction mechanism with fast electrons were investigated. Distinct resonances along the taper shaft were explicitly resolved by EELS. However, the underlying physics of these resonant modes involved two different dynamic mechanisms, reflection and phase-matching, whose relation was disentangled by systematically studying the plasmonic modes of gold tapers with various opening angles from 5° to 47° by means of EELS and FDTD numerical calculations. The interaction mechanism is essentially determined by the interaction length between the scattered field of the excited plasmons and the field of a fast electron along the electron trajectory. For small taper cross-sections (radius $\leq$ 50 nm), the fundamental plasmon mode with zeroth-order azimuthal angular momentum ($M = 0$) was excited and travelled to the taper apex. The reflection of the $M = 0$ mode thus interfered with itself, which caused resonant signals in EEL spectra. For larger taper cross-sections, plasmonic modes with higher-orders were excited due to the larger local radius. Meanwhile, with increasing interaction length, the scattered plasmonic field picked up the phase of the exciting electron along the trajectory, resulting in a phase-matching resonant condition. These two coexisting mechanisms competed with each other during transition. In general, for gold tapers with large opening angles (above ~20°), phase matching is the dominant contribution to the electron energy-loss because of the increasing interaction length between the electron and the taper near-field. In contrast, reflection from the taper apex dominates the EELS contrast in gold tapers with small opening angles (below ~10°). For intermediate opening angles, a gradual transition of these two mechanisms was observed. The results serve for designing gold tapers with the desired plasmonic properties.

Also, the far-field radiation of gold tapers with 13° and 47° opening angles under electron excitation were investigated by means of CL. A significant radiation between 500 and 700 nm was observed when the electrons excited the area behind the taper apex regardless of the opening angles. It showed that the radiative decay of surface plasmons on gold tapers was the major contribution as compared to transition radiation and photoluminescence. Moreover, reflection of plasmonic modes plays a role on the emission at the apex; the modes that were excited at the apex of the 13° taper were prone to be guided away from the apex rather than coupled to the far-field radiation. In contrast, stronger radiation at the apex was observed in the case of 47° taper, mostly due to the lack of adiabatic guidance.

Further interesting aspects for future studies are: (i) to experimentally investigate the fundamental $M = 0$ mode in a lower energy range (< 0.5 eV), complementarty to the already investigated higher-order modes. It should be useful to understand the spectral evolution of the fundamental mode. It requires an electron probe with a narrower energy resolution in EEL spectroscopy, which is commercially available; (ii) in a modified structural system with a sphere attached at the end of taper apex, to investigate the dependence of plasmonic resonances on the parameter of the attached spheres; (iii) to facilitate the nanofocusing capabilities of gold tapers via modification of the geometry, for example, designing an interface for coupling azimuthally rotating higher-order modes to longitudinally propagating edge modes; (iv) to employ angular-momentum-resolved CL to incorporate the momentum-dependent plasmon-mediated photoemission; (v) experimentally investigate the dynamics of the plasmonic modes, especially at taper apices as nanoantennas, when ultrafast time-resolved EELS in lower energy-loss regime is available.

In chapter 4, a brief introduction to toroidal multipoles was presented, including the discovery and derivation from multipole expansion sets, the near-field and parity characteristics, the associated research fields of both static and dynamic toroidal moments, and their applications. Toroidal moments were early considered as ´dark´ modes, because of no evident detection via far-field

microscopy; later it was predicted theoretically that the far-field radiation pattern of a toroidal dipole should have an identical pattern as an electric dipole. As a proof-of-principle experiment, we used STEM-CL to detect the radiation of a toroidal dipole moment sustained by a plasmonic heptamer nanocavity on the nanoscale. The EELS results showed that two toroidal modes were supported in such a structure, one consisting of a single toroidal dipole moment and another mode with two antiparallel toroidal dipoles. The corresponding CL results demonstrated a pronounced far-field radiation of the single toroidal dipole moment, whereas the antiparallel toroidal dipole mode was ´dark´ due to the net zero dipole moment. It was clearly shown that the single toroidal dipole coupled to the far-field.

Furthermore, the fundamental dipole–dipole coupling among toroidal moments was investigated both experimentally and theoretically. It was demonstrated for the first time by EELS and EFTEM that the pronounced toroidal dipole–dipole coupling in a plasmonic nanocavity. The statements were strongly supported by numerical FDTD calculations. The results showed that the toroidal dipoles coupled to each other even at a separation of more than hundred nanometers. The parallel and antiparallel alignments between them gave rise to hybridized modes with different interaction energies. The coupling was through reorientation of the head-to-tail vortices composed of localized magnetic dipoles at nanoholes. The electrodynamic retardation effect was supposed to further facilitate the coupling at a few nanometers. This work further enhances the understanding of fundamental electromagnetic phenomena in the third set of electromagnetic sources, and paves the way for further research and exploitation in the fields of metamaterials, and light–matter interaction.

A deeper and interesting extension of this project can be: (i) investigating the vertical toroidal dipole–dipole coupling by fabricating two vertically aligned plasmonic heptamer nanocavities with a dielectric separation layer, and (ii) focusing on the dependency between the geometry parameters and the toroidal moment response, such as hole diameter, hole–hole distance and slab thickness.

Hereby I declare that this thesis titled, "Characterization of Surface Plasmons and Toroidal Moments Using Relativisitc Electrons" has been independently carried out by me at the Stuttgart Center for Electron Microscopy (StEM), Max Planck Institute for Solid State Research in partial fulfillment of the requirements for the degree of Doctor of Natural Science (Dr. rer. nat.) in Materials Science from the Technical University of Darmstadt (TU Darmstadt). I certify that the work presented in this thesis is, to the best of my knowledge and belief, original and contains no material previously published or written by another person, except where due reference and permission is made.

Stuttgart
28.06.2018

Surong Guo

References

1.   Nelayah, J.; Kociak, M.; Stéphan, O.; Garcia de Abajo, F. J.; Tence, M.; Henrard, L.; Taverna, D.; Pastoriza-Santos, I.; Liz-Marzan, L. M.; Colliex, C. Mapping surface plasmons on a single metallic nanoparticle. *Nature Physics* **2007**, *3*, 348–353.

2.   Bosman, M.; Keast, V. J.; Watanabe, M.; Maaroof, A. I.; B. Cortie, M. Mapping surface plasmons at the nanometre scale with an electron beam. *Nanotechnology* **2007**, *18*, 165505.

3.   Kociak, M.; Stéphan, O. Mapping plasmons at the nanometer scale in an electron microscope. *Chemical Society Reviews* **2014**, *43*, 3865–3883.

4.   Hohenester, U., Plasmon excitation by fast electrons. In *World Scientific Handbook of Metamaterials and Plasmonics*, World Scientific: 2017; pp 339–377.

5.   Kociak, M.; Zagonel, L. F. Cathodoluminescence in the scanning transmission electron microscope. *Ultramicroscopy* **2017**, *174*, 50–69.

6.   Kapetanakis, M. D.; Zhou, W.; Oxley, M. P.; Lee, J.; Prange, M. P.; Pennycook, S. J.; Idrobo, J. C.; Pantelides, S. T. Low-loss electron energy loss spectroscopy: an atomic-resolution complement to optical spectroscopies and application to graphene. *Physical Review B* **2015**, *92*, 125147.

7.   Egerton, R. F., Electron energy-loss spectroscopy in the electron microscope. 3 ed.; Springer US: 2011.

8.   Ögüt, B.; Talebi, N.; Vogelgesang, R.; Sigle, W.; van Aken, P. A. Toroidal plasmonic eigenmodes in oligomer nanocavities for the visible. *Nano Letters* **2012**, *12*, 5239–5244.

9.   Ruthemann, G. Discrete energy loss of fast electrons in solid bodies. *Naturwissenschaften* **1941**, *29*, 648–648.

10.   Bohm, D.; Pines, D. A collective description of electron interactions: III. Coulomb interactions in a degenerate electron gas. *Physical Review* **1953**, *92*, 609–625.

11.   Powell, C. J.; Swan, J. B. Origin of the characteristic electron energy losses in aluminum. *Physical Review* **1959**, *115*, 869–875.

12.   Ritchie, R. H. Plasma losses by fast electrons in thin films. *Physical Review* **1957**, *106*, 874–881.

13.   Nelayah, J.; Gu, L.; Sigle, W.; Koch, C. T.; Pastoriza-Santos, L.; Liz-Marzan, L. M.; van Aken, P. A. In *Low-loss-energy EFTEM imaging of triangular silver nanoparticles*, Berlin, Heidelberg, Springer Berlin Heidelberg: Berlin, Heidelberg, 2008; pp 243–244.

14.   Sigle, W.; Nelayah, J.; Koch, C. T.; van Aken, P. A. Electron energy losses in Ag nanoholes—from localized surface plasmon resonances to rings of fire. *Optics Letters* **2009**, *34*, 2150–2152.

15.   Yamamoto, N.; Araya, K.; García de Abajo, F. J. Photon emission from silver particles induced by a high-energy electron beam. *Physical Review B* **2001**, *64*, 205419.

16.   Vesseur, E. J. R.; de Waele, R.; Kuttge, M.; Polman, A. Direct observation of plasmonic modes in Au nanowires using high-resolution cathodoluminescence spectroscopy. *Nano Letters* **2007**, *7*, 2843–2846.

17.   Losquin, A.; Zagonel, L. F.; Myroshnychenko, V.; Rodríguez-González, B.; Tencé, M.; Scarabelli, L.; Förstner, J.; Liz-Marzán, L. M.; García de Abajo, F. J.; Stéphan, O.; Kociak, M. Unveiling nanometer scale extinction and scattering phenomena through combined electron energy loss spectroscopy and cathodoluminescence measurements. *Nano Letters* **2015**, *15*, 1229–1237.

18.   Yamamoto, N. Development of high-resolution cathodoluminescence system for STEM and application to plasmonic nanostructures. *Microscopy* **2016**, *65*, 282–295.

19.   Coenen, T.; Haegel, N. M. Cathodoluminescence for the 21st century: Learning more from light. *Applied Physics Reviews* **2017**, *4*, 031103.

20.   Losquin, A.; Kociak, M. Link between cathodoluminescence and electron energy loss spectroscopy and the radiative and full electromagnetic local density of states. *ACS Photonics* **2015**, *2*, 1619–1627.

21.   Browning, N. D.; Arslan, I.; Erni, R.; Reed, B. W., Low-Loss EELS in the STEM. In *Scanning Transmission Electron Microscopy: Imaging and Analysis*, Pennycook, S. J.; Nellist, P. D., Eds. Springer New York: New York, NY, 2011; pp 659–688.

22.   Stockman, M. I., Nanoplasmonics fundamentals and surface-enhanced Raman scattering as a physical phenomenon. In *Recent developments in plasmon-supported Raman spectroscopy*, World Scientific (Europe): 2017; pp 1–32.

23.   Stockman, M. I. Nanoplasmonics: past, present, and glimpse into future. *Optics Express* **2011**, *19*, 22029–22106.

24.   Fernandez-Dominguez, A. I.; Garcia-Vidal, F. J.; Martin-Moreno, L. Unrelenting plasmons. *Nature Photonic* **2017**, *11*, 8–10.

25.   Sheldon, M. T.; van de Groep, J.; Brown, A. M.; Polman, A.; Atwater, H. A. Plasmoelectric potentials in metal nanostructures. *Science* **2014**, *346*, 828–831.

26.   Chou, C. H.; Chen, F. C. Plasmonic nanostructures for light trapping in organic photovoltaic devices. *Nanoscale* **2014**, *6*, 8444–8458.

27.   Lal, S.; Clare, S. E.; Halas, N. J. Nanoshell-enabled photothermal cancer therapy: impending clinical impact. *Accounts of Chemical Research* **2008**, *41*, 1842–1851.

28.   Becker, S. F.; Esmann, M.; Yoo, K.; Gross, P.; Vogelgesang, R.; Park, N.; Lienau, C. Gap-plasmon-enhanced nanofocusing near-field microscopy. *ACS Photonics* **2016**, *3*, 223–232.

29.   Lal, S.; Link, S.; Halas, N. J. Nano-optics from sensing to waveguiding. *Nature Photonic* **2007**, *1*, 641–648.

30.   Vogelsang, J.; Robin, J.; Nagy, B. J.; Dombi, P.; Rosenkranz, D.; Schiek, M.; Groß, P.; Lienau, C. Ultrafast electron emission from a sharp metal nanotaper driven by adiabatic nanofocusing of surface plasmons. *Nano Letters* **2015**, *15*, 4685–4691.

31.   Schattschneider, P., *Fundamentals of inelastic electron scattering*. Springer Vienna: 1986.

32.   Zhang, R.; Bursi, L.; Cox, J. D.; Cui, Y.; Krauter, C. M.; Alabastri, A.; Manjavacas, A.; Calzolari, A.; Corni, S.; Molinari, E.; Carter, E. A.; García de Abajo, F. J.; Zhang, H.; Nordlander, P. How to identify plasmons from the optical response of nanostructures. *ACS Nano* **2017**, *11*, 7321–7335.

33.   Trügler, A., Optical properties of metallic nanoparticles: basic principles and simulation. Springer International Publishing: 2016.

34.   Yakubovsky, D. I.; Arsenin, A. V.; Stebunov, Y. V.; Fedyanin, D. Y.; Volkov, V. S. Optical constants and structural properties of thin gold films. *Optics Express* **2017**, *25*, 25574–25587.

35.   Tame, M. S.; McEnery, K. R.; Ozdemir, S. K.; Lee, J.; Maier, S. A.; Kim, M. S. Quantum plasmonics. *Nature Physics* **2013**, *9*, 329–340.

36.   Raza, S.; Yan, W.; Stenger, N.; Wubs, M.; Mortensen, N. A. Blueshift of the surface plasmon resonance in silver nanoparticles: substrate effects. *Optics Express* **2013**, *21*, 27344–27355.

37.   Plasmonics. In *From Basics to Advanced Topics*, Enoch S., Bonod, N., Ed. Springer-Verlag Berlin Heidelberg: 2012.

38.   Maier, S. A.; Atwater, H. A. Plasmonics: Localization and guiding of electromagnetic energy in metal/dielectric structures. *Journal of Applied Physics* **2005**, *98*, 011101.

39.   Nápoles-Duarte, J. M.; Chavez-Rojo, M. A.; Fuentes-Montero, M. E.; Rodríguez-Valdez, L. M.; García-Llamas, R.; Gaspar-Armenta, J. A. Surface plasmon resonances in Drude metal cylinders: radius dependence and quality factor. *Journal of Optics* **2015**, *17*, 065003.

40.   Lotito, V.; Hafner, C.; Sennhauser, U.; Bona, G.-L., Novel SNOM probes based on nanofocusing in asymmetric structures. In *Plasmonics - Principles and Applications*, Kim, K. Y., Ed. InTech: Rijeka, 2012; pp 99–134.

41.   Esmann, M.; Becker, S. F.; da Cunha, B. B.; Brauer, J. H.; Vogelgesang, R.; Gross, P.; Lienau, C. k-space imaging of the eigenmodes of sharp gold tapers for scanning near-field optical microscopy. *Beilstein Journal of Nanotechnology* **2013**, *4*, 603–610.

42.   Albrecht, G.; Ubl, M.; Kaiser, S.; Giessen, H.; Hentschel, M. Comprehensive study of plasmonic materials in the visible and near infrared: linear, refractory, and nonlinear optical properties. *ACS Photonics* **2018**, *5*, 1058–1067.

43.   Bethe, H. A. Theory of diffraction by small holes. *Physical Review* **1944**, *66*, 163–182.

44.   Kihm, H. W.; Koo, S. M.; Kim, Q. H.; Bao, K.; Kihm, J. E.; Bak, W. S.; Eah, S. H.; Lienau, C.; Kim, H.; Nordlander, P.; Halas, N. J.; Park, N. K.; Kim, D. S. Bethe-hole polarization analyser for the magnetic vector of light. *Nature Communications* **2011**, *2*, 451.

45.   Kihm, H. W.; Kim, J.; Koo, S.; Ahn, J.; Ahn, K.; Lee, K.; Park, N.; Kim, D.-S. Optical magnetic field mapping using a subwavelength aperture. *Optics Express* **2013**, *21*, 5625–5633.

46.   Jackson, J. D., *Classical electrodynamics*. 3rd ed.; John Wiley & Sons, Inc.: 1998.

47.   Talebi, N.; Ögüt, B.; Sigle, W.; Vogelgesang, R.; van Aken, P. A. On the symmetry and topology of plasmonic eigenmodes in heptamer and hexamer nanocavities. *Applied Physics A* **2014**, *116*, 947–954.

48. Dubovik, V. M.; Tugushev, V. V. Toroid moments in electrodynamics and solid-state physics. *Physics Reports* **1990**, *187*, 145–202.

49. Brenny, B. J. M.; Polman, A.; García de Abajo, F. J. Femtosecond plasmon and photon wave packets excited by a high-energy electron on a metal or dielectric surface. *Physical Review B* **2016**, *94*, 155412.

50. Campos, A.; Arbouet, A.; Martin, J.; Gerard, D.; Proust, J.; Plain, J.; Kociak, M. Plasmonic breathing and edge Modes in aluminum nanotriangles. *ACS Photonics* **2017**, *4*, 1257–1263.

51. Sutter, P.; Li, Y.; Argyropoulos, C.; Sutter, E. In situ electron microscopy of plasmon-mediated nanocrystal synthesis. *Journal of the American Chemical Society* **2017**, *139*, 6771–6776.

52. Guzzinati, G.; Béché, A.; Lourenço-Martins, H.; Martin, J.; Kociak, M.; Verbeeck, J. Probing the symmetry of the potential of localized surface plasmon resonances with phase-shaped electron beams. *Nature Communications* **2017**, *8*, 14999.

53. Chu, M.-W.; Myroshnychenko, V.; Chen, C. H.; Deng, J.-P.; Mou, C.-Y.; García de Abajo, F. J. Probing bright and dark surface-plasmon modes in individual and coupled noble metal nanoparticles using an electron beam. *Nano Letters* **2009**, *9*, 399–404.

54. Talebi, N.; Sigle, W.; Vogelgesang, R.; Koch, C. T.; Fernández-López, C.; Liz-Marzán, L. M.; Ögüt, B.; Rohm, M.; van Aken, P. A. Breaking the mode degeneracy of surface plasmon resonances in a triangular system. *Langmuir* **2012**, *28*, 8867–8873.

55. Barrow, S. J.; Rossouw, D.; Funston, A. M.; Botton, G. A.; Mulvaney, P. Mapping bright and dark Modes in gold nanoparticle chains using electron energy loss spectroscopy. *Nano Letters* **2014**, *14*, 3799–3808.

56. García de Abajo, F. J.; Kociak, M. Probing the photonic local density of states with electron energy loss spectroscopy. *Physical Review Letters* **2008**, *100*, 106804.

57. García de Abajo, F. J. Optical excitations in electron microscopy. *Reviews of Modern Physics* **2010**, *82*, 209–275.

58. Cherqui, C.; Thakkar, N.; Li, G.; Camden, J. P.; Masiello, D. J. Characterizing localized surface plasmons using electron energy-loss spectroscopy. *Annual Review of Physical Chemistry* **2016**, *67*, 331–357.

59. Wu, Y.; Li, G.; Camden, J. P. Probing nanoparticle plasmons with electron energy loss spectroscopy. *Chemical Reviews* **2017**, *118*, 2994–3031.

60. Kawasaki, N.; Meuret, S.; Weil, R.; Lourenço-Martins, H.; Stéphan, O.; Kociak, M. Extinction and scattering properties of high-order surface plasmon modes in silver nanoparticles probed by combined spatially resolved electron energy loss spectroscopy and cathodoluminescence. *ACS Photonics* **2016**, *3*, 1654–1661.

61. Gür, F. N.; McPolin, C. P. T.; Raza, S.; Mayer, M.; Roth, D. J.; Steiner, A. M.; Löffler, M.; Fery, A.; Brongersma, M. L.; Zayats, A. V.; König, T. A. F.; Schmidt, T. L., Self-assembled plasmonic waveguides for excitation of fluorescent nanodiamonds. 12/2017 ed.; ARXIV, 2017; pp 1–40.

62. Saito, H.; Yamamoto, N.; Sannomiya, T. Waveguide bandgap in crystalline bandgap slows down surface plasmon polariton. *ACS Photonics* **2017**, *4*, 1361–1370.

63. Haberfehlner, G.; Schmidt, F. P.; Schaffernak, G.; Horl, A.; Trugler, A.; Hohenau, A.; Hofer, F.; Krenn, J. R.; Hohenester, U.; Kothleitner, G. 3D imaging of gap plasmons in vertically coupled nanoparticles by EELS tomography. *Nano Letters* **2017**, *17*, 6773–6777.

64. Thollar, Z.; Wadell, C.; Matsukata, T.; Yamamoto, N.; Sannomiya, T. Three-dimensional multipole rotation in spherical silver nanoparticles observed by cathodoluminescence. *ACS Photonics* **2017**.

65. Feist, A.; Echternkamp, K. E.; Schauss, J.; Yalunin, S. V.; Schafer, S.; Ropers, C. Quantum coherent optical phase modulation in an ultrafast transmission electron microscope. *Nature* **2015**, *521*, 200–203.

66. Yurtsever, A.; van der Veen, R. M.; Zewail, A. H. Subparticle ultrafast spectrum imaging in 4D electron microscopy. *Science* **2012**, *335*, 59–64.

67. Merano, M.; Sonderegger, S.; Crottini, A.; Collin, S.; Renucci, P.; Pelucchi, E.; Malko, A.; Baier, M. H.; Kapon, E.; Deveaud, B.; Ganière, J. D. Probing carrier dynamics in nanostructures by picosecond cathodoluminescence. *Nature* **2005**, *438*, 479.

68. Talebi, N. A directional, ultrafast and integrated few-photon source utilizing the interaction of electron beams and plasmonic nanoantennas. *New Journal of Physics* **2014**, *16*, 053021.

69.   Talebi, N. Interaction of electron beams with optical nanostructures and metamaterials: from coherent photon sources towards shaping the wave function. *Journal of Optics* **2017**, *19*, 103001.
70.   Johnson, P. B.; Christy, R. W. Optical constants of the noble metals. *Physical Review B* **1972**, *6*, 4370–4379.
71.   Park, J. H.; Ambwani, P.; Manno, M.; Lindquist, N. C.; Nagpal, P.; Oh, S.-H.; Leighton, C.; Norris, D. J. Single-crystalline silver films for plasmonics. *Advanced Materials* **2012**, *24*, 3988–3992.
72.   Schmidt, S.; Piglosiewicz, B.; Sadiq, D.; Shirdel, J.; Lee, J. S.; Vasa, P.; Park, N.; Kim, D.-S.; Lienau, C. Adiabatic nanofocusing on ultrasmooth single-crystalline gold tapers creates a 10-nm-sized light source with few-cycle time resolution. *ACS Nano* **2012**, *6*, 6040–6048.
73.   Richter, G.; Hillerich, K.; Gianola, D. S.; Mönig, R.; Kraft, O.; Volkert, C. A. Ultrahigh strength single crystalline nanowhiskers grown by physical vapor deposition. *Nano Letters* **2009**, *9*, 3048–3052.
74.   Schamel, M.; Schopf, C.; Linsler, D.; Haag, S. T.; Hofacker, L.; Kappel, C.; Strunk, H. P.; Richter, G. The filamentary growth of metals. *International Journal of Materials Research* **2011**, *102*, 828–836.
75.   Lyles Jr, R. L.; Rothman, S. J.; Jäger, W. A cyanide-free solution for electropolishing silver. *Metallography* **1978**, *11*, 361–363.
76.   Williams, D. B.; Carter, C. B., *Transmission electron microscopy*. 2 ed.; Springer US: 2009.
77.   Essers, E.; Benner, G.; Mandler, T.; Meyer, S.; Mittmann, D.; Schnell, M.; Höschen, R. Energy resolution of an Omega-type monochromator and imaging properties of the MANDOLINE filter. *Ultramicroscopy* **2010**, *110*, 971–980.
78.   Peña, F. d. l.; Burdet, P.; Ostasevicius, T.; Sarahan, M.; magnunor; vidartf; Taillon, J.; Eljarrat, A.; Mazzucco, S.; Donval, G.; Zagonel, L. F.; Walls, M.; iygr hyperspy: HyperSpy 0.8.1. https://doi.org/10.5281/zenodo.27735.
79.   Corporation, O. 18.1 Smoothing. https://www.originlab.com/doc/Origin-Help/Smoothing (accessed 15 November, 2017).
80.   Maznev, A. A.; Wright, O. B. Upholding the diffraction limit in the focusing of light and sound. *Wave Motion* **2017**, *68*, 182–189.
81.   Novotny, L., Chapter 5 The history of near-field optics. In *Progress in Optics*, Wolf, E., Ed. Elsevier: 2007; Vol. 50, pp 137–184.
82.   Babadjanyan, A. J.; Margaryan, N. L.; Nerkararyan, K. V. Superfocusing of surface polaritons in the conical structure. *Journal of Applied Physics* **2000**, *87*, 3785–3788.
83.   Stockman, M. I. Nanofocusing of optical energy in tapered plasmonic waveguides. *Physical Review Letters* **2004**, *93*, 137404.
84.   Gramotnev, D. K.; Bozhevolnyi, S. I. Nanofocusing of electromagnetic radiation. *Nature Photonics* **2014**, *8*, 13–22.
85.   A., B.; J., R.; R., B. M.; L., N. Plasmon-coupled tip-enhanced near-field optical microscopy. *Journal of Microscopy* **2003**, *210*, 220-224.
86.   Frimmer, M.; Novotny, L. Controlling light at the nanoscale. *Europhysics News* **2015**, *46*, 27–30.
87.   Umakoshi, T.; Saito, Y.; Verma, P. Highly efficient plasmonic tip design for plasmon nanofocusing in near-field optical microscopy. *Nanoscale* **2016**, *8*, 5634–5640.
88.   Lindquist, N. C.; Jose, J.; Cherukulappurath, S.; Chen, X.; Johnson, T. W.; Oh, S.-H. Tip-based plasmonics: squeezing light with metallic nanoprobes. *Laser & Photonics Reviews* **2013**, *7*, 453–477.
89.   Ropers, C.; Neacsu, C. C.; Elsaesser, T.; Albrecht, M.; Raschke, M. B.; Lienau, C. Grating-coupling of surface plasmons onto metallic tips: A nanoconfined light source. *Nano Letters* **2007**, *7*, 2784–2788.
90.   Neacsu, C. C.; Berweger, S.; Olmon, R. L.; Saraf, L. V.; Ropers, C.; Raschke, M. B. Near-field localization in plasmonic superfocusing: A nanoemitter on a tip. *Nano Letters* **2010**, *10*, 592–596.
91.   Sadiq, D.; Shirdel, J.; Lee, J. S.; Selishcheva, E.; Park, N.; Lienau, C. Adiabatic nanofocusing scattering-type optical nanoscopy of individual gold nanoparticles. *Nano Letters* **2011**, *11*, 1609–1613.
92.   Groß, P.; Esmann, M.; Becker, S. F.; Vogelsang, J.; Talebi, N.; Lienau, C. Plasmonic nanofocusing – grey holes for light. *Advances in Physics: X* **2016**, *1*, 297–330.

93. Schröder, B.; Weber, T.; Yalunin, S. V.; Kiel, T.; Matyssek, C.; Sivis, M.; Schäfer, S.; von Cube, F.; Irsen, S.; Busch, K.; Ropers, C.; Linden, S. Real-space imaging of nanotip plasmons using electron energy loss spectroscopy. *Physical Review B* **2015**, *92*, 085411.

94. Piglosiewicz, B.; Vogelsang, J.; Schmidt, S.; Park, D. J.; Groß, P.; Lienau, C. Electron photoemission and acceleration from sharp gold nanotapers in the strong-field, few-cycle regime. *Quantum Matter* **2014**, *3*, 297–306.

95. Müller, M.; Kravtsov, V.; Paarmann, A.; Raschke, M. B.; Ernstorfer, R. Nanofocused plasmon-driven sub-10 fs electron point source. *ACS Photonics* **2016**, *3*, 611–619.

96. Berweger, S.; Atkin, J. M.; Olmon, R. L.; Raschke, M. B. Light on the tip of a needle: plasmonic nanofocusing for spectroscopy on the nanoscale. *The Journal of Physical Chemistry Letters* **2012**, *3*, 945–952.

97. Talebi, N.; Sigle, W.; Vogelgesang, R.; Esmann, M.; Becker, S. F.; Lienau, C.; van Aken, P. A. Excitation of mesoscopic plasmonic tapers by relativistic electrons: phase matching versus eigenmode resonances. *ACS Nano* **2015**, *9*, 7641–7648.

98. Yalunin, S. V.; Schröder, B.; Ropers, C. Theory of electron energy loss near plasmonic wires, nanorods, and cones. *Physical Review B* **2016**, *93*, 115408.

99. Thomas, S.; Wachter, G.; Lemell, C.; Burgdörfer, J.; Hommelhoff, P. Large optical field enhancement for nanotips with large opening angles. *New Journal of Physics* **2015**, *17*, 063010.

100. Boudarham, G.; Kociak, M. Modal decompositions of the local electromagnetic density of states and spatially resolved electron energy loss probability in terms of geometric modes. *Physical Review B* **2012**, *85*, 245447.

101. Kalkbrenner, T.; Ramstein, M.; Mlynek, J.; Sandoghdar, V. A single gold particle as a probe for apertureless scanning near-field optical microscopy. *Journal of Microscopy* **2001**, *202*, 72–76.

102. Weisenburger, S.; Sandoghdar, V. Light microscopy: an ongoing contemporary revolution. *Contemporary Physics* **2015**, *56*, 123–143.

103. Gurbatov, S.; Vitrik, O.; Kulchin, Y.; Kuchmizhak, A. Mapping the refractive index with single plasmonic nanoantenna. *Scientific Reports* **2018**, *8*, 3861.

104. Talebi, N.; Sigle, W.; Vogelgesang, R.; van Aken, P. Numerical simulations of interference effects in photon-assisted electron energy-loss spectroscopy. *New Journal of Physics* **2013**, *15*, 053013.

105. Jang, M. S.; Atwater, H. Plasmonic rainbow trapping structures for light localization and spectrum splitting. *Physical Review Letters* **2011**, *107*, 207401.

106. Kravtsov, V.; Atkin, J. M.; Raschke, M. B. Group delay and dispersion in adiabatic plasmonic nanofocusing. *Optics Letters* **2013**, *38*, 1322–1324.

107. Dorfmüller, J.; Vogelgesang, R.; Weitz, R. T.; Rockstuhl, C.; Etrich, C.; Pertsch, T.; Lederer, F.; Kern, K. Fabry-Pérot resonances in one-dimensional plasmonic nanostructures. *Nano Letters* **2009**, *9*, 2372–2377.

108. Kuttge, M.; Vesseur, E. J. R.; Koenderink, A. F.; Lezec, H. J.; Atwater, H. A.; García de Abajo, F. J.; Polman, A. Local density of states, spectrum, and far-field interference of surface plasmon polaritons probed by cathodoluminescence. *Physical Review B* **2009**, *79*, 113405.

109. Brenny, B. J. M.; Coenen, T.; Polman, A. Quantifying coherent and incoherent cathodoluminescence in semiconductors and metals. *Journal of Applied Physics* **2014**, *115*, 244307.

110. Stöger-Pollach, M.; Kachtík, L.; Miesenberger, B.; Retzl, P. Transition radiation in EELS and cathodoluminescence. *Ultramicroscopy* **2017**, *173*, 31–35.

111. Mooradian, A. Photoluminescence of metals. *Physical Review Letters* **1969**, *22*, 185–187.

112. Beversluis, M. R.; Bouhelier, A.; Novotny, L. Continuum generation from single gold nanostructures through near-field mediated intraband transitions. *Physical Review B* **2003**, *68*, 115433.

113. Ngoc, L. L. T.; Wiedemair, J.; van den Berg, A.; Carlen, E. T. Plasmon-modulated photoluminescence from gold nanostructures and its dependence on plasmon resonance, excitation energy, and band structure. *Optics Express* **2015**, *23*, 5547–5564.

114. Cai, Y. Y.; Liu, J. G.; Tauzin, L. J.; Huang, D.; Sung, E.; Zhang, H.; Joplin, A.; Chang, W. S.; Nordlander, P.; Link, S. Photoluminescence of gold nanorods: Purcell effect enhanced emission from hot carriers. *ACS Nano* **2018**, *12*, 976–985.

115. Sehmi, H. S.; Langbein, W.; Muljarov, E. A. Optimizing the Drude-Lorentz model for material permittivity: Method, program, and examples for gold, silver, and copper. *Physical Review B* **2017**, *95*, 115444.

116.   Yamamoto, N.; García de Abajo, F. J.; Myroshnychenko, V. Interference of surface plasmons and Smith-Purcell emission probed by angle-resolved cathodoluminescence spectroscopy. *Physical Review B* **2015**, *91*, 125144.

117.   Miroshnichenko, A. E.; Flach, S.; Kivshar, Y. S. Fano resonances in nanoscale structures. *Reviews of Modern Physics* **2010**, *82*, 2257–2298.

118.   Guo, S.; Talebi, N.; Sigle, W.; Vogelgesang, R.; Richter, G.; Esmann, M.; Becker, S. F.; Lienau, C.; van Aken, P. A. Reflection and phase matching in plasmonic gold tapers. *Nano Letters* **2016**, *16*, 6137–6144.

119.   Zeldovich, I. B. Electromagnetic interaction with parity violation. *Soviet Physics Jetp-Ussr* **1958**, *6*, 1184–1186.

120.   Ginzburg, V. L.; Tsytovich, V. N. Fields and radiation of toroidal dipole-moments moving uniformly in a medium. *Zhurnal Eksperimentalnoi I Teoreticheskoi Fiziki* **1985**, *88*, 84–95.

121.   Afanasiev, G. N.; Stepanovsky, Y. P. The electromagnetic-field of elementary time-dependent toroidal sources. *Journal of Physics A* **1995**, *28*, 4565–4580.

122.   Heras, J. Electric and magnetic fields of a toroidal dipole in arbitrary motion. *Physics Letters A* **1998**, *249*, 1–9.

123.   Radescu, E. E.; Vaman, G. Toroid moments in the momentum and angular momentum loss by a radiating arbitrary source. *Physical Review E* **2002**, *65*, 035601.

124.   Vrejoiu, C. Electromagnetic multipoles in Cartesian coordinates. *Journal of Physics a-Mathematical and General* **2002**, *35*, 9911–9922.

125.   Papasimakis, N.; Fedotov, V. A.; Marinov, K.; Zheludev, N. I. Gyrotropy of a metamolecule: wire on a torus. *Physical Review Letters* **2009**, *103*, 093901.

126.   Nanz, S., *Toroidal multipole moments in classical electrodynamics*. Springer Fachmedien Wiesbaden, **2016**.

127.   Fernandez-Corbaton, I.; Nanz, S.; Rockstuhl, C. On the dynamic toroidal multipoles from localized electric current distributions. *Scientific Reports* **2017**, *7*, 7527.

128.   Radescu, E. E.; Vaman, G. Exact calculation of the angular momentum loss, recoil force, and radiation intensity for an arbitrary source in terms of electric, magnetic, and toroid multipoles. *Physical review. E* **2002**, *65*, 046609.

129.   Papasimakis, N.; Fedotov, V. A.; Savinov, V.; Raybould, T. A.; Zheludev, N. I. Electromagnetic toroidal excitations in matter and free space. *Nature Materials* **2016**, *15*, 263–271.

130.   Talebi, N.; Guo, S.; van Aken, P. A. Theory and applications of toroidal moments in electrodynamics: their emergence, characteristics, and technological relevance. *Nanophotonics* **2018**, *7*, 93–110.

131.   Savinov, V.; Fedotov, V. A.; Zheludev, N. I. Toroidal dipolar excitation and macroscopic electromagnetic properties of metamaterials. *Physical Review B* **2014**, *89*, 205112–205111–205112.

132.   Sessoli, R.; Boulon, M.-E.; Caneschi, A.; Mannini, M.; Poggini, L.; Wilhelm, F.; Rogalev, A. Strong magneto-chiral dichroism in a paramagnetic molecular helix observed by hard X-rays. *Nature Phyics* **2015**, *11*, 69–74.

133.   Lin, S. Y.; Wernsdorfer, W.; Ungur, L.; Powell, A. K.; Guo, Y. N.; Tang, J.; Zhao, L.; Chibotaru, L. F.; Zhang, H. J. Coupling Dy3 triangles to maximize the toroidal moment. *Angewandte Chemie-International Edition* **2012**, *51*, 12767–12771.

134.   Li, X.-L.; Wu, J.; Tang, J.; Le Guennic, B.; Shi, W.; Cheng, P. A planar triangular $Dy_3 + Dy_3$ single-molecule magnet with a toroidal magnetic moment. *Chemical Communications* **2016**, *52*, 9570–9573.

135.   Chibotaru, L. F.; Ungur, L.; Soncini, A. The origin of nonmagnetic Kramers doublets in the ground state of dysprosium triangles: evidence for a toroidal magnetic moment. *Angewandte Chemie-International Edition* **2008**, *47*, 4126–4129.

136.   Rondin, L.; Tetienne, J.-P.; Spinicelli, P.; Savio, C. D.; Karrai, K.; Dantelle, G.; Thiaville, A.; Rohart, S.; Roch, J.-F.; Jacques, V. Nanoscale magnetic field mapping with a single spin scanning probe magnetometer. *Applied Physics Letters* **2012**, *100*, 153118.

137.   Gusev, A.; Herchel, R.; Nemec, I.; Shul'gin, V.; Eremenko, I. L.; Lyssenko, K.; Linert, W.; Trávníček, Z. Tetranuclear lanthanide complexes containing a hydrazone-type ligand. Dysprosium [2 × 2] gridlike single-molecule magnet and toroic. *Inorganic Chemistry* **2016**, *55*, 12470–12476.

138.   Biswas, S.; Das, S.; Gupta, T.; Singh, S. K.; Pissas, M.; Rajaraman, G.; Chandrasekhar, V. Observation of slow relaxation and single-molecule toroidal behavior in a family of butterfly-shaped Ln4 complexes. *Chemistry – A European Journal* **2016**, *22*, 18532–18550.

139.   Scagnoli, V.; Staub, U.; Bodenthin, Y.; de Souza, R. A.; García-Fernández, M.; Garganourakis, M.; Boothroyd, A. T.; Prabhakaran, D.; Lovesey, S. W. Observation of orbital currents in CuO. *Science* **2011**, *332*, 696–698.

140.   Jodlauk, S.; Becker, P.; Mydosh, J. A.; Khomskii, D. I.; Lorenz, T.; Streltsov, S. V.; Hezel, D. C.; Bohatý, L. Pyroxenes: a new class of multiferroics. *Journal of Physics: Condensed Matter* **2007**, *19*, 432201.

141.   Popov, Y. F.; Kadomtseva, A. M.; Vorob'ev, G. P.; Timofeeva, V. A.; Ustinin, D. M.; Zvezdin, A. K.; Tegeranchi, M. M. Magnetoelectric effect and toroidal ordering in $Ga_{2-x}Fe_xO_3$. *Journal of Experimental and Theoretical Physics* **1998**, *87*, 146–151.

142.   Van Aken, B. B.; Rivera, J.-P.; Schmid, H.; Fiebig, M. Observation of ferrotoroidic domains. *Nature* **2007**, *449*, 702–705.

143.   Baum, M.; Schmalzl, K.; Steffens, P.; Hiess, A.; Regnault, L. P.; Meven, M.; Becker, P.; Bohatý, L.; Braden, M. Controlling toroidal moments by crossed electric and magnetic fields. *Physical Review B* **2013**, *88*, 024414.

144.   Tolédano, P.; Ackermann, M.; Bohatý, L.; Becker, P.; Lorenz, T.; Leo, N.; Fiebig, M. Primary ferrotoroidicity in antiferromagnets. *Physical Review B* **2015**, *92*, 094431.

145.   Yamaguchi, Y.; Kimura, T. Magnetoelectric control of frozen state in a toroidal glass. *Nature Communications* **2013**, *4*, 2063.

146.   Spaldin, N. A.; Fiebig, M.; Mostovoy, M. The toroidal moment in condensed-matter physics and its relation to the magnetoelectric effect. *Journal of Physics: Condensed Matter* **2008**, *20*, 434203.

147.   Ederer, C.; Spaldin, N. A. Towards a microscopic theory of toroidal moments in bulk periodic crystals. *Physical Review B* **2007**, *76*, 214404.

148.   Sannikov, D. G. Phenomenological theory of the magnetoelectric effect in some boracites. *Journal of Experimental and Theoretical Physics* **1997**, *84*, 293–299.

149.   Sannikov, D. G. Ferrotoroic phase transition in boracites. *Ferroelectrics* **1998**, *219*, 177–181.

150.   Sannikov, D. G.; Schaack, G. Theoretical temperature-electric-field phase diagram for betaine calcium chloride dihydrate. *Physical Review B* **1998**, *58*, 8313–8322.

151.   Zimmermann, A. S.; Meier, D.; Fiebig, M. Ferroic nature of magnetic toroidal order. *Nature Communications* **2014**, *5*, 4796–4791–4796.

152.   Fiebig, M.; Meier, D. From magnetic vortices to magnetic monopoles – ferrotoroidicity as fourth form of ferroic order. https://www.manep.ch/from-magnetic-vortices-to-magnetic-monopoles/ (accessed April 4, 2017).

153.   Fiebig, M.; Lottermoser, T.; Meier, D.; Trassin, M. The evolution of multiferroics. *Nature Reviews Materials* **2016**, *1*, 16046.

154.   Popov, Y. F.; Kadomtseva, A. M.; Belov, D. V.; Vorob'ev, G. P.; Zvezdin, A. K. Magnetic-field-induced toroidal moment in the magnetoelectric Cr_2O_3. *Journal of Experimental and Theoretical Physics Letters* **1999**, *69*, 330–335.

155.   Hehl, F. W.; Obukhov, Y. N.; Rivera, J.-P.; Schmid, H. Relativistic nature of a magnetoelectric modulus of Cr_2O_3 crystals: A four-dimensional pseudoscalar and its measurement. *Physical Review A* **2008**, *77*, 022106.

156.   Wilczek, F. Two applications of axion electrodynamics. *Physical Review Letters* **1987**, *58*, 1799–1802.

157.   Tellegen, B. D. H. The Gyrator, a new electric network element. *Philips Research Reports* **1948**, *3*, 81–101.

158.   Valencia, S.; Crassous, A.; Bocher, L.; Garcia, V.; Moya, X.; Cherifi, R. O.; Deranlot, C.; Bouzehouane, K.; Fusil, S.; Zobelli, A.; Gloter, A.; Mathur, N. D.; Gaupp, A.; Abrudan, R.; Radu, F.; Barthelemy, A.; Bibes, M. Interface-induced room-temperature multiferroicity in $BaTiO_3$. *Nature Materials* **2011**, *10*, 753–758.

159.   Yadav, A. K.; Nelson, C. T.; Hsu, S. L.; Hong, Z.; Clarkson, J. D.; Schlepüetz, C. M.; Damodaran, A. R.; Shafer, P.; Arenholz, E.; Dedon, L. R.; Chen, D.; Vishwanath, A.; Minor, A. M.; Chen, L. Q.; Scott, J. F.; Martin, L. W.; Ramesh, R. Observation of polar vortices in oxide superlattices. *Nature* **2016**, *530*, 198–201.

160.   Naumov, I. I.; Bellaiche, L. M.; Prosandeev, S. A.; Ponomareva, I. V.; Kornev, I. A. Ferroelectric nanostructure having switchable multi-stable vortex states. **2009**, US7593250 B2.

161.   Naumov, I. I.; Bellaiche, L. M.; Fu, H. Unusual phase transitions in ferroelectric nanodisks and nanorods. *Nature* **2004**, *432*, 737–740.

162.   Liu, Y.; Zhang, X. Metamaterials: a new frontier of science and technology. *Chemical Society Reviews* **2011**, *40*, 2494–2507.

163.   Marinov, K.; Boardman, A. D.; Fedotov, V. A.; Zheludev, N. Toroidal metamaterial. *New Journal of Physics* **2007**, *9*, 324.

164.   Huang, Y.-W.; Chen, W. T.; Wu, P. C.; Fedotov, V.; Savinov, V.; Ho, Y. Z.; Chau, Y.-F.; Zheludev, N. I.; Tsai, D. P. Design of plasmonic toroidal metamaterials at optical frequencies. *Optics Express* **2012**, *20*, 1760–1768.

165.   Wu, P. C.; Hsu, W.-L.; Chen, W. T.; Huang, Y.-W.; Liao, C. Y.; Liu, A. Q.; Zheludev, N. I.; Sun, G.; Tsai, D. P. Plasmon coupling in vertical split-ring resonator metamolecules. *Scientific Reports* **2015**, *5*, 9726.

166.   Tang, C.; Chen, J.; Wang, Q.; Yan, Z.; Liu, B.; Liu, F.; Sui, C. Toroidal dipolar response in metamaterials composed of metal-dielectric-metal sandwich magnetic resonators. *IEEE Photonics Journal* **2016**, *8*, 1–9.

167.   Dong, Z.-G.; Zhu, J.; Yin, X.; Li, J.; Lu, C.; Zhang, X. All-optical Hall effect by the dynamic toroidal moment in a cavity-based metamaterial. *Physical Review B* **2013**, *87*, 245429.

168.   Wu, P. R.; Liao, C. Y.; Chen, W. T.; Wu, P. C.; Huang, Y.-W.; Tsai, W.-Y.; Chen, T.-Y.; Chen, J.-W.; Savinov, V.; Zheludev, N. I.; Tsai, D. P. In *Horizontal toroidal response in three-dimensional plasmonic (Conference Presentation)*, Proceedings of SPIE, **2016**; pp 992120–992121.

169.   Liao, C. Y.; Chen, M. K.; Huang, Y.-W.; Chen, W. T.; Wu, P. C.; Tsai, W.-Y.; Lin, H. T.; Huang, Y.-T.; Chen, T.-Y.; Chen, J.-W.; Savinov, V.; Zheludev, N. I.; Tsai, D. P. In *Optical toroidal response in three-dimensional plasmonic metamaterial (Conference Presentation)*, Proceedings of SPIE, **2015**; p 954724.

170.   Raybould, T. A.; Fedotov, V. A.; Papasimakis, N.; Kuprov, I.; Youngs, I. J.; Chen, W. T.; Tsai, D. P.; Zheludev, N. I. Toroidal circular dichroism. *Physical Review B* **2016**, *94*, 035119.

171.   Han, S.; Cong, L.; Gao, F.; Singh, R.; Yang, H. Observation of Fano resonance and classical analog of electromagnetically induced transparency in toroidal metamaterials. *Annalen der Physik* **2016**, *528*, 352–357.

172.   Fan, Y.; Wei, Z.; Li, H.; Chen, H.; Soukoulis, C. M. Low-loss and high-Q planar metamaterial with toroidal moment. *Physical Review B* **2013**, *87*, 115417.

173.   Basharin, A. A.; Chuguevsky, V.; Volsky, N.; Kafesaki, M.; Economou, E. N. Extremely high Q-factor metamaterials due to anapole excitation. *Physical Review B* **2017**, *95*, 035104.

174.   Bao, Y.; Zhu, X.; Fang, Z. Plasmonic toroidal dipolar response under radially polarized excitation. *Scientific Reports* **2015**, *5*, 11793.

175.   Dong, Z.-G.; Zhu, J.; Rho, J.; Li, J.-Q.; Lu, C.; Yin, X.; Zhang, X. Optical toroidal dipolar response by an asymmetric double-bar metamaterial. *Applied Physics Letters* **2012**, *101*, 144105.

176.   Li, J.; Shao, J.; Li, J.-Q.; Yu, X. Q.; Dong, Z.-G.; Chen, Q.; Zhai, Y. Optical responses of magnetic-vortex resonance in double-disk metamaterial variations. *Physics Letters A* **2014**, *378*, 1871–1875.

177.   Fedotov, V. A.; Rogacheva, A. V.; Savinov, V.; Tsai, D. P.; Zheludev, N. I. Resonant transparency and non-trivial non-radiating excitations in toroidal metamaterials. *Scientific Reports* **2013**, *3*, 2967.

178.   Guo, L.-Y.; Li, M.-H.; Huang, X.-J.; Yang, H.-L. Electric toroidal metamaterial for resonant transparency and circular cross-polarization conversion. *Applied Physics Letters* **2014**, *105*, 033507.

179.   Liu, W.; Shi, J.; Lei, B.; Hu, H.; Miroshnichenko, A. E. Efficient excitation and tuning of toroidal dipoles within individual homogenous nanoparticles. *Optics Express* **2015**, *23*, 24738–24747.

180.   Miroshnichenko, A. E.; Evlyukhin, A. B.; Yu, Y. F.; Bakker, R. M.; Chipouline, A.; Kuznetsov, A. I.; Luk'yanchuk, B.; Chichkov, B. N.; Kivshar, Y. S. Nonradiating anapole modes in dielectric nanoparticles. *Nature Communications* **2015**, *6*, 8069.

181.   Basharin, A. A.; Kafesaki, M.; Economou, E. N.; Soukoulis, C. M.; Fedotov, V. A.; Savinov, V.; Zheludev, N. I. Dielectric metamaterials with toroidal dipolar response. *Physical Review X* **2015**, *5*, 011036.

182.   Li, J.; Shao, J.; Wang, Y.-H.; Zhu, M.-J.; Li, J.-Q.; Dong, Z.-G. Toroidal dipolar response by a dielectric microtube metamaterial in the terahertz regime. *Optics Express* **2015**, *23*, 29138–29144.

183.   Liu, W.; Zhang, J.; Miroshnichenko, A. E. Toroidal dipole-induced transparency in core–shell nanoparticles. *Laser & Photonics Reviews* **2015**, *9*, 564–570.

184.   Zhang, Q.; Xiao, J. J.; Zhang, X. M.; Han, D.; Gao, L. Core–shell-structured dielectric–metal circular nanodisk antenna: gap plasmon assisted magnetic toroid-like cavity modes. *ACS Photonics* **2015**, *2*, 60–65.

185.   Li, J.; Zhang, Y.; Jin, R.; Wang, Q.; Chen, Q.; Dong, Z. Excitation of plasmon toroidal mode at optical frequencies by angle-resolved reflection. *Optics Letters* **2014**, *39*, 6683–6686.

186.   Tasolamprou, A. C.; Tsilipakos, O.; Kafesaki, M.; Soukoulis, C. M.; Economou, E. N. Toroidal eigenmodes in all-dielectric metamolecules. *Physical Review B* **2016**, *94*, 205433.

187.   Kaelberer, T.; Fedotov, V. A.; Papasimakis, N.; Tsai, D. P.; Zheludev, N. I. Toroidal dipolar response in a metamaterial. *Science* **2010**, *330*, 1510–1512.

188.   Xiang, H.; Ge, L.; Liu, L.; Jiang, T.; Zhang, Z. Q.; Chan, C. T.; Han, D. A minimal discrete model for toroidal moments and its experimental realization. *Physical Review B* **2017**, *95*, 045403.

189.   Wei, L.; Xi, Z.; Bhattacharya, N.; Urbach, H. P. Excitation of the radiationless anapole mode. *Optica* **2016**, *3*, 799–802.

190.   Gupta, M.; Savinov, V.; Xu, N.; Cong, L.; Dayal, G.; Wang, S.; Zhang, W.; Zheludev, N. I.; Singh, R. Sharp toroidal resonances in planar terahertz metasurfaces. *Advanced Materials* **2016**, *28*, 8206–8211.

191.   Gupta, M.; Singh, R. Toroidal versus Fano resonances in high Q planar THz metamaterials. *Advanced Optical Materials* **2016**, *4*, 2119–2125.

192.   Fan, Y.; Zhang, F.; Fu, Q.; Wei, Z.; Li, H. Controlling the toroidal excitations in metamaterials for high-Q response. ARXIV, **2016**, pp 1–12.

193.   Zhao, J.-F.; Zhang, Y.-W.; Li, Y.-H.; Chen, Y.-Q.; Fang, K.; He, L. Wireless power transfer system based on toroidal metamaterials. *Acta Physica Sinica* **2016**, *65*, 168801–168801.

194.   Urban, M. J.; Dutta, P. K.; Wang, P.; Duan, X.; Shen, X.; Ding, B.; Ke, Y.; Liu, N. Plasmonic toroidal metamolecules assembled by DNA origami. *Journal of the American Chemical Society* **2016**, *138*, 5495–5498.

195.   Totero Gongora, J. S.; Miroshnichenko, A. E.; Kivshar, Y. S.; Fratalocchi, A. Anapole nanolasers for mode-locking and ultrafast pulse generation. *Nature Communications* **2017**, *8*, 15535.

196.   Huang, Y.-W.; Chen, W. T.; Wu, P. C.; Fedotov, V. A.; Zheludev, N. I.; Tsai, D. P. Toroidal lasing spaser. *Scientific Reports* **2013**, *3*, 1237.

197.   Li, J.; Xin, X.-X.; Shao, J.; Wang, Y.-H.; Li, J.-Q.; Zhou, L.; Dong, Z.-G. From non- to super-radiating manipulation of a dipolar emitter coupled to a toroidal metastructure. *Optics Express* **2015**, *23*, 29384–29389.

198.   Li, J.; Dong, Z.-G.; Zhu, M.-J.; Shao, J.; Wang, Y.-H.; Li, J.-Q. Dual-band toroidal-dipole-induced transparency in optical regime. *Journal of Physics D: Applied Physics* **2016**, *49*, 345104.

199.   Hellwarth, R. W.; Nouchi, P. Focused one-cycle electromagnetic pulses. *Physical Review E* **1996**, *54*, 889–895.

200.   Raybould, T. A.; Fedotov, V.; Papasimakis, N.; Youngs, I.; Zheludev, N. Focused electromagnetic doughnut pulses and their interaction with interfaces and nanostructures. *Optics Express* **2016**, *24*, 3150–3161.

201.   Schmidt, F.-P.; Losquin, A.; Hofer, F.; Hohenau, A.; Krenn, J. R.; Kociak, M. How dark are radial breathing modes in plasmonic nanodisks? *ACS Photonics* **2018**, *5*, 861–866.

202.   Sidgwick, N. V. Dipole moment and molecular structure. *Chemical Reviews* **1936**, *19*, 183–194.

203.   Yamanaka, N. Review of the electric dipole moment of light nuclei. *International Journal of Modern Physics E* **2017**, *26*, 1730002.

204.   Spackman, M. A.; Munshi, P.; Dittrich, B. Dipole moment enhancement in molecular crystals from X-ray diffraction data. *ChemPhysChem* **2007**, *8*, 2051–2063.

205.   Sharp, K. A.; Honig, B. Electrostatic interactions in macromolecules: theory and applications. *Annual Review of Biophysics and Biophysical Chemistry* **1990**, *19*, 301–332.

206.   Kuznetsov, A. I.; Miroshnichenko, A. E.; Fu, Y. H.; Zhang, J.; Luk'yanchuk, B. Magnetic light. *Scientific Reports* **2012**, *2*, 492.

207.　Rivera, N.; Kaminer, I.; Zhen, B.; Joannopoulos, J. D.; Soljačić, M. Shrinking light to allow forbidden transitions on the atomic scale. *Science* **2016**, *353*, 263–269.

208.　Li, G.-C.; Zhang, Y.-L.; Jiang, J.; Luo, Y.; Lei, D. Y. Metal-substrate-mediated plasmon hybridization in a nanoparticle dimer for photoluminescence line-width shrinking and intensity enhancement. *ACS Nano* **2017**, *11*, 3067–3080.

209.　Talebi, N.; Shahabdi, M. Analysis of the propagation of light along an array of nanorods using the generalized multipole techniques. *Journal of Computational and Theoretical Nanoscience* **2008**, *5*, 711–716.

210.　Duan, H.; Fernández-Domínguez, A. I.; Bosman, M.; Maier, S. A.; Yang, J. K. W. Nanoplasmonics: classical down to the nanometer scale. *Nano Letters* **2012**, *12*, 1683–1689.

211.　Giannini, V.; Fernández-Domínguez, A. I.; Sonnefraud, Y.; Roschuk, T.; Fernández-García, R.; Maier, S. A. Controlling light localization and light–matter interactions with nanoplasmonics. *Small* **2010**, *6*, 2498–2507.

212.　Solís, D. M.; Taboada, J. M.; Obelleiro, F.; Liz-Marzán, L. M.; García de Abajo, F. J. Toward ultimate nanoplasmonics modeling. *ACS Nano* **2014**, *8*, 7559–7570.

213.　Mascheck, M.; Schmidt, S.; Silies, M.; Yatsui, T.; Kitamura, K.; Ohtsu, M.; Leipold, D.; Runge, E.; Lienau, C. Observing the localization of light in space and time by ultrafast second-harmonic microscopy. *Nature Photonics* **2012**, *6*, 293–298.

214.　Zhang, S.; Genov, D. A.; Wang, Y.; Liu, M.; Zhang, X. Plasmon-induced transparency in metamaterials. *Physical Review Letters* **2008**, *101*, 047401.

215.　Liu, N.; Langguth, L.; Weiss, T.; Kastel, J.; Fleischhauer, M.; Pfau, T.; Giessen, H. Plasmonic analogue of electromagnetically induced transparency at the Drude damping limit. *Nature Materials* **2009**, *8*, 758–762.

216.　Artamonov, Y. A.; Gorbatsevich, A. A. Symmetry and dynamics of systems with toroidal moments. *Zhurnal Eksperimentalnoi I Teoreticheskoi Fiziki* **1985**, *89*, 1078–1093.

217.　Liu, N.; Giessen, H. Coupling effects in optical metamaterials. *Angewandte Chemie International Edition* **2010**, *49*, 9838–9852.

218.　Guo, S.; Talebi, N.; van Aken, P. A. Long-range coupling of toroidal moments for the visible. *ACS Photonics* **2018**, *5*, 1326–1333.

219.　Krivanek, O. L.; Lovejoy, T. C.; Dellby, N.; Aoki, T.; Carpenter, R. W.; Rez, P.; Soignard, E.; Zhu, J.; Batson, P. E.; Lagos, M. J.; Egerton, R. F.; Crozier, P. A. Vibrational spectroscopy in the electron microscope. *Nature* **2014**, *514*, 209–212.

220.　Lagos, M. J.; Trügler, A.; Hohenester, U.; Batson, P. E. Mapping vibrational surface and bulk modes in a single nanocube. *Nature* **2017**, *543*, 529.